The Fabrication and Characterization of Terahertz Wave Photoconductive Dipole Antennas on Oxygen Ion Implanted GaAs

CHEN, Kejian

A Thesis Submitted in Partial Fulfillment

Of the Requirements for the Degree of

Doctor of Philosophy

in

Electronic Engineering

©The Chinese University of Hong Kong

January 2009

The Chinese University of Hong Kong holds the copyright of this thesis. Any person(s) intending to use a part of whole of the material in the thesis in a proposed publication must seek copyright release from the Dean of the Graduated School.

UMI Number: 3377988

INFORMATION TO USERS

The quality of this reproduction is dependent upon the quality of the copy submitted. Broken or indistinct print, colored or poor quality illustrations and photographs, print bleed-through, substandard margins, and improper alignment can adversely affect reproduction.
In the unlikely event that the author did not send a complete manuscript and there are missing pages, these will be noted. Also, if unauthorized copyright material had to be removed, a note will indicate the deletion.

UMI®

UMI Microform 3377988
Copyright 2009 by ProQuest LLC
All rights reserved. This microform edition is protected against unauthorized copying under Title 17, United States Code.

ProQuest LLC
789 East Eisenhower Parkway
P.O. Box 1346
Ann Arbor, MI 48106-1346

ABSTRACT OF THESIS ENTITLED:

The fabrication and characterization of terahertz wave photoconductive dipole antennas on oxygen ion implanted GaAs

Submitted by Chen, Kejian

For the degree of Doctor of Philosophy in Electronic Engineering

at The Chinese University of Hong Kong in January 2009

In the recent decade, lots of funds are provided to investigate terahertz (THz) wave and its applications in Fundamental Physics, Homeland Security, Biomedical, Astronomy and THz Communication. The main reason is that terahertz wave has some advantages of microwave, like the relatively long wavelength and transparency to some materials, and also some advantages of light, such as good directionality and high capacity for information transmission.

Lately, oxygen ion implanted GaAs (GaAs:O) has caught a lot of attention and been studied as an alternative material to Low Temperature Grown (LTG) GaAs material (which is commonly used to generate terahertz wave by photoconductive method) for its good performances in THz wave generation. GaAs:O has a reasonably high resistivity and ultra-short carrier lifetime close to those of LTG GaAs material. The preparation of GaAs:O is easy to control and reproduce compared with LTG GaAs material. A higher saturation level of both pumping and bias field of GaAs:O THz wave emitter is observed, which will lead to a higher output power of THz wave.

In this work, the GaAs:O materials are further studied. The preparation conditions of GaAs:O materials are optimized by adjusting the implant process and annealing temperature. The performance of devices made from GaAs:O in terms of THz wave generation is investigated under both pulsed and continuous-wave (CW) modes. The saturation behaviors and screening effects are also studied in this work.

The main results and original contribution of this research are summarized as follows:

1. Material:

✧ A uniform defect distribution was obtained in oxygen ion implanted GaAs

materials by a multi-implantation process followed by Rapid Thermal Annealing (RTA).

- ✧ A dark resistance higher than **10^6** Ohm/square was obtained after RTA in GaAs:O. An ultra-short carrier lifetime (around **0.35ps**) was achieved with high implant dosage and a suitable annealing temperature.
- ✧ Compared with the LTG GaAs tested in this work, GaAs:O has a **relatively higher saturation threshold**, which allows it to generate higher CW THz power than this type LTG GaAs.

2. Photoconductive devices:

- ✧ For high-dose GaAs:O based PC antenna, under the pulsed generation mode, around **31μW** average power was achieved under the condition of 35mW pumping power and 70V DC bias. Under the CW generation mode, 0.35 THz single frequency wave is generated at the level of tens of nW, which is around 2~3 orders smaller than that under pulsed generation mode.
- ✧ For low-dose GaAs:O based PC antenna, about **48μW** average power was achieved under pulsed generation mode, **which is the highest power ever reported to our knowledge by such kind of devices**. An analysis of the power saturation behavior suggests that power levels at **~200μW** may be achievable in GaAs:O materials. CW THz wave at **μW** level was also achieved from this device at **0.358THz** under 180mW pump power and 80V bias voltage.
- ✧ The **THz spectra** of some GaAs:O devices are similar to that of LTG GaAs, which suggests GaAs:O can yield as good THz spectra as the LTG GaAs sample tested in this work.

3. Device modeling:

- ✧ Screening effect in the PC antenna, especially under CW background illumination, has been studied experimentally and theoretically. **A simple empirical model** has been proposed to explain the mechanism of the screening effect.
- ✧ We propose an **enhanced theoretical model** of CW THz generation which can adequately explain the bias-dependent saturation behavior of the PC antenna, as

evidenced by the good matching of simulation results and experimental data.

摘要

近幾十年來,太赫茲波(terahertz wave)及其在基礎物理，國土安全、生物醫學，天文學以及高速通信等領域的相關應用得到了廣泛的關注．大量的科研經費被投放到相關研究领域.太赫兹之所以這麼受關注的主要原因在於：太赫茲波不僅具備微波的不少優點,如相對較長的波長以及其對某些物質的穿透性；同時它還具備光波的一些優點,比如優良的方向性及高的信號承載能力.

最近幾年，氧離子注入型砷化鎵(GaAs:O)材料吸引了不少研究人員的注意.並由於其在太赫茲波產生領域的良好性能而被作爲低溫生長砷化鎵(LTG GaAs)的一種潛在替代材料來進行研究．(低溫生長砷化鎵是目前最常用的一種應用於太赫茲波產生(光電導方式)的基礎材料.）氧離子注入型砷化鎵材料擁有相當高的電阻率,以及接近低溫生長砷化鎵的超短載流子壽命．同時 GaAs:O 的生長條件要比 LTG GaAs 的容易控制，其可重複性也相對較高．另外 GaAs:O 材料擁有相對較高的光泵浦飽和能量以及較高的電場飽和閾值，而這兩個因素正好賦予了 GaAs:O 材料可產生高能量太赫茲波的能力.

本文將對 GaAs:O 材料做進一步的研究．通過對離子注入濃度及後續的退火溫度的控制與調整，GaAs:O 材料的生長條件得到了相應的優化．而 GaAs:O 材料在太赫茲波產生方面的性能則通過不同的產生模式進行了測試，他們分別是脈衝冲光(fs laser)激勵方式以及連續光(two single-mode CW lasers)激勵方式.文中還對不同的飽和現象(pump or bias) 以及能量掩蔽(screening)效應進行了相應的研究和探討.

在此研究過程中所獲得的主要實驗結果以及原創性貢獻總結如下:

1．<u>材料:</u>

✧ 通過結合多能量離子注入法(Multi-implantation)以及快速退火(RTA)技術實現氧離子在砷化鎵襯底內的均勻分佈

✧ 經過 RTA 流程後的 GaAs:O 材料可獲得高於 10^6 Ω/sq 的電阻率. 而通過注入大劑量離子以及選擇合適的退火溫度, GaAs:O 材料可獲得超短載流子壽命(約 **0.35ps**).

✧ 相對於 LTG GaAs 材料而言, 氧離子注入型砷化鎵材料有著相對較高的電場飽和閾值, 因而使其具備了產生相對較大連續光(CW)太赫茲波的能力.

2. 光導器件:

✧ 使用脈衝光激勵法產生太赫茲波時, 高參雜 **GaAs:O** 材料可以獲得約 **31** 微瓦 (平均功率) 的太赫茲波能量. 其工作條件爲 70V 的直流偏置電壓, 35mW 的泵浦光能量. 而採用連續光(CW)混頻方法產生太赫茲波時, 同一器件可以獲得幾十納瓦的(連續光)太赫茲波能量(工作波長爲 0.35 太赫茲), 這一能量要比脈衝光激勵方式下的小兩到三個數量級.

✧ 基於低參雜 GaAs:O 材料的光導天線可以在脈衝光激勵下產生 **48** 微瓦(平均功率)的太赫茲波, 是具我們所知的目前已經報導過經由类似器件獲得的最大输出能量.通過對器件的能量飽和特性的分析, 200 微瓦量級的最大輸出能量是可以預期的. 而在 180mW 光泵浦能量及 80V 直流電壓驅動下,同一器件可以獲得微瓦量級的連續光太赫茲波(其工作波長爲 **0.358 THz).**

✧ GaAs:O 材料所得到的太赫茲頻譜與從 LTG GaAs 材料得到的相近. 從這一點可以看出氧離子注入型砷化鎵也可以獲得不錯的太赫茲頻譜.

3. 器件建模:

✧ 能量掩蔽(screening)效應(特別是在外加連續光照射的情况下)在文中做了一

定的實驗和理論上的研究. 結果表明,文中所提出的簡單經驗模型在一定程度上可以滿足從物理上描述此現象的要求.

- 文中採用了一種經過優化的連續光(CW)太赫茲波產生的理論模型去解釋電場相關的飽和行爲. 仿真結果和實驗數據的較好吻合,證明瞭此理論模型是具有其合理性和適用性的

Acknowledgements

First of all, I would like to express my gratefulness to my supervisor, Professor K.T.Chan, who guided me with patience during these years' study. Thank you for providing me an abundant space for developing my research ability. And, thank you for your continuous advice and encouragement.

I am also grateful to Professor C.L. Pan (NCTU), who provided me the opportunity to work with a group of young and passionate researchers in this research area. And I own my gratitude to Prof.Chinlon Lin for broadening my vision on research and life. I am also grateful to Prof.Chester Shu and Prof. H.K. Tsang for their kindly concern and help. And I would like to express my deep appreciation to Professor. X.C. Zhang (RPI) for his insightful discussion on THz research.

I am very thankful to Dr.W.Y Cheung for his technical assistance on implantation and photolithography. Without his help, I couldn't prepare such good quality GaAs:O materials and PC devices. And I am also very grateful to Ms. L.C. Ho, who arranged the experimental equipments for me. Without her help, I couldn't purchase the components and finish my experiments on time.

I am very indebted to Mr.Yutai Li (NCTU), Mr.Weiwen Wang (NCTU) and Mr.Mong-huan Yang (NCTU) for the devices testing, as well as to Prof. C.K Lee (NSYSU) for the carrier lifetime measurement.

I would also like to thank deeply to Dr.Z Wang (TJU) and Mr.Y.J. Song (TJU) for sharing with me their excellent experience on Ti:sapphire laser and common space optics. And I am also grateful to Dr.Y.M Zhu (Tokyo U) and Dr. X.P. Zhou (Tokyo U) for their useful discussion on physics of Semiconductor. And I would like to thank Mr.L.Y Shao (HK PolyU) and Mr.X.W.Chen (ZJU) for their help on FBG fabrication and related discussion.

I would like to express my appreciation to Dr.N.Ke, Mr.Y.M.Fung, Mr.L.Wang, Mr.H.Wang, Mr.C.M Sun and my colleagues Dr.Y.G. Du, Dr.Y.H Luo, Dr.H.P. Li,

Dr. P.S Chan, Dr. Y.Liu, Dr.C.W.Chow, Dr.M.P.Fok, Dr.W.W Tang, Dr. T.Q. Liang, Dr. J. He, Dr.A.L. Zhang, Mr.C.H.Kwok, Ms. S.M Wan, Mr.T.Yang, Mr.H.Hao, Mr.Z.X. Zhang, Ms.M.Y. Chen, Mr.L.Xu, Mr.L.K Cheng, Mr.X.Chen, Mr.Y.H.Dai, Mr.K.P.Lei for their creation of wonderful working environment and their useful discussions.

And I would like to thank my friends Dr.Q. Tian, Mr.W.Zeng, Dr. Q. Zhao, Mr.James Hsu, Mr.H.Chen, Dr.W.Z.Ye, Dr.C.Y.Wen, Mr.L. Song, Mr.Z.C. Xie, Ms.Z.Y.Yang, Dr.K.Xu, Dr.C.L.Xiong, Ms.S.S.Zhu, Ms.L.Zhou, Mr.Z.K.Chen, Ms.X. Huang, Dr.R.G.Xie, Mr.B.Yang, Mr.X.Li for their warm friendship. Without them, I couldn't keep such adamantine willpower and overcome all the difficulties on the road.

Last but not the least, I would like to express my deepest gratitude to my parents and my elder sister, and all the other members of the big family, for their consideration, support, encouragement and love. Without them, I couldn't turn my dream into reality.

If the PhD degree means some honor, it belongs not only to me, but also to all of them mentioned above, especially to my father and mother!

Bow to you.

You own my great thanks!

Table of Contents

Abstract: i

Acknowledgements vii

Table of Contents ix

List of Tables and Figures xi

List of Abbreviations and Symbol xiv

Chapter 1:Introduction 1

- **1.1 Background** 1
- **1.2 Aim of this work** 7
- **1.3 Organization of the thesis** 8

Chapter 2:Material preparation and Characteristics 10

- **2.1 Introduction** 10
- **2.2 Process of Implantation** 13
  - **2.2.1 The advantage of ion implantation** 13
  - **2.2.2 Ion range and ion stopping** 14
  - **2.2.3 Structure of ion implanter** 15
  - **2.2.4 Selection of Implantation conditions** 16
- **2.3 Annealing process** 19
- **2.4 Material properties** 21
  - **2.4.1 Infrared light (IR) Absorption** 21
  - **2.4.2 Carrier concentration, Resistivity and Carrier mobility** 31
  - **2.4.3 Carrier lifetime** 36
- **2.5 Summary** 44

Chapter 3:Device Fabrication 47

- **3.1 Introduction** 47
- **3.2 Antenna structure** 48
- **3.3 Photolithography (process and parameters)** 49
  - **3.3.1 Wafer Cleaning** 51
  - **3.3.2 Photoresist Spin Coating** 52
  - **3.3.3 Pre-Bake (Soft Bake)** 53
  - **3.3.4 Alignment and Exposure** 54
  - **3.3.5 Post-bake (Hard Bake) and Flood Exposure** 55
  - **3.3.6 Development** 56
- **3.4 E-beam Evaporation and lift-off** 57
  - **3.4.1 E-beam evaporation** 57
  - **3.4.2 The material and deposition parameters selection** 58

3.4.3 Lift-off and the fabricated devices 59
3.5 Packaging and Wire Bonding 60
3.5.1 Packaging 60
3.5.2 Wire Bonding 60
3.6 Summary 62
Chapter 4:Pulsed THz wave generation pumped by femtosecond laser 65
4.1 Introduction 65
4.2 Generation mechanisms 66
4.2.1 Drude-Lorentz Model 66
4.2.2 Saturation behavior of Large aperture PC emitters 69
4.2.3 Saturation behavior of small-size PC emitters 72
4.3 Experimental systems 75
4.3.1 THz wave generation system 75
4.3.2 FTIR system for THz wave spectrum measurement 78
4.3.3 TDS system for THz wave spectrum measurement 80
4.3.4 Experimental setup for studying pulsed THz wave generation with CW background illumination 81
4.4 Results and Discussion 82
4.4.1 Photocurrent and THz power 82
4.4.2 THz spectrum 95
4.4.3 Pulsed THz wave generation with a CW background illumination 104
4.5 Summary 116
Chapter 5: CW THz wave generation pumped by two single-mode lasers system 119
5.1 Introduction 119
5.2 Mechanism of CW THz generation in photoconductive device 120
5.3 Experimental results and discussion 125
5.3.1 CW THz wave generation and detection system 125
5.3.2 CW THz wave and high-dose GaAs:O material 127
5.3.3 Comparison of Low-dose GaAs:O and LTG GaAs 132
5.3.4 Discussion on bias dependence behaviors 140
5.4 Conclusion 146
Chapter 6: Conclusions and future work 148
Publication list 155
References 156
Appendix: 165

List of Tables and Figures

Figure 1.1	Terahertz range within the e.m. spectrum. (from Nature Material)	1
Figure 1.2	Papers on "Terahertz" area during the past years	2
Figure 2.1	Energy band structure of GaAs	11
Figure 2.2	Schematic of Ion Implanter[44] and our real implantation facility (upper and left figures)	16
Figure 2.3	Ion distribution of Oxygen ion implanted GaAs	18
Figure 2.4	Facility of rapid temperature annealing	20
Figure 2.5	Band diagram of ion implanted GaAs showing the key excitation and decay processes in the rate equation	22
Figure 2.6	System of IR transmission measurement	24
Figure 2.7	IR Transmission of GaAs:O materials with different implant dosage after 400℃ annealing	26
Figure 2.8	IR Transmission of GaAs:O materials with different implant dosage after 500℃ annealing	26
Figure 2.9	IR Transmission of GaAs:O materials with different implant dosage after 550℃ annealing	27
Figure 2.10	IR Transmission of GaAs:Oe13 materials with different annealing temperatures	27
Figure 2.11	IR Transmission of GaAs:O2e14 materials with different annealing temperatures	29
Figure 2.12	IR Transmission of GaAs:Oe15 materials with different annealing temperatures	29
Figure 2.13	IR Transmission of GaAs(110):O materials with different dosage	30
Figure 2.14	Carrier concentration Vs Annealing Temperature for O^+ implanted GaAs	32
Figure 2.15	Resistance of GaAs:O materials Vs Annealing Temperature	33
Figure 2.16	Carrier mobility of GaAs:O materials Vs Annealing temperatures	35
Figure 2.17	The ionization energies for various impurities in GaAs	36
Figure 2.18	Time-domain photoreflectance system (Pump-probe system) for carrier lifetime measurement. (With permission from Prof.Chao-Kuei Lee of National Sun Yat-Sen University (NSYSU)).	40
Figure 2.19	Mechanism of photocarrier decay	41
Figure 2.20	The carrier lifetime of GaAs(110):Oe13 materials with different annealing temperatures. (a) the fast decay time constant, (b) the slow decay time constant	43
Figure 3.1	Dipole antenna structure. (Insert window is the photogap area of device	48
Figure 3.2	Process of photolithography	50
Figure 3.3	Photoresist Spin Coating	52
Figure 3.4	Photo of an alignment mark after development	57
Figure 3.5	Electron-Beam evaporation source	58
Figure 3.6	Photo of an alignment mark after lift-off step	59
Figure 3.7	Ultrasonic bonding process. (a) Tool guides wire to the package. (b) Pressure and ultrasonic energy form bond. (first bond) (c and d) Tool feeds wires and repositions, and ten form the second bond. (e) Wire broken at the bond.	61
Figure 4.1	Schematic of equivalent circuit of GaAs:O based PC antenna	73
Figure 4.2	Schematic of experimental setup for THz generation by fs laser pumping. (THz Power measurement)	75
Figure 4.3	The increase of detection efficiency with Si lens	77
Figure 4.4	Schematic of Martin-Puplett-type Fourier Transform Infrared Spectrometer (FTIR) System	78
Figure 4.5	Schematic of Terahertz Time-Domain Spectroscopy System	80
Figure 4.6	Schematic of experimental setup for studying pulsed THz wave generation efficiency as a function	81

	of CW background illumination	
Figure 4.7	I-V curve and Power-Bias curve of Dipole_1 (GaAs:Oe14 550℃, 195μm)	82
Figure 4.8	Electrical properties and THz generation performance of Dipole_2 (GaAs:Oe14 550℃, 95μm). (a) I-V curve; (b) THz power vs. Bias voltage; (c) Current vs. pump power; (d) THz power vs. pump power.	84
Figure 4.9	Saturation behavior of dipole_2 under 10V bias	85
Figure 4.10	I-V curve and Power-Bias curve of Dipole_5 (GaAs:Oe13 500℃, 95μm)	86
Figure 4.11	I-V curve and Power-Bias curve of Dipole_6 (GaAs:Oe13 500℃, 45μm)	87
Figure 4.12	I-V curve and Power-Bias curve of Dipole_7 (GaAs:Oe13 500℃, 40μm)	88
Figure 4.13	I-V curve and Power-Bias curve of Dipole_8 (LTG GaAs, 40μm)	88
Figure 4.14	Comparison of THz power generation performance of different devices. (a) Pump power dependence; (b) Bias dependence.	90
Figure 4.15	Peak power vs. Bias curve of Dipole_6 (GaAs:Oe13 500℃, 45μm) measured from TDS system	93
Figure 4.16	THz spectra of devices measured by FTIR method. (a) Dipole_1, (b)Dipole_3, (c)Dipole_5, (d)Dipole_6, (e)Dipole_2. (f)Spectra of devices in linear scale.	95
Figure 4.17	TDS measurement of dipole_1_2 (GaAs:O e14 550℃,195μm). (a) THz signal waveforms under different DC bias. Insert figure: curve of peak power versus bias. (b) THz spectrum of dipole_1_2 (under 100V bias, 55mW pump power). The light gray curve is from dipole_1 measured by FTIR method. Insert window: waveform of THz signal in time domain for dipole_1_2.	96
Figure 4.18	Spectra of dipole_10 (GaAs: As5e15,600℃,195μm). Insert: waveform of THz signal in time domain	98
Figure 4.19	Spectra of dipole_6 (GaAs:O e13 500℃,45μm). Insert: waveform of THz signal in time domain.	98
Figure 4.20	Spectra of dipole_7 (GaAs:O e13 500℃,40μm) and dipole_8 (LTG GaAs,40μm). Insert windows in (a) and (b): waveform of THz signal in time domain of dipole_7 and dipole_8, respectively.	99
Figure 4.21	The device (spiral antenna) for CW background illumination experiment.	101
Figure 4.22	THz power and photoinduced current under CW background illumination for device spiral_1 with 10mW fs laser pumping. (a) THz power vs. CW LD power; (b) Current vs. CW LD power.	102
Figure 4.23	The effect of CW LD background illumination on pulsed THz wave generation versus the photocurrent induced by the CW LD illumination	103
Figure 4.24	The Change of THz power versus CW LD power or DC bias voltage for device spiral_1. (a)The modulation ratio of THz power vs. CW Laser diode power; (b)The modulation ratio of THz power at different bias voltages.	104
Figure 4.25	THz power and modulation ratio under CW background illumination for device spiral_4 with different fs laser pumping power. (a) THz power vs. CW LD power; (b) The modulation ratio of THz power vs. CW LD power.	105
Figure 4.26	THz power of spiral_3 under different bias voltages vs. fs laser power. Open square represents the modulation ratio under 5V bias and 30mW CW LD illumination (right y axis)	106
Figure 4.27	The modulation ratio of THz power under different bias voltages for device spiral_4. The solid symbols and open symbols are for 10mW and 20mW fs laser pump powers respectively.	106
Figure 4.28	THz power of spiral_2 and spiral_5 under different illumination power of CW laser diode: (a)spiral_2 and (b)spiral_5. THz power modulation ratio vs. bias voltage: (c)spiral_2 and (d)spiral_5.	107
Figure 4.29	Simulation results of the screening effect under CW background illumination for device spiral_1 tested under 10mW fs pumping.	112
Figure 5.1	Interdigitated electrode configuration of photomixer	117
Figure 5.2	Equivalent circuit of PC device (Photomixer)	119

Figure 5.3	THz power vs. beating frequency (simulation results)	121
Figure 5.4	Schematic of experimental setup for CW THz generation with two single-mode lasers system. (Measure output power and other electrical parameters.)	122
Figure 5.5	Photocurrent of dipole_1 under the pumping of two CW laser beams	124
Figure 5.6	CW THz power of dipole_1. The beating frequency is set at 0.327THz. Dash lines are the curve fitting with quadratic law	124
Figure 5.7	Power of CW THz waves generated by dipole antenna fabricated on GaAs(110):Oe14 material. Insert shows the spectrum of THz wave generated by the same device under pulsed mode measured by FTIR System.	125
Figure 5.8	Performance of CW THz wave generated from Dipole_4_2 under 70V bias and 45mW pumping condition.	127
Figure 5.9	CW THz power and photocurrent of dipole_9 (LTG GaAs) under 35mW pump. The red dash line is the fitting curve with quadratic law.	128
Figure 5.10	Current and CW THz power of dipole_4_2 (GaAs:Oe13) and dipole_9 (LTG GaAs). (a) IV curve measured under 45mW CW pump power @ 0.359THz, (b) The ratio of photocurrent to dark current vs. bias voltage (solid symbols) and CW THz power under different bias voltages (open symbols).	129
Figure 5.11	Photocurrent (open symbol) and CW THz output power (solid symbol) under different CW pump powers for dipole_4_2 (GaAs:Oe13) and dipole_9 (LTG GaAs). The beating frequency is set at 0.359THz	130
Figure 5.12	CW THz signal vs. beating frequency. (a) Normalized CW THz signal; (b) Original data in linear scale with Gaussian fitting curves [dash line for Dipole_4_2 (GaAs:Oe13) , dot line for Dipole_9 (LTG GaAs)].	131
Figure 5.13	Schematic of experimental setup for CW THz generation with two single-mode lasers system. (CW light is amplified by MOPA to around 180mW.)	132
Figure 5.14	Photocurrent and CW THz output power of dipole_4_2 (GaAs:Oe13) and dipole_9 (LTG GaAs) under high CW pumping power (180mW). The beating frequency is set at 0.358THz. (a) Photocurrent (b) CW THz output power (1mV≈0.119μW). Insert window is the linear scale for CW THz output power	132
Figure 5.15	Simulation results of CW THz power under different bias voltage [solid line is GaAs:Oe13 (dipole_4_2) and dash line is LTG GaAs (dipole_9)]. Solid symbols are the measured values.) Insert window (left) is for photocurrent and CW THz wave of GaAs:Oe13 and Insert window(right) is for those of LTG GaAs. (lines are fitting curves)	136
Figure 5.16	CW THz power versus Photocurrent for GaAs:Oe13 and LTG GaAs devices	139
Figure a.1	THz wave generation from the fiber based system. (1550nm for InGaAs)	159
Figure a.2	Signal transmission in space.	162
Table 3.1	Parameters of dipole antennas and their calculated resonance frequencies.	49
Table 3.2	Parameters for photolithography	63
Table 3.3	Devices and their parameters	64
Table 4.1	Resonance frequency and bandwidth of devices measured by FTIR or TDS	100
Table a.1	Pulsed THz wave generated by LTG InGaAs based PC devices under 1550nm fs fiber laser pumping.	160

List of Abbreviations and Symbol

BWO	Back Wave Oscillator
CW	Continuous wave
FBG	Fiber Bragg Grating
fs	Femtosecond. Time unit, =10-15 second.
FTIR	Fourier transform infrared spectrometer
LTG	Low Temperature Grown
MOPA	Master Oscillator Power Amplifier
M-P	Martin-Puplett
MBE	Molecular Beam Epitaxy
MOCVD	Metalorganic chemical vapor deposition
OPO	Optical parametric oscillator
PBS	Polarization beam splitter
PC	Photoconductive
PCB	Printed circuit broad
ps	Picosecond. Time unit, =10-12 second
QCL	Quantum cascade Laser
RBS	Rutherford backscattering spectrometry
RTA	Rapid Temperature Annealing
SI	Semi-insulating
SNR	Signal-to-noise ratio
SRH	Schockley-Read-Hall
SRIM	Stopping and Range of Ions in Matter
TDS	Terahertz Time-Domain Spectroscopy
TRIM	The transport of Ion in Matter
UTC	Uni-traveling-carrier
VCSEL	Vertical-cavity surface-emitting laser

A	The illuminated area of the emitter

α_b, α_{trap}	The band-to-band absorption coefficient, and the absorption coefficient from the traps to the upper excited states in the conduction band, respectively
$\Delta\alpha$	The change of absorption efficiency of material
β	The two-photon absorption coefficient
C	The capacitance of the light incident area
c, ε_0	Light speed and the permittivity of free space, respectively
d_{pre}	The precipitates cross section
d_{dep}	The extent of the depletion region
d_{gap}	The distance between the two terminals of antenna (metal electrodes)
e	The elementary charge
E_g	The bandgap energy
E_{THz}	The Terahertz radiation field
E_{opt}	The measured average optical energy
E_{loc}	The local electric field
E_{sc}	The space-charges field
E_b	The applied electric bias
E_{gap}	The electric field added on the photogap
E_a	The radiation screening field
f_r, λ_r	The resonance frequency of a dipole antenna and its resonance wavelength
I	The intensity of incident light

$I_{opt}(t)$	The incident optical pulse intensity
$I_{DC,ph}$	The Dc photocurrent
$i(t)$	The photocurrent
J	The transient photocurrent density
J_s	The surface current
L_{ae}	The effective length of dipole antenna
L_s	The separation of two strip lines
l	The thickness of semiconductor absorption layer
m_e, m_h	The effective electron mass and hole mass, respectively
m^*	The effective mass of carrier
m	The mixing efficiency which ranges in value between 0 and 1
N_{band}	The population of carrier at the bottom of the conduction band
N_{trap}	The population of carriers in the trap centers
N_{inner}	The population of carriers in the excited states within the conduction band
$N_{band(0)}$	The saturation carrier density near bandgap in conduction band
$N_{trap(0)}$	The saturation carrier density of defects which act as trapping centers
N_{def}	The point defect trap density
n_{def}	The occupation of the point defects states
N_{pre}	The number density of precipitates
n	The carrier density
P_{sc}	The space-charge polarization
P_0	The total incident power averaged over a long time period, $P_0=P_1+P_2$. P_1 and P_2 are average power of two single-mode CW laser beams.
R_L	The load impedance of antenna
R	The optical reflectivity
μ_{eff}	The effective carrier mobility of materials
v	The carrier velocity

υ_{th}	The thermal velocity of the electrons
W_s, W_a	The width of stripline and antenna (electrode),respectively
$Z_{gap}(0)$	The impedance of photogap
Z_0	The characteristic impedance of the free space, about 377Ω
Z_a	The impedance of antenna
η_e, η_i	The external and internal quantum efficiency, respectively
η_{geo}	The geometrical factor of material
$\hbar\omega$	Light which photon energy
τ_1, τ_2	The decay time for exited carriers to recombine by jumping back to the valance band from conduction band, and the decay time for the exited carriers to be trapped in the mid-gap states, respectively
τ_f, τ_s	The fast decay time constant and the slow decay time constant
τ_{trap}	The carrier trapping time
τ_s	The momentum relaxation time
τ_r	The carrier recombination time
$\tau_{carrier}$	The lifetime of the excited carriers
τ_{drift}	The carrier drift time in a bias field
τ_p	The pulse width of the radiated field
σ_b, σ_{trap}	The cross section for band-to-band transitions and the cross section for absorption from the traps to the excited states in the conduction band, respectively
σ_s	The surface photoconductivity
σ_c	The capture cross section of each point defect
ε_s, κ	The relative static dielectric constant of the material and a fitting parameter, respectively
ε_e	The effective dielectric constant, $\varepsilon_e=(1+\varepsilon_d)/2$, where ε_d is the dielectric constant of the substrate material
ε	The permittivity of the substrate
λ	The wavelength of injection light
ΔN, ΔP	The concentrations change of free electrons and holes
χ, χ_{cr}	The concentration of free electron or holes and The critical concentration of free carriers, respectively

Chapter 1: Introduction

1.1 Background

Terahertz wave is the electromagnetic wave which is located between microwaves and infrared light (see Figure 1.1). The range from 0.1 THz to 10 THz is named as THz gap, where 1 THz is equivalent to 33 wave numbers or 300 um or 4mev.

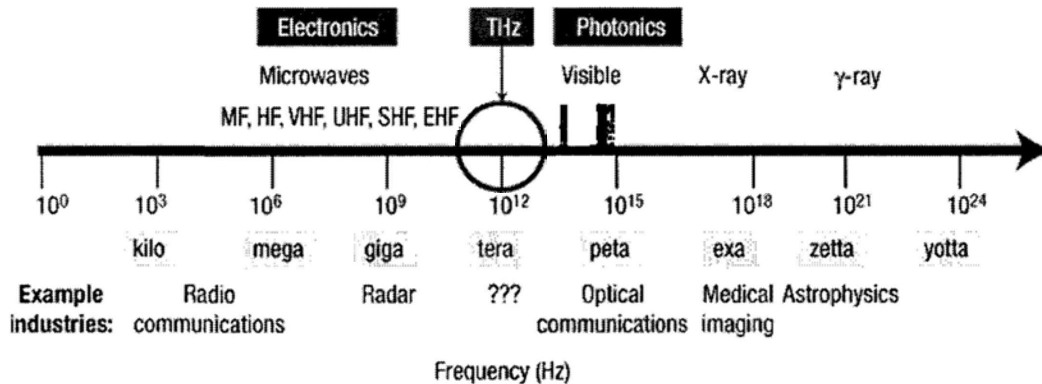

Figure 1.1: Terahertz range within the e.m. spectrum. (from Nature Material[1])

Terahertz wave is harmless to biological cells (like human body), because its corresponding low photon energy (4 meV @ 1 THz, around one million times weaker than an X-ray photon) will not cause the damage associated with ionizing radiation such as X-ray. This leads T-ray diagnostic technique to be an interesting complement to X-ray radiography technique (ionizing radiation). As each material has its own intrinsic absorption and reflection characteristics in the THz region, such kind of spectrum could be used for their identification. Another property of terahertz wave is that, it is highly transparent to most non-metallic and non-polar mediums (like paper, plastics), but highly reflected by metal and absorbed by liquid (like water) or vapor. This kind of behavior can be used to see though package and find metal inside, without causing any damage on the package (nondestructive detection). So, terahertz wave have tremendous applications in biomedical science (like skin cancer detection[2], DNA analyzer[3]) , THz imaging[4] (security screening in airports[5], mail inspection[6]), materials science (semiconductor[7],

drugs[8]), high speed communications[9, 10], and Astronomy[11].

Because of these special properties and their tremendous application area, "Terahertz" comes to be a very hot word in the eyes of scientists and researchers. The research papers on "Terahertz" research area increase dramatically during the past 20 years, especially the past ten years (see Figure 1.2).

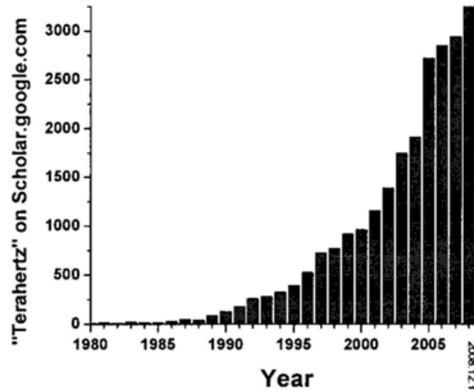

Figure 1.2: Papers on "Terahertz" area during the past years.

The most important element of terahertz science (technology) is terahertz source. Without a suitable terahertz source, those potential applications can't come to be reality. Normally, the terahertz sources can be classified into two branches. One is broadband (Pulsed) terahertz sources, and the other is narrow band (CW) terahertz sources.

The broadband terahertz wave can be generated by a number of different mechanisms, including photocarrier acceleration in photoconductive (PC) antennas[12], optical rectification[13], plasma oscillations[14] and electronics non-linear transmission lines[15], or even just from air (plasma)[16]. With such kind of broadband source (bandwidth could be as high as 4 THz[17]), one can obtain the THz spectrum of materials just by one round scan (about kHz scan rates[18]). The common used spectroscopic tool is the well known "Terahertz Time-Domain Spectroscopy (TDS)". In a TDS system, the THz wave is measured coherently, which provides both high sensitivity and time-resolved phase information.

Nowadays, most of those approaches list above need an ultrashort (femtosecond) laser (for example, mode-locked Ti:sapphire laser), which limits the size of the whole system to be compact. But, fortunately, the evolution of fiber based fs laser provides the possibility of miniaturization for broadband THz source (Mini-Z 1000[19]).

Unlike broadband THz source, whose spectral resolution is about 50 GHz, the narrow band (CW) THz source provides a chance to study material spectrum with a resolution around 4 GHz [20]. The narrow band terahertz wave can be generated by different approaches. For examples, the photomixing technique using photoconductive antenna, optical parametric oscillator (OPO)[21], Back Wave Oscillator (BWO)[22], Gunn diode[23], and Quantum cascade Laser (QCL)[24]. Among them, the photomixing approach combines the advantage of both electric and optical technologies: room temperature operation, narrow linewidth, compactness, and wide-range tenability).

As PC devices can generate both broadband THz wave (photocarrier acceleration) and narrow band THz wave (photomixing), the photoconductive method comes to be one of the most popular approaches for THz wave generation used in laboratory experimental setup or commercial systems. The photoconductive approach uses high-speed photoconductors as transient current sources for radiating antennas. For example, LTG GaAs [25], ErAs:GaAs [26] for 800nm light, and LTG InGaAs, InGaAs:Br+ [27] for 1550nm light. As the dark resistivity of materials corresponding to 1550 nm light is several orders smaller than those materials for 800nm light, there are still a lot of spaces for them to improve. Therefore, the 800nm pumped PC devices (materials) are still in the dominative status.

Among them, LTG GaAs is the common used material for 800nm pumping PC devices, for its advantages of high dark resistivity ($>10^6$ Ωcm [28]) , short carrier lifetime(0.25 ps[29, 30]), high carrier mobility (200 μm/V·s [31]), and high breakdown voltage($>5\times10^5$ V/cm[32]). However, these excellent characteristics are difficult to be reproduced from sample to sample, because the quality of the LTG

GaAs depends critically on both the preparation temperature and the post thermal annealing conditions. Some materials grown by ion implantation method have the potential to be the good complement of LTG GaAs, because the precise control over ion dosage and implant energy helps ion implantation method to overcome the reproducibility limitation of LTG GaAs.

In recent years some ion implanted semiconductors (GaAs:As [33], GaAs:H [34, 35], GaAs:N [36]) have caught a lot of attention and been studied as the possible substitute materials for LTG GaAs. For example, Salem et al.[37] implanted O+ ions to optimize the GaAs and generated Pulse THz wave from it. And, Mayorga et al. [38] used high energy oxygen implanted GaAs to generate CW THz wave.

As the energy level formed by oxygen ions in GaAs is close to the Fermi level, it makes the O+ implanted GaAs almost electrically neutral, and hence a comparatively higher resistance.

This thesis aims to do further study on such kind of oxygen ion implanted GaAs material and its THz wave generation properties under both pulsed and CW mode (Broadband and narrow band).

Before embarking in a detailed study of GaAs:O and related PC devices, one should know what the advantage of GaAs:O materials is, and also its disadvantage. Its first advantage comes from its preparation method. The ion implantation method has two main advantage compared with the Low temperature MBE (Molecular Beam Epitaxy) or MOCVD (Metalorganic chemical vapor deposition). One is its reproducibility. User can easily repeat the preparation condition time by time, without changing too much in the material characteristics from sample to sample. The other one is its tailor ability. The properties of material can be tailored by selected suitable implant energy, ion dosage and the post annealing temperature. With this kind of preparation method, one can grow materials with certain characteristics easily, according to his (her) own purpose. And, as the oxygen is common component of air, it is easy to be found and extracted for implantation usage comparing with other kind of ions, which need to be bombarded out from

bulk material or powder. And oxygen is harmless (nontoxic) and cheaper comparing with those ions like As+, Er+, and therefore it will cause less risk on Environmental pollution

The defects caused by the O+ ion in GaAs material endows other advantages for GaAs:O materials, as listed in the following:

1. High dark resistance. As mentioned above, the energy level formed by Oxygen ions in the material is close to the Fermi level, which makes the material close to electrical neutral. The general resistivity of GaAs:O can be as high as $10^6\Omega$cm.

2. A reasonable carrier lifetime (in subpicosecond range). O+ ions form lots of defects (carrier trapping center) in the GaAs material during the implantation process. The higher defects concentration in it, the shorter carrier lifetime (carrier trapping time) it will have.

3. High saturation level. The existing of O+ defects increases the saturation level of GaAs:O material. Comparing with LTG GaAs material, GaAs:O has higher pump power saturation level and bias field saturation level. These allow one to add higher pump power and bias onto the PC devices, which at the end generate higher output power of THz wave.

Although there are lots of advantages discussed above, there still exist some imperfect aspects, for examples:

1. The dosage layer is close to the surface. It is difficult to get deeper into the inner of substrate (material), which limited by the implant energy and the atom mass of ion. For example, implant energy 1200 keV can only achieve 1.4 μm depths for O+ ion in GaAs substrate. (One should be mentioned, the real peak of ion concentration after post annealing process should be thinner than the original one just after implantation process.) And the implantation time will increase with the implantation energy dramatically, because of the decreasing of implant ion current. This, at the end, will cause the cost of material preparation to increase.

2. The ion distribution can not be very uniform by mono-implantation, even

after annealing process, which forces one to do multi-implantation if he (she) needs a good uniform ion distribution profile. Then it will double or triple the time of the growing process, supposing the multi-implantation process includes two or three different implant energies.

Although there some imperfects exist, considering its advantages the oxygen ion implanted GaAs material (GaAs:O) is still a very interesting material for THz PC devices. In the material preparation area, one can optimize the ion implant energy, ion dosage and annealing temperature, to improve the performance of GaAs:O material for THz generation. Because the material's resistivity and carrier lifetime are sometimes on the opposite direction (which both are critically related to defects concentration, but with reverse proportional), the best preparation condition of those three parameters for carrier lifetime maybe is not the best one for resistivity. Therefore, it needs one to balance the requirement of these two factors in a certain case, and select the best preparation condition for both of them (a compromise between carrier lifetime and resistivity), by sufficiently testing of the performances of GaAs:O materials grown under different conditions.

To minimize the effect of those imperfects discussed above, one could do much simulation work to design the multi-implantation process before going into the real operation process.

As mentioned above, in THz generation area, GaAs:O material has been demonstrated in pulsed generation mode by B.Salem, et al.[37, 39] (A group in Canada). They used multi-implanted GaAs:O with a dosage level $10^{13}cm^{-2}$ to study its THz wave generation performance, and compared it with other kinds of ion-implanted material, such as GaAs:As, GaAs:H, and GaAs:N. But they haven't compared the generation performance of GaAs:O with LTG GaAs, which occupies the dominative position of PC devices at 800 nm pumping range. And they haven't gone further and compared the effect of dosage in the power generation and THz spectrum. There still lots of space were left for one to do further study on this area, even without including the possible application using GaAs:O based PC devices

Following their work, we have demonstrated our partial study work on GaAs:O based THz PC devices in pulsed generation mode [40], and the CW THz generation mode in the middle of 2007[41],which will be discussed in the Chapter 4 and 5, respectively. For CW terahertz generation from GaAs:O, it is almost at the same time (a little early than ours), another group from Germany, I.Camara Mayorga et al. [38] published their very detailed study works on the high energy ion (2 and 3 MeV) implanted GaAs:O material. It should be cheerful that on this road we are not lonely. They have compared the THz wave generation performance of GaAs:O material not only with different implant energy and dosage, but also other material like GaAs:N. Their hard work promotes the study on GaAs:O material in CW THz area to a new high level. But, unfortunately, they also haven't compared its performance with LTG GaAs materials.

For one who is interested in the properties of GaAs:O in terahertz generation area, there are still a lot of study directions can be gone deeper. For example, THz generation performances comparing with LTG GaAs, the saturation behavior and its material reason, maximum output power of THz wave from GaAs:O based PC devices, the screening behavior under CW background illumination. And others like the generation performance optimizing, system compacting, and the special applications are also the valuable research areas for GaAs:O based PC devices.

1.2 Aim of this work

A compact, high power and low cost terahertz source is something what desired for laboratory and commercial usage. Terahertz photoconductive device is one of best choices, if they can combine with fiber laser or diode laser, which are normally compact and low cost comparing with solid laser. As introduced above, a high reproducibility method for material preparation is also a very important factor to the aim of low cost. The ion implantation method and Oxygen ion type give one not only an easy way to reproduce high quality material samples to samples, but also

the possible very good properties of materials. So, this thesis aims to do further study oxygen ion implanted GaAs material and its properties in terahertz generation area, especially focusing on the THz output power (both pulsed mode and CW mode). The related pump light saturation and bias saturation behaviors, and the effect of DC current on THz generation (Screening of CW background illumination) will also be studied to construct this thesis. To best exhibit the special performances of GaAs:O material in THz area, as much as possible comparison will be carried out between different preparation condition, or between different materials (especially with LTG GaAs). Some different antenna structures will also be adopted in this work.

1.3 Organization of the thesis

The structure of this thesis is as follows:

In Chapter 2, the ion implantation method and its parameters selection are discussed at first. The approach used to recover some crystal lattice damages, which were induced by the ion implantation process, is also mentioned in this part. Considering the energy states created by the defects in material after implantation process, a set of rate equations for carrier dynamic is introduced to analysis the light absorption characteristic of GaAs:O material. At the end, to optimize the preparation condition, some important materials properties like the carrier concentration, resisitivity, carrier mobility and the carrier lifetime were tested with different ion dosages and annealing temperatures.

Chapter 3 deals with the devices fabrication on GaAs:O substrate. Dipole and spiral antenna structures are selected for this work. The common photolithography technology is used to transform the pattern onto the material surface, and electron beam Evaporation forms the Ti/Au metal layer. After packaging, the wire bonding technology gives the wire connection to the device with external circuit.

Chapter 4 reviews the physics of pulsed THz generation. Three theoretical

models are introduced on the different focusing aspects, especially on saturation behaviors. Two series of GaAs:O materials with different dipole antenna structure were studied for their performances on photocurrent, THz power generation, THz spectrum (measured by Fourier transform infrared spectrometer (FTIR) or Terahertz Time-Domain Spectroscopy (TDS) system), comparing with LTG GaAs and GaAs:As. At last, the effect of DC current on output power of pulsed THz wave was studied under CW background illumination. A theoretical model was suggested to describe such kind of screening behavior.

In Chapter 5, two single-mode lasers system was setup for generating CW THz wave by photomixing (optical heterodyne downconversion) mechanism. Three kinds of materials (GaAs:Oe14 [500keV/6×10^{13}cm^{-2}+800keV/6×10^{13}cm^{-2}+1200keV /1×10^{14}cm], GaAs:Oe13 [500keV/2.5×10^{13}cm^{-2} + 800keV/2.5×10^{13}cm^{-2} +1200keV /4×10^{13}cm^{-2}] and LTG GaAs) based PC devices are studied in this Chapter. To understand the bias dependent saturation behavior better, a CW pumping power as high as 180mW is used to enhance such kind of phenomenon, and the comparing testing was launched between low-dose GaAs:Oe13 and LTG GaAs based PC devices. At the end, a modified theoretical model is used to simulate this kind of behavior and explain the possible reason in physics.

Chapter 6 gives a summary on the whole work and launches a brain storm on the future work (material, device, system, and application). Some ongoing research works are also introduced in this part.

Chapter 2:
Material preparation and Characteristics

A material with high dark resistance, short carrier lifetime, high breakdown voltage and high power saturation level is desired for THz Photoconductive devices. High dark resistance means one can get high signal-to-noise ratio (SNR) of THz wave from such kind of materials, because the background electrical current will be at a low level. Material with short carrier lifetime means that it could respond very fast to the modulation signal, and can generate THz wave with more high frequency components. And, the high breakdown voltage and high pump power saturation level means the devices could be driven by higher applied electric field and higher optical pumping power, which at the end could help devices to generate higher output power of THz wave. This Chapter aims to prepare such kind of good performance material by ion-implantation method.

2.1 Introduction

The carrier lifetime of direct bandgap materials (for example, GaAs) is generally shorter than those of indirect bandgap materials (for example, Silicon). Figure 2.1 shows the energy band structure of GaAs. When incident light photon is absorbed by materials like GaAs, electron-hole pair will be generated. The electrons will jump into the Γ-valley, and in a short time the excited electrons will jump back and recombine with hole and emit a photon. This process would be very fast as it doesn't need a change in crystal momentum for the electron. But, in indirect materials like Silicon, a change of crystal momentum is required in such a transition, which increases the duration. The carrier lifetime of GaAs is on piscosecond (ps) level, but it is nanosecond (ns) or microsecond (μs) level in Silicon.

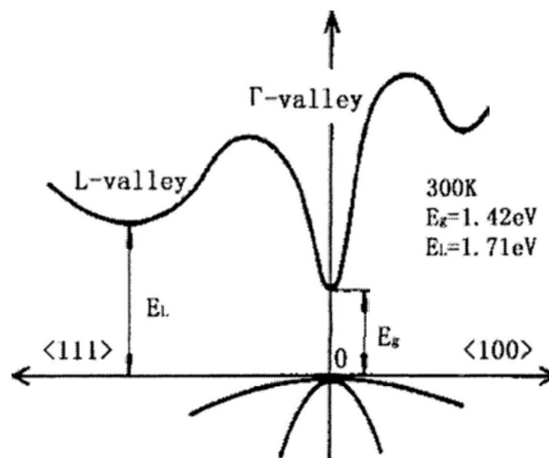

Figure2.1: Energy band structure of GaAs

Although GaAs material has short carrier lifetime in ps level, but such level is not enough for high frequency terahertz wave generation. Only material with carrier lifetime lower than 1 ps could be used to generate >1 THz components. So, the common used material for terahertz photoconductive devices is Low temperature grown (LTG) GaAs, as it accumulates lots of As^+ defects during the low temperature grown process. The existing of these abundant As^+ defects endows LTG GaAs material with good performances on dark resistivity, carrier lifetime and breakdown voltage [26]. But the preparation condition of LTG GaAs is not easy to repeat time by time, for the difficulty of precise temperature control for the low temperature preparation process.

Another approach is to induce high density defects by implanting some suitable ions into the semi-insulator materials. The collision of incoming ions with the lattice atoms forms varies defects such as vacancies, interstitials, antisites, etc, so that the material can exhibit similar carrier trapping mechanism as in LTG GaAs. The ion implantation technique can allow user to control ion dosage precisely, which allows a reproducible properties of the ion-implanted materials. Ion implantation can also generate depth-dependent damage profiles by choosing the ion species, dosage, and implanting energy in the specific sample areas.

As^+ ion should be the ion species which scientists will firstly consider for preparing the ion implant GaAs, because after implantation process the chemical

composition of GaAs are the same as LTG GaAs, therefore its performance should be similar to LTG GaAs[33]. Other ions like H^+, He^+, N^+ and O^+ are also utilized by scientists in these years.[34-37]

In this thesis we will focus on O^+ ion, for the energy level of oxygen ion in GaAs is close to Fermi level[42], which makes the oxygen ion implanted GaAs material close to be electrically neutral and have comparative high resistance.

The ion distribution was simulated with software "Stopping and Range of Ions in Matter" (SRIM) [43]. For light with wavelength 800nm, the absorption depth is around 1μm in GaAs materials. Considering the condition of our high energy ion implanter (a Rutherford Backscattering Spectrometry (RBS) facility from HVEE) and the requirement of uniform ion distribution profile, we performed a multi-implantation process with different implant energies.

After selecting the ion implant energies by SRIM simulation, we plan the ion dosage needed for the materials. The carrier lifetime is generally related to the intrinsic characteristics of material such as energy band structure, or the density of the defects which embedded by manual work (for example, ion implantation). For general Semi-insulating (SI) GaAs, the carrier lifetime does not reach the sub-ps range, so we need to create more additional defects in it by ion implantation method. If just considering the carrier lifetime, higher dosage will be better choice. We also have to take care of the other performances of material, like resistivity. If the startup material is Semi-insulating, the material resistivity is normally inversely proportional to the concentration of defects. Although the O^+ implanted GaAs should be close to electrical neutral, it is still act as slight N-type. (The detail will be discussed in "Chapter 2.4 Material properties"). So, we prepare our GaAs:O samples with different dosage-energy sets. For example Oe13, Oe14, O2e14 and Oe15 (Their detailed definition will be showed in Chapter2.2.5), each set is a combination of implant energies and implant dosage. The implantation process detail will be presented in "Chapter 2.2 Process of Implantation".

After implantation process, a post annealing process was taken. The annealing

temperature is a critical parameter, because the small changes of this parameter will cause great effect on dark resistance, mobility and carrier lifetime. So, several annealing temperatures were tested for optimizing the properties of GaAs:O samples in this thesis. The detail can be described in "Chapter 2.3 Annealing process".

The performances of GaAs:O materials will be characterized in "Chapter 2.4 Material properties". In that part, light absorption, resistivity, free carrier mobility, the concentration of free carrier and carrier lifetime will be measured and discussed. A theoretical mode would also be introduced to explain the change of light absorption and the relationship of defects concentration and absorption efficiency.

Finally, an optimized condition of material preparing would be presented.

2.2 Process of Implantation

Ion implantation and diffusion are the two key methods for impurity doping. Since the early 1970s, many doping operations have been performed by ion implantation. In this process the doping ions are implanted into the substrate by means of an ion beam. Comparing with diffusion, the main advantages of ion implantation are its more precise control on the account of dopant and the location of dopant, and reproducibility of impurity doping, and its lower processing temperature comparing with diffusion process. [44-46]

Ion implantation is one of the simplest methods for synthesis a surface layer with particular properties in selected regions (normally its depth is limited to the order of a micron.). The user has to decide which electrical, optical, chemical, mechanical properties are required in decided area of the surface. After choosing suitable chemical composition, a well selected injection energies and implantation time will help to get desired properties in certain depth with designed ion dosage.

2.2.1 The advantage of ion implantation

Besides those advantages mentioned above, ion implantation also have lots of other

inherent merits [44]. As it is a method to introduce impurity atoms into the substrate at a high velocity, the modified new layer on the surface of semiconductor is not formed in thermodynamic equilibrium. This is very useful because normal chemical solubility rules are by passed. And the ion paths are also not straight because of the collisions. As the number of collisions per unit distance and the energy lost per collision are random variables, there will be a spatial distribution of ions having the same mass and the same quite possible to achieve impurity levels, which are impossible to be achieved by conventional treatments.

Chemical doping by an ion beam is a "clean" method. With accelerators and high resolution mass separators, it is quite feasible to implant a single isotope. The simplicity with which atoms can be added to a semiconductor also implies that a second or a third impurity can be added under certain controlled conditions without causing problems like material decomposition or the accidental incorporation of unwanted impurities.

By ion implantation method, a precisely controlled dosage can be achieved as the designed concentration of defect or impurity sites in the surface layer of the semiconductor. This will let the user to get subtle control of properties which result from the changes in the Fermi level.

As the ion implantation produces extensive damage and creates lots of defects in the implanted layer, generally, the minority-carrier lifetime and mobility are severely degraded after ion implantation. So with this method, one could obtain some material with ultra-short carrier lifetime for fabricating high speed devices, for example, THz PC devices.

2.2.2 Ion range and ion stopping

Implantation energies are normally between 1 keV to 1 MeV (some high-energy implanters can reach 5 MeV), resulting in the ion distribution with an average depths ranging from 10nm to 10μm for silicon. Ion doses vary from 10^{12} ions/cm^2 for threshold voltage, to 10^{18} ions/cm^2 for the formation of buried insulating layer.

When ion pass through a solid (semiconductor material), they collide with electrons and nuclei, then lose their energy and come to rest within the solid after a distance. The average depth of ion implantation can be controlled by adjusting the acceleration energy.

From Lindhard, Scharff, and Schiott (LLS) range theory [47], the major reasons of energy loss which lead to the incident ion stopping are caused by the following two mechanisms. The first is by transferring its energy to the target nuclei. This kind of collision will cause deflection of the incident ion and also dislodge many target nuclei from their original lattice sties, thereby create damage in the semiconductor lattice. So, a subsequent annealing treatment is needed to remove this kind of damage. The second stopping mechanism is by the interaction between the incident ion and the cloud of electrons surrounding the target's atoms. The ion loses its energy in collisions with electrons through Coulombic interaction. The electron which gained energy from incident ion will be excited to higher energy levels (excitation), or be ejected from the atom (ionization).

2.2.3 Structure of ion implanter.

Figure 2.2 shows the schematic of implanter and our real implantation facility. The ion source of implanter is a hot filament plasma source which ionize the source gases or solids into charged ions [46]. An extraction voltage, around 12 keV (our facility), extract the charged ions from the ion source chamber to the mass analyzer. The magnetic filed of mass analyzer is set to allow the ions with desired mass-to-charge ratio to travel through without being filtered. The selected ions then are accelerated under high voltage to get desired implantation energy in the acceleration tube. A focusing system is just next to the acceleration tube to achieve good collimation of the ion beam. The neutral beam trap and beam gate is used to separated neutral beam and charged ion beam. With an electrostatic deflection system, the ion beam is then scanned over the wafer (semiconductor samples) surface, and is implanted into the semiconductor substrate. To minimize the ion

scattering by gas molecules on the path of ion beam, the implanter is normally operated at a pressure below 10^{-4} Pa.

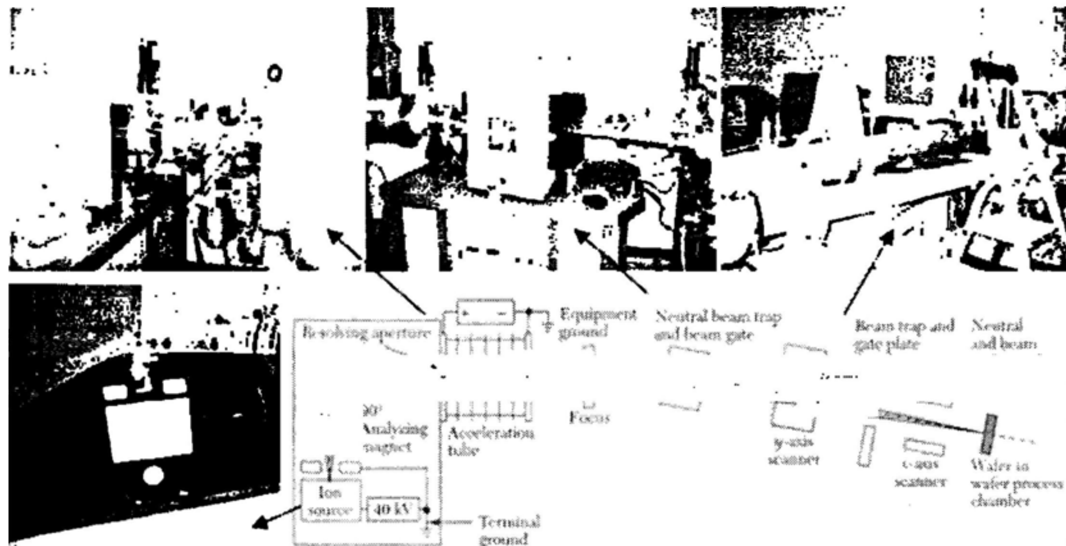

Figure2.2: schematic **of Ion Implanter [44] and our real implantation facility (the upper and left figures)**

2.2.4 Selection of Implantation conditions

For THz photoconductive (PC) devices, the materials should have better performances on the response speed, dark resistance, break voltage, and quantum efficiency, etc. By selecting suitable ion type and using various combinations of ion implantation energy and dosage, we can satisfy some of those requirements by ion implantation method.

For example, the response time is normally related to the carrier lifetime, which directly related to the concentration of defects. To get short carrier lifetime, we can fulfill this requirement by increasing the ion dosage during the ion implantation process. For ultrashort carrier lifetime in ps level, the dosage of ion of $10^{13}/cm^2$ level should be the least value. For a given absorption coefficient, a sufficiency thick absorption layer is needed to utilize most of power of incidence light. To increase the light efficiency, one method is to increase absorption coefficient, the other is to increase the thickness of absorption layer. For GaAs materials pumping by 800nm photon, the absorption depth is around 1μm. So the depth of ion implantation is also required to be near 1μm. To achieve such depth, an implant

energy as high as 1MeV should be used for O^+ ions.

As the ion implantation process is a huge time and money cost work, the simulation work is compulsory to evaluate the possible results after ion implantation and optimize the preparation parameters before going on the real ion implantation process. A free software "Stopping and Range of Ions in Matter" (SRIM) can be download from website authored by James F. Ziegler [43] .

The transport of Ion in Matter (**TRIM**) program in the SRIM software is a program using Monte-Carlo calculation method which follows the ion into the target, making detailed calculations of the energy transferred to every target atom collision. It can calculate both the final 3D distribution of the ions and also all kinetic phenomena associated with the ion's energy loss: target damage, sputtering, ionization, and phonon production.

By calculating the 3D distribution of ions with TRIM program, we can optimize the ion implant energy and ion dosage for our case. As the mono-implantation will create an ion distribution profile with a comparable shape peak, it means the characteristics of material in such layer are not uniform. To get a relative uniform profile of ion distribution, a multi-implantation process is required. With the help of multi-implantation method, we could form a flat doping profile to keep uniform material properties in certain thickness of new growth layer. And, such kind of multi-implantation method can also help to obtain a well controlled doping profiles which unavailable from diffusion technique by using various combination of implantation energy and implant dosage.

As we know the absorption depth is around 1μm in GaAs materials for light wavelength of 800nm. So to fully utilize the pumping light power, a uniform implant layer thicker than 1μm should be required. By simulation with STRM program, we found the ion range of oxygen in GaAs, for 500 keV is around 0.7μm, 800 keV is 1μm, and 1200 keV is close to 1.4 μm. Although the simulation result of depth is deeper than 1 μm for 1200 keV energy, the ion distribution will be close to (or litter deeper than) the depth which we designed (from surface to absorption

depth) after the post annealing process.

To get a uniform defects distribution layer, we should utilize multi-implantation method to optimize the defects distribution profile. By combining 500 keV, 800 keV and 1200 keV implant energy with different dosage (relative dose), we can obtain an optimized simulation results as shown in Figure 2.3.

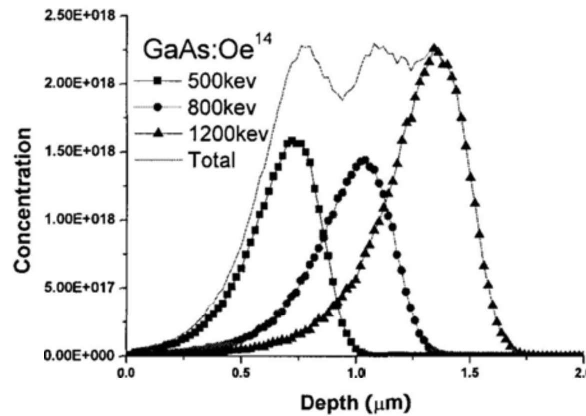

Figure2.3. Ion distribution of Oxygen ion implanted GaAs

Note: In this work, as the lowest implant energy is 500keV, O+ ion distribution has lower value in those areas just below the surface of material, although after implantation the redistribution process can happen during the annealing process. To improve this, one can add a lower implant energy process into the implantation process, or use some etching solution to slightly etch out such layer.

The implant dosage for each implant energy level should be based on the requirements of THz PC devices. Then, what level of defects we need? From the experiments, around $10^{18}/cm^3$ level is usually needed to achieve ultrashort carrier lifetime. If the dosage is too low and the annealing temperature is high, the defects what the implanted ion created would not be enough after annealing process. If using too large dosage, some unwanted events will appear. For example, too high dosage could bring some unwanted ionized bulk into the material, which would change the properties of material.

Therefore, an optimized dosage is needed. The precise value of this parameter can't be obtained just from simulation. The testing of real material properties is

needed in practice to optimize the preparation condition. So we tested material performances with as many as possible samples with different growing conditions such as dosage, annealing temperature, etc in this chapter. To test samples with different implant energy and dosage, we have tried four sets of growing condition in this thesis:

Set	Implantion conditon
Oe13	500keV/$2.5\times10^{13}cm^{-2}$ + 800keV/$2.5\times10^{13}cm^{-2}$ +1200keV/$4\times10^{13}cm^{-2}$
Oe14	500keV/$6\times10^{13}cm^{-2}$ + 800keV/$6\times10^{13}cm^{-2}$ +1200keV/$1\times10^{14}cm^{-2}$
O2e14	500keV/$1.2\times10^{13}cm^{-2}$ + 800keV/$1.2\times10^{13}cm^{-2}$ +1200keV/$2\times10^{14}cm^{-2}$
Oe15	500keV/6×10^{14} cm^{-2} + 800keV/6×10^{14} cm^{-2} + 1200keV/1×10^{15} cm^{-2}

The detail operation of RBS machine will not be discussed here. In the part of "2.4 Material properties", some testing results are showed to help to optimize the material preparing condition.

2.3 Annealing process

After ion implantation, the implanted material has poor electrical characteristics, for example, severely degraded in mobility. Furthermore, only a fraction of the implanted ions are located on the substitutional sites and contribute to the carrier concentration.

To eliminate the detrimental effects of ion implantation, the material has to be annealed at an appropriate temperature for optimized time. By this procedure, the defect density would be reduced because of the annihilation of some of the vacancies. And the implanted dopant atoms in the interstitial sites could migrate to the lattice sites and become electrical active.

Conventional annealing uses a tube furnace which system which is widely used for thermal oxidation. This kind of annealing normally requires a long annealing time, and also will cause the dopant ions diffusion inside of the implanted material. If one wants to anneal those dopant ions and minimize the dopant redistribution, a

Rapid Temperature Annealing (RTA) method will be used.

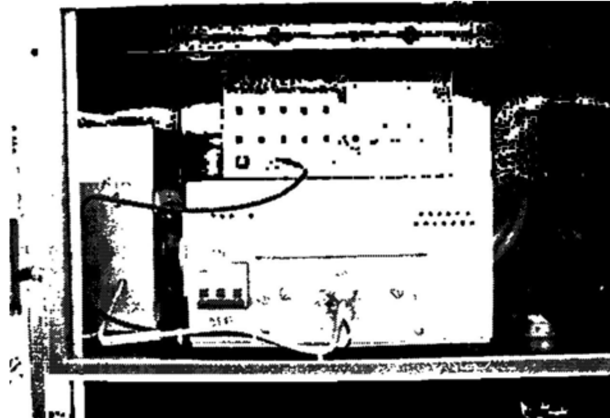

Figure2.4: Facility of rapid thermal annealing

In the RTA machine (Figure 2.4), the wafers on the quartz holder are heated by the optical radiation which passing through the quartz window from tungsten quartz lamps. The annealing temperature can be selected from 200℃ to more than 1000℃. In the chamber of RTA machine, the temperature rises rapidly, and reaches to a high temperature from room temperature within a few seconds.

To prevent some unwanted chemical reaction between wafer and the components in air under high temperature, some inert gases are blown into the chamber, such as N_2, Ar gas. For GaAs:O material annealing, a GaAs cap will also be covered onto the sample surface to minimize the escaping of As+ from the substrate into the air, under such kind of high annealing temperature. (The process detail is showed in Appendix A.)

For the temperature lower than 300℃, the effect of annealing process (especially RTA method) will not be obvious for GaAs materials (LTG or ion implanted). For temperature near 650℃, the carrier concentration will be greatly changed by the annealing process and the defects will come to disappearance. An even higher temperature will not change the material characteristics further.

So, here we only selected some annealing temperature in the range of 300℃-650℃. As the best temperature for dark resistance may not be the best one for the carrier lifetime, the best annealing temperature for materials is required to

consider for all the desired properties of material.

2.4 Material properties

Whether a material could be used for fabricating THz PC devices depends on its material properties like carrier lifetime, dark resistance, breakdown voltage, carrier mobility, and etc. As what we discuss in this thesis is the photoconductive devices, the light absorption character is also an important factor needs to be considered. From the material preparation method introduced above, one could prepare GaAs:O materials by various combination of implantation energy and implant dosage to fulfill the requirements for materials, and using suitable annealing technology to optimize the performances of material in some degree, after ion implantation.

Now, let's review at whether the GaAs:O materials grown by ion implantation method can meet those requirements on the material properties.

2.4.1 Infrared light (IR) Absorption

The defects created in the substrate by implantation will create additional mid-gap states within energy bandgap. They will act as trapping centers of excited carriers, such as EL2-like defects. How can these mid-gap defects affect the material properties like light absorption and carrier lifetime? A theory model should possibly give us some details. S.D. Benjamin[48] suggested a model to observe the behavior of these mid-gap trap states with a rate equation formalism in 1996.

Figure 2.5 shows the band diagram including the mid-gap states. Assume N_{band} is the population of carrier at the bottom of the conduction band and N_{trap} is the population of carriers in the trap centers. The N_{inner} is assumed as the population of carriers in the excited states within the conduction band. Photon whose energy ($\hbar\omega$) is slightly larger than E_g will excite electrons to the bottom of the conduction band from valance band. After some time, some of these carriers will recombine by decay back to the valance band from conduction band in a decay time τ_1, and the others will be trapped in the mid-gap states (N_{trap}) in a decay time τ_2. These carriers which

trapped by trapping centers in the mid-gap states can be optically excited to upper state in the conduction band. This kind of re-exciting process gives rise to an additional absorption mechanism in ion implanted GaAs or LTG GaAs, and can produce a substantially larger carrier concentration in the conduction band than those materials just have band-to-band absorption.

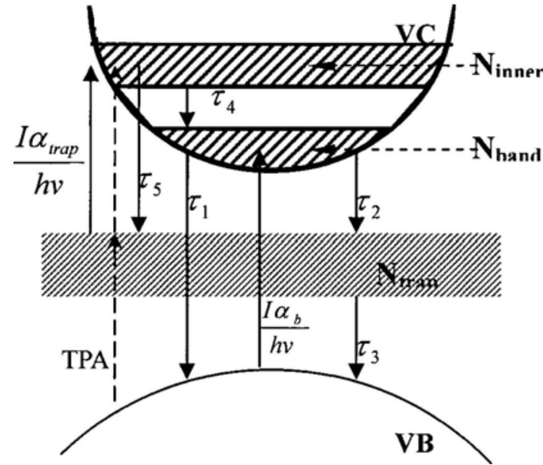

Figure2.5: Band diagram of ion implanted GaAs showing the key excitation and decay processes in the rate equation model.

The time dynamics of carriers in ion implanted GaAs is described by a set of rate equations like following:

$$\frac{dN_{band}}{dt} = \frac{I\alpha_b}{\hbar\omega} - \frac{N_{band}}{\tau_1} - \frac{N_{band}}{\tau_2} + \frac{N_{inner}}{\tau_4}, \tag{2.1}$$

where I is the intensity of incident light with photon energy $\hbar\omega$, α_b is the band-to-band absorption coefficient;

$$\frac{dN_{trap}}{dt} = -\frac{I\alpha_{trap}}{\hbar\omega} - \frac{N_{trap}}{\tau_3} + \frac{N_{band}}{\tau_2} + \frac{N_{inner}}{\tau_5}, \tag{2.2}$$

where α_{trap} is the absorption coefficient from the traps to the upper excited states (N_{inner}) in the conduction band. And

$$\frac{dN_{inner}}{dt} = \frac{I\alpha_{trap}}{\hbar\omega} - \frac{N_{inner}}{\tau_4} - \frac{N_{inner}}{\tau_5} + \frac{I^2\beta}{2\hbar\omega}, \tag{2.3}$$

Where β is the two-photon absorption coefficient. The decay times (τ) refer to the relaxation processes indicated in Figure 2.5.

From these equations, we can easily deduce the total absorption coefficient as:

$$\begin{aligned}\alpha &= \alpha_b + \alpha_{trap} + I\beta \\ &= \sigma_b N_{band(0)}(1 - \frac{N_{band}}{N_{band(0)}}) + \sigma_{trap} N_{trap(0)}(1 - \frac{N_{trap}}{N_{trap(0)}}) + I\beta\end{aligned}, \quad (2.4)$$

Where $N_{band(0)}$ and $N_{trap(0)}$ are the saturation carrier density near bandgap in conduction band and the density of defects which act as trapping center respectively. σ_b is the cross section for band-to-band transitions, and σ_{trap} is the cross section for absorption from the traps to the (N_{inner}) excited states in the conduction band.

From the equation, the total absorption coefficient is firstly contributed by band-to band absorption coefficient which having a maximum value equals to $N_{band(0)}$ ($N_{band(0)} \approx 1.9\times10^{18}/cm^3$ [49]). The second contribution factor to the total absorption coefficient comes from the trapping centers in which the trapped carriers could be re-excited to upper excited states in the conduction band. The contribution factor also has a maximum value which equals to the concentration of ion implantation induced defects. The last factor is also related to the mid-gap states, but its contribution is mainly caused by two photon absorption process.

Now, we can clearly know the effect of defects on the phonon absorption from the second and third terms of total absorption coefficient equation Eq. (2.4). More defects introduced into the material by ion implantation or low temperature grown will lead to the increasing of $N_{trap(0)}$, directly increasing the possibility of absorption caused by re-excitation. And the existing of mid-gap states also increases the chance of two photon absorption process under high pumping condition, β is found to be at level of 35 cm^2/GW [48] . Without trapping centers, there are no other mechanisms that would contribute to the photon absorption process except band-to-band absorption, for example in intrinsic semiconductor.

From the previous analysis, one can get some ideas. For example, by measuring

the changing of photon absorption with photon energy is lower than energy bandgap but higher than one half of the energy bandgap, one can easily get to know the relative account of concentration of defects from different samples of the same substrate by qualitative analysis.

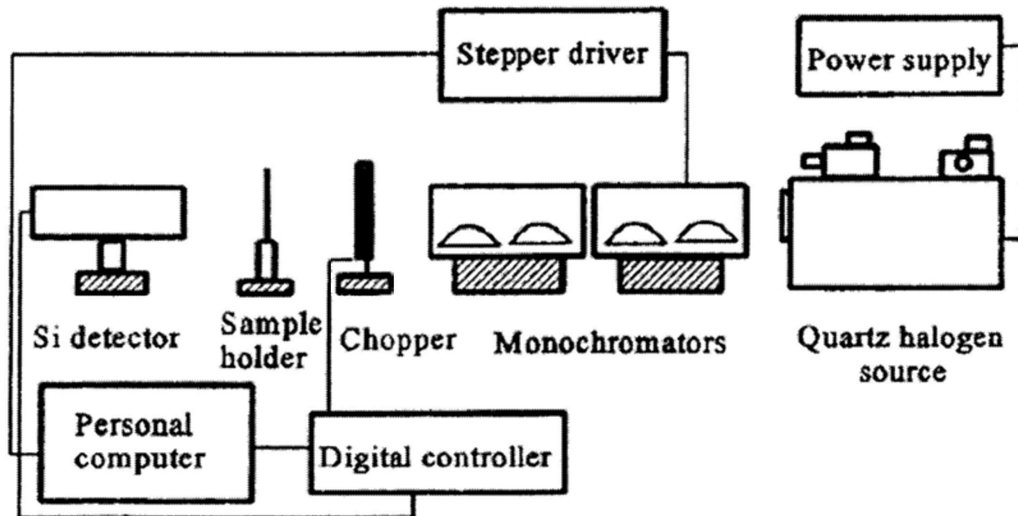

Figure2.6: System of IR transmission measurement

Using the IR transmission measurement system, the absorption at various wavelengths can be measured. Figure 2.6 shows the experimental setup, the quartz halogen lamp source is used to generate broadband lights (from UV to IR). A monochromator is used to select the wavelength of interest. By scanning the wavelength of light selected by monochromator, the absorption as a function of wavelength of pumping light will be obtained. In this thesis, the scanning range is from 740nm to 940nm.

Firstly, let's take a look on oxygen ion implanted GaAs materials with different ion dosage. Semi-insulator GaAs (100) wafers are cut into several $1\times0.5\ cm^2$ samples, some of them are marked as H1-H16. Among them, samples are material grown by multi-implantation method, whose implantation parameters (energy/dose) are like following:

No.	Set	Implantation condition
H1-H4	GaAs(100):Oe13	$500keV/2.5\times10^{13}cm^{-2}+800keV/2.5\times10^{13}cm^{-2}+1200keV/4\times10^{13}cm^{-2}$
H5-H8	GaAs(100):O2e14	$500keV/1.2\times10^{14}cm^{-2}+800keV/1.2\times10^{14}cm^{-2}+1200keV/2\times10^{14}cm^{-2}$

H9-H12	GaAs(100):Oe15	500keV/6×10^{14}cm^{-2} + 800keV/6×10^{14} cm^{-2}+ 1200keV/1×10^{15} cm^{-2}
H13-H16	GaAs(100)	un-implanted

(Note: the un-implanted samples sometimes are also called as undoped samples in some figures for convenient reading)

As mentioned before, the implanted materials should be annealed at certain temperature before being used for practical applications. Firstly, we annealed samples at 400℃ for 60 seconds (real annealing parameters is with a short warming time under 300℃ for 5s before that 400℃/60s) for sample H4, H8, H12 and H16. After annealing process, these samples are loaded into the IR transmission measurement system. The measured results are shown in Figure 2.7. From the figure, one can find the transmission of un-implanted GaAs sample which annealed at 400 ℃ is similar to the un-implanted GaAs sample without any annealing process (asgrown sample, cut from wafer directly). This means under this annealing temperature, the characteristics of substrate is almost unchanged by the annealing process. For those three other samples, the transmission intensities are different with the un-implanted samples in the range of 875nm to 940nm (whose wavelength is larger than that related to the bandgap energy of GaAs (1.42eV)). The main reason of this difference should come from the defects induced by the ion implantation process. After 400℃ annealing, the defects in these three O^+ implanted GaAs samples (H4, H8 and H12) still exist. From the equation of total absorption coefficient (Eq.(2.4)), one can find more defects existing in the material will lead to the higher absorption of incident lights, whose energy is just higher than half of bandgap energy . So, one can easily find the transmission intensities decrease step by step from un-implanted GaAs samples (asgrown sample and H16) to the low dosage implanted GaAs (H4-GaAs:Oe13), then to the middle dosage level sample (H8-GaAs:O2e14), finally to the high dosage level sample (H12-GaAs:Oe15).

These results directly show us the relative concentration of defects in these ion implanted samples. In another word, the high dosage implanted sample (H12) has more defects existing in the material than those lower dosage samples (H4 and H8)

after 400℃ annealing process. And the defects in those three implanted samples are not annealed out under such low annealing temperature, as they still have different absorption behavior compared with those two un-implanted samples.

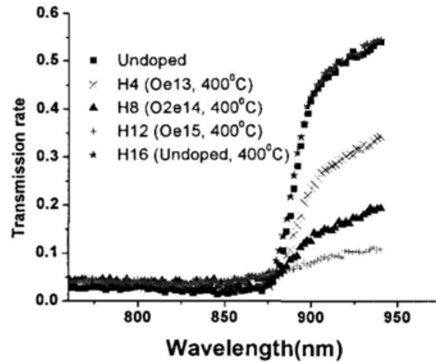

Figure2.7: IR Transmission of GaAs:O materials with different implant dosage after 400℃ annealing.

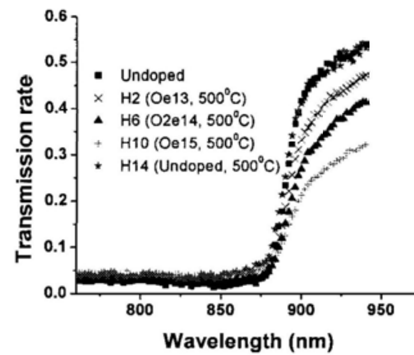

Figure2.8: IR Transmission of GaAs:O materials with different implant dosageafter 500℃ annealing.

Now, let's increase the annealing temperature to 500℃ to see what will happen. Figure 2.8 shows the measurement results. The same as the Figure 2.7, 400℃ annealing, the characteristics of materials do not have significant change under this annealing temperature. But the differences between the transmission intensities of ion implanted samples (H2-GaAs:Oe13, H6-GaAs:O2e14 and H14-GaAs:Oe15) and those un-implanted samples (asgrown one and H16) become less. That means more defects in these ion implanted samples are recovered by annealing process comparing with the 400℃ annealing temperature, but there still some defects exist in these samples because of the existence of the difference between them to the un-implanted samples.

A higher annealing temperature as 550℃ (300℃/5s + **550**℃/ 60s) has also been tested. Figure 2.9 shows the transmission spectrum of samples under 550 ℃. In this figure, we can find the transmission intensity of un-implanted GaAs material is changed a lot by high annealing process comparing to the sample without any annealing process (asgrown one). At the same annealing condition, the ion implanted samples also have significant change in their properties. Unlike Figure 2.7 and Figure 2.8, the transmission intensity of middle level implanted sample

(H5-GaAs:O2e14) is the smallest one among these three implanted samples(other two are H1-GaAs:Oe13 and H9-GaAs:Oe15). It seems that the defects in the sample H5 has more opportunity to exist compared with that in sample H9, under this high annealing temperature. The detail why the high level implanted sample having lower concentration of defects than middle level implantation is not clear yet. It needs other methods to have detailed study on this phenomenon.

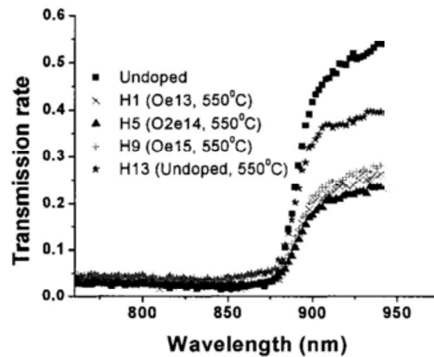

Figure2.9: IR Transmission of GaAs:O materials with different implant dosage after 550℃ annealing.

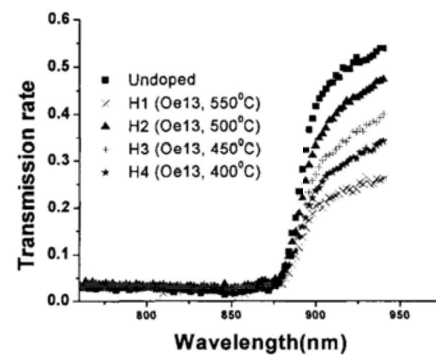

Figure2.10: IR Transmission of GaAs:Oe13 materials with different annealing temperatures.

One thing should be mentioned. The surfaces of 550℃ annealed samples are not as shining as those samples annealed under lower temperature. It looks like something (gray color) covering the surface. Two possible reasons will cause this kind of phenomenon. One is the preparation of thin oxide layer on the surface, maybe caused by the imperfect inert gas atmosphere (blowing speed of N_2 gas is not enough) during the annealing process. The other possible reason is the escaping of As^+ ions from the surface of GaAs samples. Although we have covered the samples with another GaAs sample to avoid the escaping of As^+, the possibility of escaping of As^+ still exists, because this method can only decrease but not prohibit the escaping. These cause the analysis of defect concentration to be more complex.

For our case, the information of related magnitude of defect concentration is adequate for the study. So we haven't obtained into deep study of the actions in materials during the higher temperature annealing process. But the conclusion about defects concentration looks acceptable, because the results come from another

measurement method also leads to this conclusion. The detail about that method will be discussed later (in chapter 2.4.2).

After comparing the concentration of defects from different level implantation after certain annealing temperature, let's take a look at the relationship of defect concentration to the annealing temperature.

Figure 2.10 shows the IR transmission results for GaAs:Oe13 samples with different annealing temperatures. From the figure, a clear increase of transmission intensity with the increasing temperature can be obtained, except the sample H1 (annealed under 550℃). This result tells us, the concentration of defects in these GaAs:Oe13 samples are decreased with the annealing temperature increasing. The main reason is the defects are annealed out (or to say recovered) during the annealing process. Some one maybe will question, why the higher annealing temperature will have more concentration of defects still existing? As showed before in Figure 2.9, in such level annealing temperature the characteristics of substrate (un-implanted sample) are changed much. This reminds us, the reference level is changed from the lower annealing temperature (400℃, 450℃ and 500℃) to the higher annealing temperature (550℃), and we cannot compare those data from different reference systems directly. In anther words, the analysis for the concentration of defects in the implanted material with higher annealing will be more complex, because it needs to consider the factor of the changing of substrate too. So, in this thesis, the detailed analysis for the sample with higher annealing temperature (550℃) will be lied over first.

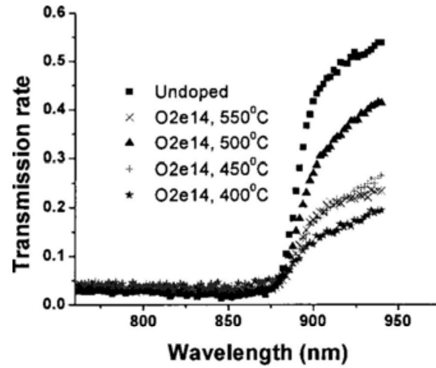

Figure2.11: IR Transmission of GaAs:O 2e14 materials with different annealing temperatures

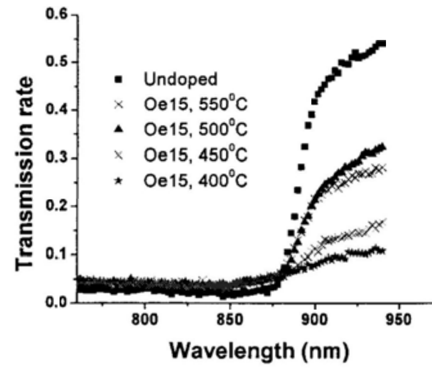

Figure 2.12: IR Transmission of GaAs:O e15 materials with different annealing temperatures

Again, we can also get the results for GaAs:O 2e14 samples and GaAs:Oe15 samples with different annealing temperature (The data of 550℃ are still plot in the Figure s just for reference). From Figure 2.11 and Figure 2.12, the transmission intensities increased from 400℃ to 500℃ under both dosage conditions. So, we can obtain the same conclusion that the concentration of defects decrease with the increasing of annealing temperature as GaAs:Oe13 samples.

At the same time we also tested some SI GaAs(110) substrates, the dosage are the same as SI GaAs(100) discussed above. In this thesis all the GaAs materials are semi-insulating, and the SI GaAs(110) material has originally higher resistivity than SI GaAs(100). It is too high to be characterized by the facility (Hall effect and resistivity measurement) what we have, which will be introduced later. To simplify the mark of samples in the following parts in this Chapter (only in this chapter), SI GaAs will be used to present SI GaAs(110) samples, if there is no additional mention.

Figure 2.13 shows the parts of data from SI GaAs(110) samples. The results are similar to those of GaAs(100) samples above. Higher dosage will lead to the lower IR transmission. Other performance related to the annealing should be also similar to those of GaAs(100) samples, here we will jump over these data and figures.

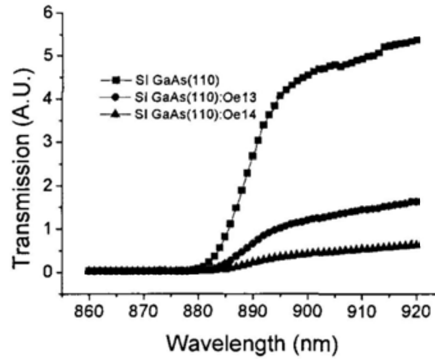

Figure2.13: IR Transmission of GaAs(110):O materials with different dosage.

From the discussion above, one can know the relationship between IR transmission performance (Or light absorption) and the ion implant dosage, and the change with different annealing temperature. One can also get some ideas like the following, that the change of transmission performance should be tightly related to the concentration of defects. As the defect concentration will also affect other characteristics of material like carrier lifetime, refractive index, etc., besides the light absorption. And carrier lifetime is one of the most importance parameters of material for fabricating high speed devices like THz photoconductor switches. So, using some convenient method to get a peek of the relative magnitude of defects concentration in certain materials, it will be a very meaningful approach for material study. The IR transmission method together with the theory of carrier dynamic of ion implanted GaAs just gives us such kind of an approach to take a peek of the defect concentration of ion implanted materials. From these experimental results showed above, we can easily find the proofs for the existence of defects in the ion implanted materials, and the fact that concentration of defects will decrease with the annealing temperature increasing.

From the analysis above, we can also get a deduction (or hypothesis) as following: the increasing of defects concentration will lead to the increase of the light absorption saturation level, which means more pumping light can potentially be absorbed to generate THz wave if all these absorbed power could transfer to THz

power.

2.4.2 Carrier concentration, Resistivity and Carrier mobility

For common users, a more common used direct measurement method for analysis defect concentration should be carrier concentration measurement, but it needs to fabricate some metal pattern on the material before testing. The carrier concentration in semiconductor may be different from the impurity (defect) concentration, because the ionized impurity density depends on the temperature and the impurity energy level. But the carrier concentration should be proportional to the defect (impurity) concentration in certain temperature and impurity type. So, one could also get some idea on defect concentration by measuring the carrier concentration in the semiconductors.

The common method used for carrier concentration measurement is Hall Effect. Hall Effect measurement is a method bases on the defection of charge carriers moving in a magnetic field. By measuring Hall voltage, one can get the carrier concentration ($p = \frac{1}{qR_H} = \frac{IB_zW}{qV_HA}$) and the type of free carriers (when $p>0$ it is p-type, and $p<0$ it is n-type). An extensive review of Hall Effect has been given by D.K.Schroder [50]. Figure 2.14 shows the carrier concentrations of GaAs:O samples with different annealing temperatures measured by Hall Effect method. The sign of the measured carrier concentrations of these samples are all negative, which means the samples (H1-H16) are all n-type. The un-implanted GaAs (asgrown GaAs) samples have a low carrier concentration. By implantation process, the free carrier concentration of the ion implanted GaAs samples (H1-H4: GaAs:Oe13, H5-H8: GaAs:O2e14 and H9-H12: GaAs:Oe15) increase. From low temperature annealing (400℃) which most defects are kept well in the materials, one can easily find the relationship between material carrier concentration and ion implant dosage. The high level implantation (GaAs:Oe15) has highest carrier concentration level among them, then is the middle level implantation

(GaAs:O2e14). By increasing the annealing temperature, we can get lower carrier concentration from all these three levels ion implanted materials, until at the end they come back to the carrier concentration level of asgrown sample, where the defects are closely to be annealed out.

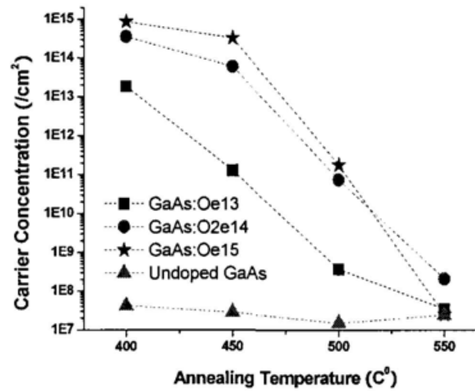

Figure2.14: Carrier concentration Vs Annealing Temperature for O^+ implanted GaAs.

So, from the trends obtained by these results, one can also get the same conclusions as those from IR transmission method. Ion implantation can increase the defect concentration in material and the concentration of defects is proportional to the ion dosage level. And the annealing process can lead to the recovering of defects.

Now, come back to the question we raised above in the chapter 2.4.1, why the high level implanted sample will have lower concentration of defects than middle and low level implantation by 550℃ annealing process? Is that method really suitable for defect concentration analysis? From carrier concentration measurement, one also can find the GaAs:Oe15 sample has the lowest carrier concentration among these three type implanted GaAs samples, under 550℃ annealing temperature. This kind of results shows the magnitude sequences of defect concentration for these three kinds of samples are the same from this method (carrier concentration measurement by Hall Effect method) as those from IR transmission method discussed before.

So, we can say, these two approaches are both suitable for studying the relative

magnitude of defect concentration in ion implanted materials. And they can prove each other perfectly.

For THz PC switches, the dark resistance is one of the most important parameters which determining the performances of devices. Higher dark resistance means the higher signal to noise (SNR) can be obtained from the devices fabricated on such materials. The most common method for resistivity (ρ) measurement is the four-point-probe method [42]. To get material resistivity more close to the condition of material for fabricating THz PC switches, we also make these four separated metal contact pads by depositing a Ti/Au thin film layer on the oxygen ion implanted GaAs. This process and fabrication conditions are all the same as the fabricating of THz PC devices in this thesis. The detail of fabrication will be introduced in Chapter 3.

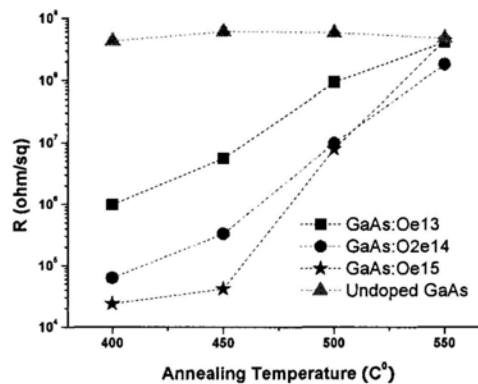

Figure2.15: Resistivity of GaAs:O materials Vs Annealing Temperature

After contact pad fabrication, a low temperature (300℃) annealing process can be selected to achieve good alloyed contact for metal to substrate. Figure 2.15 shows the results of resistance measurement. The un-implanted GaAs (asgrown one) samples have a high dark resistivity. By implantation process, the resistivities of the ion implanted GaAs samples decrease. When the annealing temperature increases, the resistivities of GaAs:O materials from all these three dosage levels increase too.

Under higher annealing temperature around 550℃, the material resistivity comes back to the high resistivity level like asgrown sample. So, if just considering the resistivity factor for the THz PC switches, the annealing temperature range from 400℃ to around 550℃ is acceptable for low level ion implanted GaAs (GaAs:Oe13), and 475℃ to 550℃ range is acceptable for middle level and higher level implanted GaAs materials (GaAs:O2e14 and GaAs:Oe15).

Besides resistivity, another important parameter for THz PC devices is carrier mobility (μ), which directly impacts the current under certain electrical bias. As we know, the output power of THz PC devices is proportional to the photocurrent (exactly, it is derivative of photocurrent) generated by incident light. Under the same optical pumping power and electrical bias voltage, the materials which have higher carrier mobility would generate larger photocurrent ($I_c = en\mu\, V_b$, where n is carrier density, e is elementary charge, V_b is the electrical bias.), leading to a higher output power of THz waves.

The carrier mobility can be calculated from carrier concentration and resistivity by equation $\mu = \dfrac{1}{en\rho}$. Figure 2.16 shows the results of carrier mobility. Although the carrier mobility is calculated from them, the fact should be reminded is that the carrier mobility determining the resisitivity with carrier concentration in physics, but not opposite way. So from the point view of material alternation, we only can change the carrier concentration (relates to the impurity concentration) and the carrier mobility of material which will lead to the change of resistivity.

So, by analyzing Figure 2.14, Figure 2.15, and Figure 2.16 together, when O^+ ion are implanted into the GaAs materials, the carrier concentration (defect concentration) increases and the carrier mobility decreases from their original level of asgrown GaAs. Higher implant dosage will create more carrier concentration as mentioned before. But the change of carrier mobility with different dosage looks

more complex.

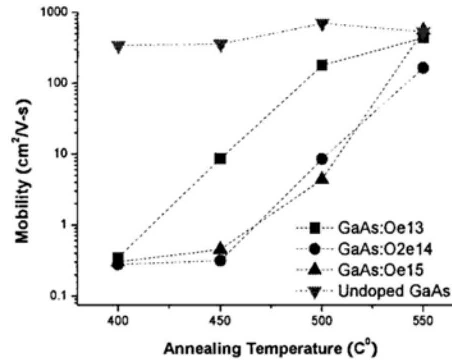

Figure2.16: Carrier mobility of GaAs:O materials Vs Annealing temperatures

For the samples with the same implant dosage level, when the annealing temperature increases, the carrier mobility will rise again. This means the damage on the crystal lattice of material is recovered step by step which leads to the recovering of carrier mobility. But carrier mobility is not changed as carrier concentration in some annealing temperature range (lower than 450℃). It isn't always proportional to the carrier concentration under such annealing temperature. This phenomenon may be caused by other physical reason which is not only the defect concentration, but also the form of the existing defects and the relative position of defects and atoms.

Under higher annealing temperature around 550℃, most effects on carrier concentration and carrier mobility by ion implantation process almost disappeared, which leads to the resistivity to recover in physics. As mentioned before, the carrier mobility and resistivity are two very important parameters for THz PC devices. A higher carrier mobility and resistivity together is desired by users, like LTG GaAs. But the resistivity and carrier mobility is in inverse proportion, an increase of carrier mobility will cause the dark resistivity of material to decrease. Then, the only choice to keep them high at the same time is to decrease the free carrier concentration.

As discussed above, the carrier concentration is proportional to the defect

concentration which generated by ion implantation or low temperature grown. An increase in impurity (defects) concentration will cause the free carrier concentration to increase. But, as we know, the free carrier concentration is also determined by the temperature and the impurity energy level at same time, besides the impurity concentration. As we still require defects to decrease the carrier lifetime of material (the reason we will discuss later), so the best choice is to find some type of ion which can generate defects but give little contribution to the free carrier concentration. What kind of ion can be?

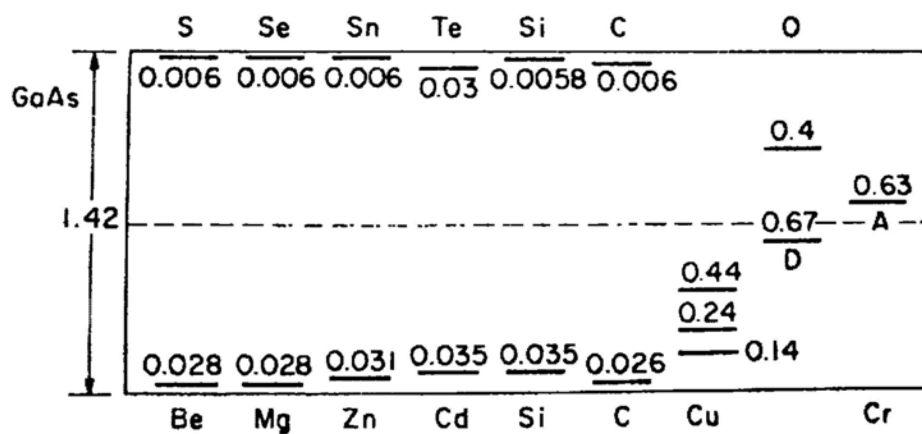

Figure2.17: The ionization energies for various impurities in GaAs. [42]

Physically, the ion whose energy level generated in such material (for example, GaAs substrate) is close to the Fermi level can be used. Figure 2.17[42] shows the measured ionization energies for various impurities in GaAs material. From it, we can easily find oxygen ion is one of good choices. This is one of main reasons why we investigate oxygen implanted GaAs materials in this thesis.

2.4.3 Carrier lifetime

The most important parameter is the carrier lifetime of material, which determines if the material can be used for generating THz wave by photoconductive approach. Only those materials which have short carrier lifetime, (not longer than 10 ps for responding to 0.1 THz, the lowest value for THz gap), could have better performance on high frequency THz generation. Normally, carrier lifetime shorter

than 1 ps is desired. Note: It doesn't mean the material with longer carrier lifetime couldn't be used for THz wave generation by photoconductive method. For example, normal Semi-insulating GaAs, which has a carrier lifetime around several hundred picoseconds, can also be used for such purpose. But its performance would be not as good as those with shorter carrier lifetimes, on high frequency THz generation [51].

As this carrier lifetime level is difficult to be studied by electrical method, in practice, the common approach is optical method, like Time-domain photoreflectance method (pump-probe detection). In simple words, the Time-domain photoreflectance method is a method, which measures the change of reflection (or transmission) rate of light against time (the time delay from probe light to the pump light) to quantitative the carrier lifetime of material. The reflection (or transmission) rate can be changed under (relative high power) light injection, mainly through band-filling effect, bandgap shrinkage (renormalization) effect and free-carrier absorption effect.

(1) Band-filling Effect [52, 53]

To electron, the density of energy state in conduction band is low, so the bottom of conduction band can be filled by only a few free electrons, which forcing the energy required for the electron excited to the conductive band from valance band should be larger than the energy gap. And, it also leads to the decreasing of the absorption efficiency of light which energy is larger than energy gap.

As the band filling effect is caused by free-electrons, some approaches like "injection" or "doping" ,which can bring additional free electrons into the material, can cause this kind of effect. The refractive index of material changed with the carrier density can be expressed by the following equation:

$$\Delta n(\Delta N,\Delta P,E)=\frac{2c\hbar}{\exp(2)}\int_0^\infty \frac{\Delta\alpha(\Delta N,\Delta P,E')}{E'^2-E^2}dE', \tag{2.5}$$

Where ΔN and ΔP are the concentrations change of free electrons and holes, respectively, E ($E=\hbar\omega$) is the photon energy. $\Delta\alpha$ is the change of absorption

efficiency of material, which is a function of the additional concentration change of carriers (ΔN, ΔP) and the certain light energy (wavelength). And e is the electron charge.

(2) Bandgap shrinkage (renormalization) effect [52]

The injected electrons will also occupy states at the bottom of the conduction band. If the concentration of electrons is large enough, the electron wave functions will overlap and forms a gas of interacting particles. The electrons will repel others by Coulomb forces. In addition, for statistical reason, electrons with the same spin will avoid in the same state. The net result of them is a screening of electrons and a decrease in their energy, lowering the energy of the conduction band edge. For holes, the similar correlation effect exists, which increases the energy of the valence band edge. The sum of these effects of electrons and holes leads to the band-gap shrinkage. The model of this effect is like:

$$\Delta E_g(\chi) = \frac{\kappa}{\varepsilon_s}\left(1 - \frac{\chi}{\chi_{cr}}\right)^{1/3} \qquad \chi \geq \chi_{cr}$$

$$\Delta E_g(\chi) = 0 \qquad \chi < \chi_{cr}, \tag{2.6}$$

where χ is the concentration of free electron or holes, and χ_{cr} is the critical concentration of free carriers. ε_s and κ are the relative static dielectric constant of the material and a fitting parameter, respectively.

The change of bandgap will lead to the absorption curve to a red shift:

$$\Delta\alpha(\chi, E) = \frac{C}{E}\sqrt{E - E_g - \Delta E_g(\chi)} - \frac{C}{E}\sqrt{E - E_g}, \tag{2.7}$$

where E_g is the bandgap energy. And C is a fitting constant. Then, by the Kramers-Kronig integrals[54], one can get the relationship between bandgap shrinkage and the change of reflective index. To mention, the bandgap shrinkage effect is determined by free-carrier density, and it is nearly independent of impurity concentration[55].

(3) Free-carrier absorption

The band filling and band-gap shrinkage effects are caused by interband absorption,

in addition, there exists another absorption mechanism like intraband absorption. A free carrier can absorb a photon and go up to a higher energy state within an energy band. In the Drude model, this kind of intraband free-carrier absorption is also known as the plasma effect. The change of reflective index by this kind of absorption is directly proportional to the concentration of electrons and holes and the square of the wavelength. The theoretical model is given by[56]

$$\Delta n = -(\frac{\exp(2)\lambda^2}{8\pi^2 c^2 \varepsilon_0 n})(\frac{\Delta N}{m_e} + \frac{\Delta P}{m_h}). \quad (2.8)$$

Where c and ε_0 are light speed and the permittivity of free space. m_e and m_h are effective electron mass and hole mass. λ is the wavelength of injection light.

Note: n in the equations (Eq.(2.6)-Eq.(2.8)) of these three effects means the reflective index of material. It is not carrier density in the equations in other parts of this thesis.

These three effects are all related to the carrier concentration. When the pump light injects into the material (sample), these three effects will be created and cause the change of the reflective index of material. After turning off the pump light, these effects will disappear within a time range, which relates to the lifetime of these additional carriers generated by pump light in material. So by measuring the change of reflective index of certain sample against the time (pump-probe technology), one can finally get the carrier lifetime in such kind of material.

The common Time-domain photoreflectance system (pump-probe detection system) is like Figure 2.18 shows. A Mode-locked Ti: sapphire Laser is used as the laser source. Its pulse width and repetition rate are about 100fs and 80 MHz respectively, and the center wavelength can be adjusted from 750 nm to 850 nm as required.

The laser beam will be divided into two beams (4:1) after the first beam splitter (BS1). One is the high power pump beam, and the other is the low power probe beam. These two beams are attenuated by adjustable-filters separately, and around

several ten times power difference between them is adjusted to reducing the effect on the sample caused by the probe beam itself.

The light path difference can be controlled by a delay system. Its minimum difference depends on the precision of stepper motor. In this experimental setup the precision can reach 0.5μm, converting to the delay time is 3.3 fs. To make sure the samples were excited only by the pure horizontal polarization light, a polarization spectroscope is used to filter the vertical polarization light of pump beam. At last, the pump beam is focused onto the samples with 500μm spot diameter by a convex lens (focal length 10cm).

The Probe beam will go through a half-wave plate. The polarization direction of probe was changed to vertical from its original horizontal. So, the probe light is perpendicular to the pump light. To avoid the pump light going into the photodetector, a polarization beam splitter is placed before the photodetector to filter the horizontal light.

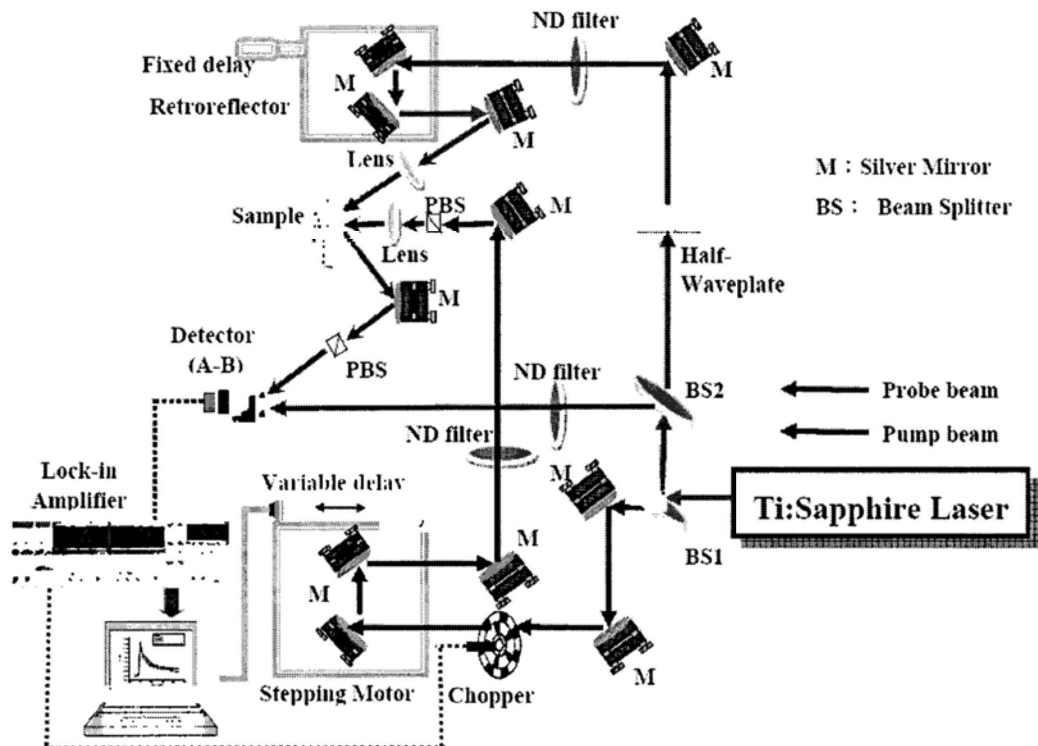

Figure 2.18:Time-domain photoreflectance system (Pump-probe system) for carrier lifetime measurement. (With permission from Prof.Chao-Kuei Lee of National Sun Yat-Sen University (NSYSU)).

In the light-detection section, there is another time-delay system. The main purpose is to finely vary the optical path difference, so the stepper motor on the road of pump beam can have the longest load path to study the change of transmission ratio and refractive index in time scale.

To achieve better SNR (Signal to Noise Ratio), the diameter of probe (200μm) is set to be smaller than that of pump light, and the probe light is covered by pump light completely. So, all the change of reflection rate detected by probe light can be looked as caused by the pump light.

In the balanced-photon detector, a reference probe beam is loaded which split from the probe light at very beginning. With the help of this reference light, the background noise can be diminished in some degree and leads to the increasing of SNR. A lock-in detection technology is also used to increase the signal-to-noise ratio. The chopping frequency is set at 1.6kHz in such experiment.

With this kind of pump-probe measurement system, we can test the carrier lifetime of our oxygen ion implanted GaAs materials. As introduced above, the SI GaAs(110) substrate materials have higher dark resistance than GaAs(100) substrate material, here we will test SI GaAs(110) based GaAs:O materials at first. Six GaAs(110):Oe13 samples are tested. Five of them are annealed by RTA process under 350℃, 400℃, 450℃, 550℃, 600℃,respectively. And the last one is an un-annealed sample (as-grown one) to help getting a reference level, then we can find the effect of anneal process (temperature) on the carrier lifetime of material.

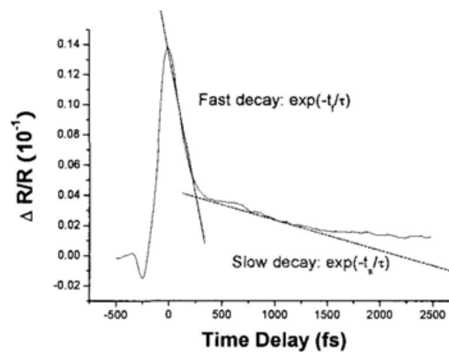

Figure2.19: Mechanism of photocarrier decay.

Figure 2.19 shows one of Carrier lifetime data measured by the pump-probe method. The reflection rate is fast decayed in the first few hundreds picoseconds, and then comes to a slow decay range with a large constant around 1 picosecond. This shows that there should be at least two decay mechanisms of carrier concentration in the material. I.S.Gregory [57] suggested a two-trap model to describe this kind of phenomenon in LTG GaAs materials. In that theory model, the point defects and the precipitates are the main mechanism for carrier trapping or recombination. For point defects, it will be eliminated with increase of annealing temperature. As the concentration of defects is related to the carriers trapping time (SRH model[5, 58]), the decreasing in defects concentration will leads to the carrier trapping time to increase. The trapping time caused by point defects can be expressed by:

$$\tau_{def} = \frac{1}{\sigma_c \upsilon_{th} (N_{def} - n_{def})}. \tag{2.9}$$

Where σ_c and υ_{th} are the capture cross section of each point defect and the thermal velocity of the electrons, respectively. N_{def} is the point defect trap density, and n_{def} is the occupation of the point defects states.

The more unoccupied trap centers left, the smaller trapping time τ_{def} will be found.

Unlike point defects, the precipitate does not only affect the carrier trapping time by its concentration, but also its capture cross section which relates to its diameter. The expression for precipitates on carrier lifetime is similar to Eq.(2.9):

$$\tau_{pre} = \frac{1}{\sigma_{pre} \upsilon_{th} N_{pre}}, \tag{2.10}$$

$$\sigma_{pre} = \pi (\frac{d_{pre} - d_{dep}}{2})^2. \tag{2.11}$$

Where N_{pre} is the number density of precipitates. d_{pre} is the precipitates cross section. d_{dep} is the extent of the depletion region. The thermal velocity at room temperature is on the level 3.8×10^{15} m/s[57].

The density of precipitate will increase with annealing temperature at first, and after reach to its maximum it will come down again like point defects eliminated under high temperature annealing process. The spacing of precipitate, which relates to the effective precipitates cross section, will decrease at first and then increase later with the annealing temperature from low level to high level. These two trends lead to the trapping time caused by precipitate unlike point defects. From Eq.(2.10)-Eq.(2.11), one can find the trapping time τ_{pre} will decrease at first and increase at higher annealing temperature.

As the effective carrier lifetime of material is the integrate contribution of these two main trapping times (τ_{def} and τ_{pre}), one can expect to get the lowest carrier lifetime at the best match point (temperature) of the curves of these two trapping times.

By measuring those six GaAs(110):Oe13 samples, we can get several figures like Figure 2.19. Taking out the fast decay time constant (τ_f) and the slow decay time constant (τ_s) in each figure, we can get the curves of them with the different annealing temperatures (see Figure 2.20).

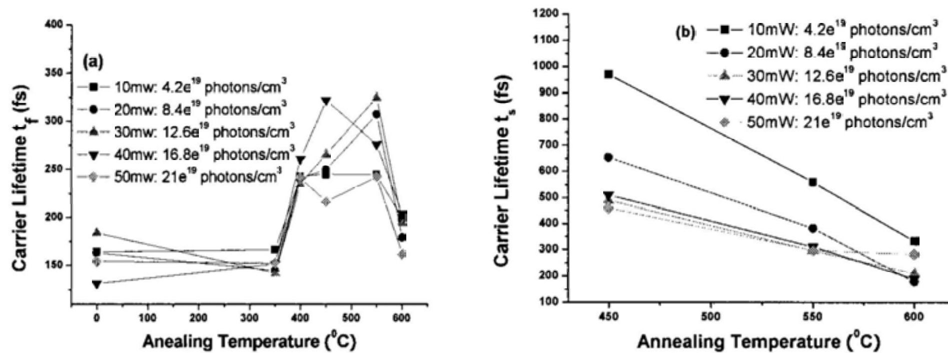

Figure2.20: The carrier lifetime of GaAs(110):Oe[13] materials with different annealing temperatures. (a) the fast decay time constant, (b) the slow decay time constant.

When the annealing temperature increases, the slow decay time constant (τ_s) decreases. It looks more like the behavior of precipitates in their low annealing temperature range. And the fast decay time constant (τ_f) is almost keeping little change in his constant in the range of (150fs-350fs), this looks more like the

behavior of point defects before they were annealed out. So we can look the fast decay time constant τ_f is mainly related to τ_{def}, and the slow decay time constant (τ_s) is mainly related to the τ_{pre}, in Eq.(2.9) and Eq.(2.10).

From Figure 2.20, one can expect the lowest carrier lifetime of GaAs(110):Oe13 should be in the range of 600℃-650℃, comparing with the curve in the Figure (FIG.5) of the reference paper[57].

The different match point (temperature) between our data and that paper, one should consider to take into account the effect of the deferent type of ion in the material. In that paper, As+ is the main source of defects during the Low temperature growing process, but in our case, the oxygen ion is the additional ion which we implanted into the GaAs substrates.

By using the Time-domain photoreflectance method, we can get two conclusions:

1).The fast decay time is in the range of 0.15-0.35 ps when the annealing temperature was set in the range of 350℃-650℃, and the slow decay time is in the range from 0.15 ps to several ps. The effective carrier lifetime of this kind of GaAs(110):Oe13 is shorter than 1 ps, and its main range should be 0.15-0.4 ps when the annealing temperature is in the range of 500 ℃-650 ℃.

2).The shortest effective carrier lifetime maybe could be achieved near 650 ℃.

Recalling the memory for the resisitivity and carrier mobility of materials under different temperature annealing, we found the best condition for both resistivity and carrier lifetime should be in the range of 500℃-600℃. The precise value in the range should be different for the different ion dosage level.

2.5 Summary

For THz generation through photoconductive method, at first, the material should have ultrafast carrier lifetime (shorter than 1 ps) to respond to the fs laser pumping and generate broadband THz wave (supposing the generation is under pulsed mode). Second, to achieve a better performance on THz generation, the resistivity of

material should be as high as possible to enhance the signal to noise ratio. A high resistivity is also inherently related to the possible high breakdown field of material, which would allow the higher output power of THz wave to generate from the devices on such material. Other parameters like carrier mobility and light absorption are also the important factors one needs to consider during the material design and preparation process.

Ion implantation method allows us to tailor the properties of materials as designed for fulfill those requirements discussed above. So, in this work, we tried this kind of material preparation method to introduce O+ ion into the SI GaAs substrate, for searching a possible substitution material of LTG GaAs.

Before implantation process, a simulation work has been done with TRIM program. From simulation results, three different implant energies (500 keV, 800 keV and 1200 keV) are selected for the multi-implantation process, considering those important factors like the absorption depth of 800nm light in GaAs materials and the uniform distribution of ion defects creased in the material by implantation. For selecting the best preparation condition of GaAs:O, several different implant dosages are tried in this work, for example, Oe13 and Oe14 (the maximum level for certain multi-implantation process).

After a post annealing process, the carrier concentrations of materials are tested at first. By the method of Hall Effect method and the IR transmission method, the inverse proportional relationship of the carrier concentration with the annealing temperature, and the proportional relationship of carrier concentration with ion dosage are both exhibited before us. Combining with the rate equations of ion implanted materials, IR transmission method could come to be a possible simple method for quantitative analysis of carrier concentration. (With such kind of method, the material sample can be used again in other situation after the testing, unlike Hall Effect method which the metal pattern on material limits recycle use of such sample.)

From the testing results of resistivity and carrier mobility, their values for ion

implanted samples come back to the level of asgrown one under high annealing temperature (higher than 550℃). This suggests that the defects in the GaAs:O materials are going to be annealed out under high annealing temperature. For keeping a relative high resistivity for THz generation usage, an annealing temperature higher 450 ℃ is desired for those three implant dosage level which tested in this work, (Oe13, O2e14 and Oe15).

At last part of this chapter, we tested the carrier lifetime of GaAs:O under different annealing temperatures, the carrier lifetimes are in the range of 0.15-0.35 ps (τ_f). The trends from the measurement results suggests the shortest carrier lifetime of GaAs:Oe13 materials should be under 650℃annealing condition.

As the preparation condition (especially the annealing temperature) of GaAs:O materials is a compromise between all those important parameters discussed above, from the testing of material properties, we found the best annealing temperature should be in the range **500℃-600℃** for the dosage level less than 10^{15} cm^2.

Chapter 3: Device Fabrication

3.1 Introduction

After getting suitable materials for such purpose, the following step comes to the device fabrication. This chapter will show 4 important processes for the device fabrication.

Firstly, a suitable antenna structure should be selected for special requirement. For example, to get narrow band with power enhancement in certain frequency, a dipole antenna[59] is a good choice. But for broad band THz generation, a spiral antenna[60] or bow-tie antenna[61] will be the first choice. For CW terahertz generation, we also need to consider the Bias field utilization, then adding some fingers structure in feed point of such antenna[31].

Second process is photolithography. Photolithography process is a very common process in semiconductor industry. Almost every modern electrical device which fabricated from semiconductor material has such kind of fabrication process before it works. By the help of photolithography process, the antenna structure can be transferred onto substrate materials easily in the form of photoresist pattern.

In this work, the following step is metal deposition. We use E-beam evaporator method to deposit Ti (Titanium) and Au (Gold) metals onto the substrate. As the substrate is patterned with photoresist already, only those substrate areas which uncovered by photoresist will have been metal deposited directly and form the device structure. The other areas will be no metal on them after lift-off step, because those metals over them are insulated by the photoresist layer and will be removed with the photoresist during the lift-off step.

The last process for device fabrication in this work is device package and wire-bonding. For easy handling, we have done some simple package work to hold devices onto the holder before testing. And then, a wire-bonding machine is used to create (gold) wire connection between contact pad of device and the metal contact

pad on the holder.

After those four important processes, a THz PC device is born. A high quality controlled fabrication process is the second important factor for PC devices to achieve good performances on THz generation. The first important factor, as we discussed in Chapter 2, is the material on which the devices fabricated.

3.2 Antenna structure.

In this work, we are more interested in the frequency around 0.3 THz and its possible highest output power of THz wave from PC devices. So we selected dipole antenna structure (a common used simple structure) for this study, for its good resonance performance, which can enhance the certain frequency component of one's interest.

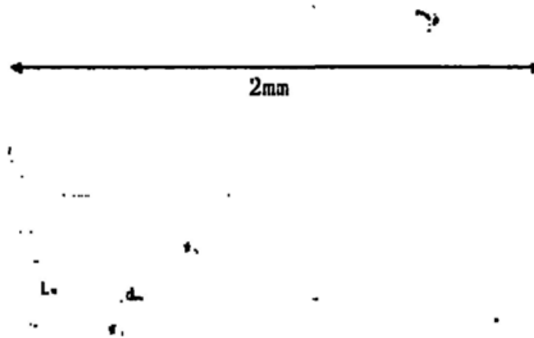

Figure3.1: Dipole antenna structure. (Insert window is the photogap area of device.)

For a dipole antenna structure like Figure 3.1, the resonance frequency can be approximated as [62]:

$$f_r = \frac{c}{\lambda_r} = \frac{c}{2L_{ae}n_{ref_index}} = \frac{c}{2L_{ae}\varepsilon_e^{1/2}} . \tag{3.1}$$

Where f_r is the resonance frequency of a dipole antenna, λ_r is the resonance wavelength, L_{ae} is the effective length of dipole antenna, ε_e is the effective

dielectric constant defined by $\varepsilon_e = (1+\varepsilon_d)/2$ [51]. And ε_d is the dielectric constant of the substrate material, it is about 13.08 for GaAs in THz frequencies range.[63]

$$L_{ae} = [(L_s + 2W_s)^2 + W_a{}^2]^{1/2}, \quad [51] \qquad (3.2)$$

L_s is the separation of two strip lines, W_s is the width of stripline. W_a is the width of antenna (electrode).

In this work, we selected the following parameters for our dipole antennas (Table 3.1), to test the THz generation performances of GaAs:O material. Their calculated resonance frequencies are 0.255 THz, 0.461 THz, 0.761 THz and 1.125 THz, respectively. One thing should be mentioned, the real resonance frequency of such kind of device is normally smaller than the value of calculated one.

Type of dipole	L_s (μ m)	W_s (μ m)	W_a (μ m)	d_{gap}(μ m)	L_{ae} (μ m)	f_r (THz)
T_D1	170	25	25	20	*221.42*	*0.25533*
T_D2	70	25	25	20	*122.58*	*0.46121*
T_D3	20	25	25	12	*74.330*	*0.76057*
T_D4	30	10	5	5	*50.249*	*1.1251*

Table 3.1: Parameters of dipole antennas and their calculated resonance frequencies.

To transform the antenna structure onto the GaAs:O substrate, a photomask is required for photolithography process. Considering our current device fabrication condition, we chose the laser printing method (minimum linewidth: 1μm) to fabricate this photomask. For this kind of photomask, the Chromium metal is used as the cover on normal soda lime glass.

3.3 Photolithography (process and parameters)

Photolithography is a fundamental process in Semiconductor Industry and related research area[45, 64]. It is an optical process of transferring patterns from a mask

onto a thin layer of photosensitive material (called photoresist) which covering the surface of a semiconductor wafer (like Silicon, GaAs, etc.). Then, with the formed patterns on photoresist, user can do etching or metal evaporation (or deposition) process to fabricated devices on the substrate as they designed.

The most common photolithography technique is contact printing. When the alignment is achieved, the mask bearing opaque-and-transparent patterns is pressed into hard contact with the photoresist coated wafer, which is then exposed through the mask with a flood beam of ultraviolet light. The minimum feature size that can be formed using photolithography is ultimately limited by the wavelength of the exposing light. After that, the layer is developed with developer to form the pattern in accordance with the mask pattern.

The brief processes of photolithography are showed in Figure 3.2.

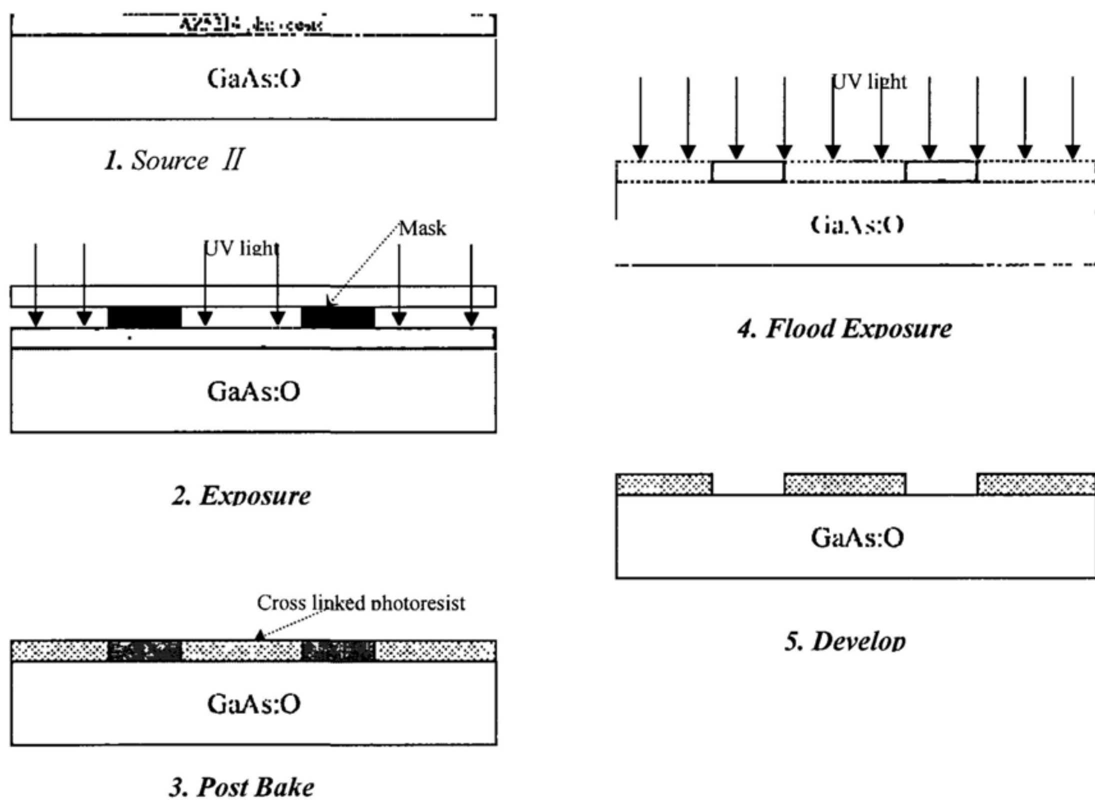

Figure3.2: Process of photolithography

To get good quality of pattern transferring, photolithography process should be done very carefully, including the preparing works.

So, in this work, the photolithography processes include: A.)Surface Preparation; B.)Photoresist Coating; C.)Pre-Bake(Soft Bake); D.)Alignment and Exposure; E.)Post-Bake(Hard Bake, to reverse photoresist polarity.); F.)Flood Exposure (post exposure, to confirm patterns); G.)Develop.

3.3.1 Wafer Cleaning

Photolithography is a plane technique and the minimum linewidth of device pattern is normally in the μm level. Even a small dust (or contaminant) on substrate (wafer) will cause the photoresist layer distortion or poor adhesion between photoresist and wafer, which will bring failure into the pattern structure during the photolithography process. So, a good surface preparing for substrate is the first important step for the following photolithography processes.

Several typical contaminants (as following shows) must be removed before photoresist coating (supposing the surface of wafer is already polished to be smooth):

5.1 Dust from scribing or cleaving.

5.2 Atmospheric dust (Need a good clean room practice, <100 particles/m^3 level)

5.3 Photoresist residue from previous photolithography (could be minimized by performing oxygen plasma ashing).

5.4 Bacteria (could be minimized by good DI water system).

5.5 Films from other sources. For example: solvent residue, H_2O residue, photoresist or developer residue.

In a standard clean room working condition, user only need to consider removing type 1,3,4 and parts of type 5 by (DI) wafer cleaning process, and removing H_2O residue by blowing with N_2 gas and hot baking.

A standard wafer cleaning steps are like following:

i) *Acetone* 3-5min (with ultrasonic agitation)

ii) *DI water* 3-5min (with ultrasonic agitation)

iii) *IPA (isopropanol)* 3-5min (with ultrasonic agitation)

iv) *DI water* 3-5min (with ultrasonic agitation)

v) *Blowing with N_2 gas*

vi) *Drying by Heater* (oven or hot-plate)

Note: Acetone is flammable liquid.

3.3.2 Photoresist Spin Coating

After cleaning and drying, wafer (sample) is moved to spinner to coat a thin photoresist layer.

Wafer is held on a spinner chuck by vacuum pump, to avoid the wafer flying off during the high speed spinning. Several drops of Photoresist (AZ5214, an amphibious photoresist used in this work) liquid are deposited onto the center of the wafer (or substrate).

Normally, spinner is working in 3000-6000rpm range for 15-30 seconds to get uniform thickness photoresist layer. The final thickness of photoresist after spin coating is primarily related to resist viscosity, and secondarily to the spinner rotational speed. $d_{thickness} = \frac{k_{spin} * per_{solids}^{2}}{\omega_{spin}^{1/2}}$. Where k_{spin} is spinner constant (typically 80-100), per_{solids} is photoresist solids content in percent, and the ω_{spin} parameter is related to spinner rotational speed (equal to rpm/1000).

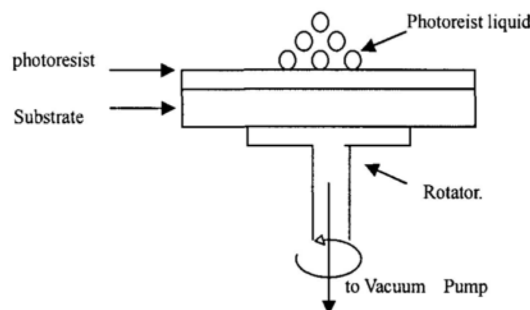

Figure3.3: Photoresist Spin Coating

For AZ5214 photoresist used in this work, we select the parameters of spin coating process like 3000rpm for 30seconds, to obtain a photoresist layer (around 2μm thick) on GaAs:O substrates. The sketch map of photoresist spin coating is

showed in **Figure 3.3**.

Note: To get better performance, during the coating process, one should add a slower rotating step before high speed rotating. The final parameters of spin coating are like this: **1200rpm for 9s and 3000 rmp for 30s.**

The precise thickness of photoresist layer can be measured by α-stepper facility (Tencor Alpha-Step 500 Surface profiler).

3.3.3 Pre-Bake (Soft Bake)

After spin-coating, the photoresist layer contains 1 to 3% residual solvent and may contain built-in stresses caused by the shear forces encountered during the spinning process. In order to remove residual solvent and anneal any stress in the thin layer, one must use a baking step before exposure step. Residual solvents will adversely affect both subsequent exposure and developing cycles, and the stress in the layer may result in loss of adhesion or erratic developing during the subsequent processing.

The percentage of solvent leaving in the photoresist layer will directly affect the subsequent exposure and developing time. Good selected parameters (Temperature and Time) will help the following processes run more smoothly and be more controllable. But, it is important to note that the problems caused by an incorrect pre-baking step are not fully realized until after the developing step.

Normal facilities used for baking are convention oven and hot plate. With convection oven, the solvent at surface of photoresist will be evaporated first and develop an impermeable skin at the surface, which will trap the remaining solvent inside. To avoid solvent burst effects, the heating of convection oven must go slowly that lead to more time cost for this method (more than 20min is normally required). Unlike convection oven baking, with hot plate baking, the temperature will raise starting at bottom of substrate (wafer) and work upward to the photoresist layer. So, this kind of heating will not grow an impermeable skin on the photoresist surface like convection oven baking. This will help the solvent in photoresist layer

evaporate more thoroughly. So, hot plate baking is much faster than convection oven baking, it only needs several tens seconds. But, for this kind of baking, an extremely smooth surface of plate is needed to get good thermal contact and heating uniformity.

Considering the condition of device fabrication, in this thesis we select the hot plate baking for the pre-baking process, not only for its faster, but also for its more controllable and suitable for automation.

By systematically parameters testing with the subsequence processes like exposure and developing, we finally select the working temperature at **80**℃ and baking for **80 seconds**. The baking temperature should not be selected too high, otherwise it will easily cause the photoresist lose its sensitivity to the UV light for oven.

3.3.4 Alignment and Exposure

Now the process comes to Exposure step. For only one layer fabricating process, the alignment work will come to be easier. It just needs to move the pattern onto the center of sample (wafer) or suitable position, requiring on layer to layer overlap alignment like multi-layer fabrication. As the fabrication in this thesis is only one layer process, so the introduction for the detail of alignment will be neglected.

The exposure process is one of the most important steps in the whole device fabrication. It is to make the photoresist to take a chemical reaction under the certain wavelength light exposing (normally, UV light in the range of 200—450nm.) For positive photoresist, the photoresist molecules in the area of exposed parts will break the cross-links between each other and make these parts of photoresist layer come to be solvable in the developer. For negative photoresist, the opposite chemical reaction it will happen, those exposed parts of photoresist layer will stay here after developing. A commercial facility (Karl Suss MA4 Mask Aligner) is used for exposure process in this lab. And, contacting exposure is used in this work. For this kind of exposure, we can get high spatial resolution of pattern and 1:1 pattern

transfer size. But, as it is contacting exposure, the scraping between wafer and mask will happen if the operation is not carefully. And the contaminants of photoresist on photomask from previous photolithography works will cause the failure of the following samples' photolithography. So to make sure the mask cleanness before the exposure process is very important too. (To clean the mask, acetone can be selected to remove those photoresist contaminants.)

There are several processing considerations that must be taken into account, including energy density and uniformity of UV light, exposure time and exposure ambient, etc. In this thesis, after systematical parameters testing, we choose **15mW/cm^2** as the UV light intensity, and **80 seconds** for exposure time.

3.3.5 Post-bake (Hard Bake) and Flood Exposure

As the post-bake and flood exposure are using the same facilities like pre-bake and exposure, this part just mentions something important in these two steps together.

For AZ5214 photoresist (an amphibious photoresist) used in this work, after one cycle exposure process, the photoresist is working as positive photoresist. Because negative photoresist is more suitable for lift-off process, we have to change the polarity of AZ5214 photoresist by post-baking and flood exposure. If one uses some negative photoresist (unlike AZ5214) directly, then these two steps can be jumped over.

The most critical parameter of the image reversal process is post-baking temperature. In this thesis, we set it as **100℃** (hot plate baking), Be careful, if the image reversal baking (post-baking) temperature is chosen too high (>130℃), the photoresist will thermally crosslink also in the unexposed areas, giving no pattern at the end. The baking time is selected like **80 seconds.**

A flood exposure step is also needed for reverse polarity of such kind of photoresist. In this step, the exposure will be taken without photomask. All areas of photoresist layer are flooded under UV light. Those areas which have been exposed in the first round exposure will be convert its polarity and will be solvable in

developer. The selected final parameter for this flood exposure step is **90 seconds**. This parameter selection is considered with the developing process together, to make the develop time more controllable.

By these treatments, the pattern transferred on photoresist layer will be image reversed, and the top part of this photoresist layer will have a lower dissolution rate comparing with the deep parts, which will help a T-shaped profile with overhanging lips to be formed after development.

3.3.6 Development

Once the latent image has been formed in the photoresist layer, it must be developed to produce the final three-dimensional relief image. The developing process is the most complex one among these processing steps. It has the greatest influence on the pattern quality. In order to optimize the developing process, several criteria are showed below:

1.)No (or least) reduction in original layer thickness.

2.)Minimum developing time (less than one minute)

3.)Minimum distortion and swelling during the developing process.

In this work, we used **AZ300 MIF developer** as the developer. The optimized develop time is found at around **45 seconds**.

A rinse step should be taken immediately after developing to prevent the pattern being over-developing with the residual developer on the surface of photoresist (or substrate). After the completion of the developing process, it is necessary to dry the substrate (wafer) thoroughly of all residual developers and rinses. This work can be done with nitrogen gas blowing.

Figure 3.4 shows a demo of alignment mark after those processes discussed above.

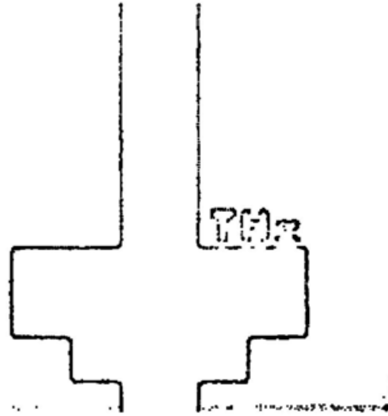

Figure3.4: Photo of an alignment mark after development.

3.4 E-beam Evaporation and lift-off

To make THz photoconductive devices (emitter or detect), a thin film metal is required to be deposited on the surface of GaAs:O substrate to form antenna and electrical contact. After photolithography processes, the pattern have been formed on the photoresist layer which will act as a mask during the metal deposition process. There are several deposition techniques are currently available for producing such metal films: 1) Evaporation, 2)Electron beam(e-beam) evaporation, 3) sputtering, 4) chemical vapor deposition. In our department, the e-beam evaporation and sputtering facilities are available. Considering the metal selected for deposition and the qualities of metal films after deposition, in this work, we select e-beam facility to do this kind of deposition work.

3.4.1 E-beam evaporation

Electron Beam (e-beam) evaporation is one of the most common methods of physical vapor deposition (PVD) of metals. Others methods are like sputtering, plasma spray deposition, evaporation. By e-beam evaporation, the metals and metal compounds such as Ti, Au, Al, Cu, Ni, TiN, TaN, can be deposited on the substrate as thin film layer.

Evaporation occurs when a source material is heated above its melting point in

a chamber, which is evacuated to a base pressure lower than 10^{-6} torr. Under this low pressure condition, the evaporated atoms will travel at high velocity in straight-line trajectories. E-beam evaporation is a method which uses accelerated electron beam as its heating source to heat material (metal or metal compound) to its melting point.

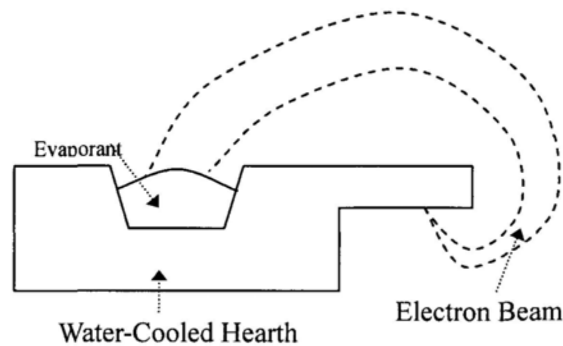

Figure3.5:Electron-Beam evaporation source

The Figure 3.5 shows the schematic structure of e-beam evaporation source [45]. Electrons are obtained from a hot filament and are then accelerated through a voltage of 10 keV before striking the source material. Appropriate provisions can be designed into the system so that impurities from the hot filament do not reach the melt. The electron beam can be scanned over the source surface to prevent non-uniform evaporation. By incorporating a number of sources in the deposition chamber, films of different compositions can be deposited sequentially. Depending on the source-substrate distance, deposition rate as high as 0.5μm/min is feasible.

The samples are mounted onto a tunable plate which is directly above the e-beam evaporation source. After evacuating the bell jar into a low pressure, the source is heated to its melting point by electron beam, then the atoms or atoms clusters of source material will leave the source and condense on the masked substrate (GaAs:O samples), leading to the deposition of metal films.

3.4.2 The material and deposition parameters selection

Normally, the metal used for PC antenna fabrication should be Aluminum (Al), as it can be easily obtained by a low price. But Al is easy to be oxidized in air, which

will decrease the performance of device in a long time scale. So some metal which is more resistive to oxidization reaction will be the first choice. From papers, Gold (Au) is the most popular metal selected for such kind of case. But, if only deposits Au layer onto the surface of substrate, the Au layer will be not easy to stick on the substrate firmly, because of the crystal lattice mismatching between the substrate material and Au material. If the adhering performance of Au layer to the substrate is not good enough, the metal layer will easily be all life-off and no pattern left during the lift-off process. Then it will cause the device fabrication failure. So, one should add some other kind of material to increase the stickiness between substrate and Au layer.

Titanium (Ti) is the one selected metal for increasing the adhesion, because Ti material has superior adhesion to GaAs substrate than Au. And, because the Ti and Au are both metal, they are easy to be combined together firmly.

So, in this work, we firstly deposited a thin **Ti layer (500 Å)** to increase adhesion of metal layer to GaAs substrate, and then deposited **Au layer (2000 Å)** to make devices.

3.4.3 Lift-off and the fabricated devices

Lift-off is the last step for antenna device fabricating on GaAs:O substrate. The metal deposited GaAs:O samples are put into a vessel with acetone solvent, and agitated with ultrasonic. About 3-5 min later, the photoresist on the top of GaAs:O surface will be solved by acetone and make the metals just above them to lift-off from the GaAs:O substrate. Then, at the end, only those metal layers directly deposited on the surface of GaAs:O will leave there and form the final device pattern. A demo after lift-off step is

Figure3.6: photo of an alignment mark after lift-off step.

also showed in Figure 3.6. **Note**: A successful lift-off step is mainly determined by the quality of those processes like photolithography and e-beam evaporation. The only thing need to take care in this step is the energy of ultrasonic. Too strong energy will cause those metals on GaAs:O to lift-off too, even they were adhered on the material.

3.5 Packaging and Wire Bonding

3.5.1 Packaging

The packaging work is just giving user an easier solution of device handling during the devices testing. A metal holder or normal printed circuit broad (PCB) can be used as such kind of hold. In this work, we chose the PCB as the holder of our GaAs:O based PC devices.

A small square hole, which is just little larger than Si lens, is dug on the back of PCB. Then the device is fixed (adhered) onto the PCB insider this square hole with Epoxy adhesive (H20E). This kind of Epoxy (H20E, www.epotek.com) can make bond between materials (metal or plastic, and so on) under 120□for 15min oven heating. If one wants to remove the device from certain holder, he (she) can put them back to the oven, and increase the heating temperature to 175□. After 1 min oven heating, the device can be taken off from the holder. So, this kind of adhesive gives one more convenience for devices packaging.

3.5.2 Wire Bonding

To make the devices works, the last process have to be done at first. That is wire bonding, a technique for giving the wire connection between small size devices to a larger electrical contact pad. Although wire bonding is the oldest attachment method, it still is the dominant technique for those devices with fewer than 200 connections. With gold or aluminum wires, the device bonding pads and the contact points on the package are connected by bonding method. Normally, ultrasonic, thermo-sonic, or

thermo-compression bonding could be selected for the boning work. The thermo-compression technique normally needs to heat the substrate to a temperature of 150℃ to 200℃, and the bonding interface temperature range from 280℃ to 350℃. In this working condition, many epoxies cannot withstand such high temperature. The ultrasonic bonding technique is a lower-temperature alternative method which relies on a combination of pressure and rapid mechanical vibration to form bonds. Considering the epoxy we used in the packaging step, we adopt ultrasonic bonding method in this work.

Figure 3.7 [46] shows the operation process of ultrasonic wire bonding. The wire is fed from a spool through a hole in the bonding tool. When the bonding tool is move down onto the position which bonding pad is located, an ultrasonic vibration at 20 to 60 kHz is added on the tool causing the end of metal wire to deform and flow (even at room temperature). After finishing the first bond on device bonding pad, the tool is raised up and move to the position of contact point of package to do the second bond. This operation is the same but the bonding parameters (ultrasonic energy, time, pressure, etc.) needs to be adjusted corresponding to the package material. After the bond to the package is formed, the tool is raised again and a clamp pulls and breaks the wire as showed in Figure3.7(e).

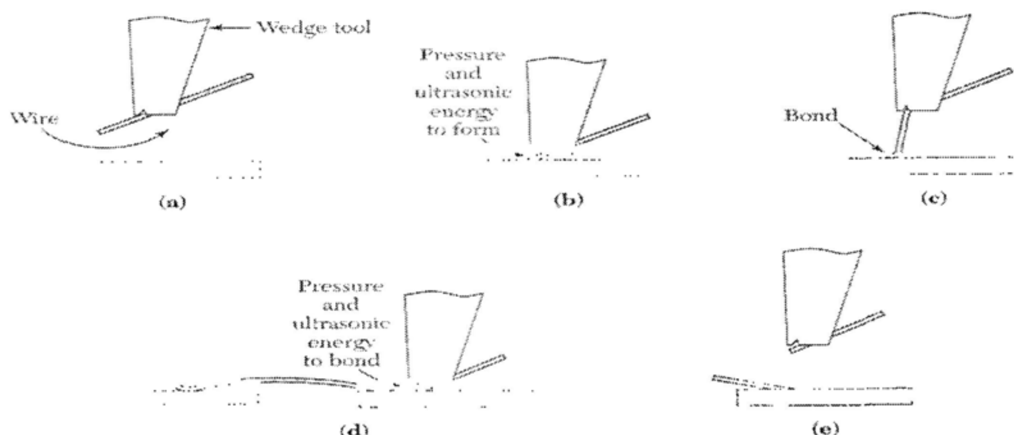

Figure 3.7: Ultrasonic bonding process. (a) Tool guides wire to the package. (b) pressure and ultrasonic energy form bond. (first bond) (c and d) Tool feeds wires and repositions, and ten form the second bond. (e) Wire broken at the bond.

3.6 Summary

In this chapter, we have discussed those important factors for fabricating a photoconductive antenna on GaAs:O substrate. After getting a good material though the preparation method which introduced in chapter 2, we have just finished the first step to the success. Without good device fabricated on such kind of substrate, we can not achieve good THz wave generation performance. So, for certain application, a suitable antenna structure is required. For example, as we are focusing on the high power generation potential of PC device at the frequency about 0.3 THz, we select normal dipole antenna structure and design its scale to match the requirement.

To realize the design on GaAs:O material, we used normal photolithography and E-beam evaporation methods. Before them is a high quality cleaning process to avoid those possible failure may caused by some contaminations during the photolithography process. In a 100 class (<100 particles/m^3 level) working condition and several times cleaning in those corresponding solutions (acetone, DI water and isopropanol) are required for such kind of preparing work before photolithography.

In photolithography part, one issue should be mentioned here, the parameters selected for each step need to demonstrate the convenience and quality of those steps after them. For example, a longer exposing time may cause the develop speed to decrease. Too fast develop speed will cause the operating difficulty to user, because a little un-precise time counting during this step will lead to the over develop result and make failures on devices. Others like softbake temperature and time, affect the sensitivity of photoresist to the UV exposure and at the end affect the parameters selecting in the step of Expose and then pass to the parameters of hard bake, flood and so on. So, even small change in the parameters in the earlier steps will lead to those parameters in following steps to change accordingly.

And it is also easy to understand that for different substrate materials and photoresists, the parameters for each step of photolithography process will be

normally different, because each pair substrate material and photoresist should have different viscosity between them. Although each kind of photoresist has its own operating manual, considering the certain material use, those parameters should be adjusted for achieving best photolithography result case by case.

So, to fabricate device successfully, one should optimize all those parameters in the photolithography process for his certain material. A possible simple method for finding the relative good working parameters is like following: At first, fix most parameters as the manual suggests and leave one for optimize. And then, select some possible values (discrete values with certain step) for certain parameter to test their effect on the final result of photolithography. (The step for discrete value can be large first and then decrease step by step.) After optimize this parameter, one can use the same method to optimize other parameters, until all the parameters are optimized at the end.

In this work, after this kind of parameters optimizing, we find the best operating condition of photolithography for our GaAs:O samples like Table 3.2 shows.

Material	**Coating**	**Soft Bake**	**1st Expose**	**Hard Bake (PEB)**	**Flood Expose**	**Develope**
GaAs:O	1200 (9s) /3000(30s)	80℃ /80s	80s	100℃ /80s	90s	45-60s

Table3.2: Parameters for photolithography.

After the E-beam evaporation process the Ti (500 Å) /Au (2000Å) metal layers are deposited on the surface of GaAs:O material. During this process, one should keep the surface of samples clean and without H_2O residue left before putting them into the chamber, otherwise the metal can not adhere well on the material surface, which at the end will cause device failure during the lift-off or wire-bonding process.

After those processes mentioned above and the packaging and wire-bonding, the whole device fabrication is finished. Now, the PC devices are ready for testing.

As there are several devices with different substrates and antenna structures will be tested in the following chapters, for easy tracing, each device will be named. The list of devices is showed in Table 3.3.

Substrate Material	Ion type	Ion implantation dosage	Annealing temperature	Dipole Antenna parameters			Mark of Devices
				D_s (L_s+W_s) (μm)	W_a (μm)	d_{gap} (μm)	
SI GaAs (110)	O^+	500keV/6×$10^{13}$$cm^{-2}$ 800keV/6×$10^{13}$$cm^{-2}$ 1200keV/1×$10^{14}$$cm^{-2}$	300℃/5s 550℃/60s	195 (170+25)	25	20	Dipole_1
				195 (170+25)	25	20	Dipole_1_2
				95 (70+25)	25	20	Dipole_2
				45 (20+25)	25	12	Dipole_3
		500kev/2.5×$10^{13}$$cm^{-2}$ 800kev/2.5×$10^{13}$$cm^{-2}$ 1200kev/4×$10^{13}$$cm^{-2}$	300℃/5s 500℃/60s	195 (170+25)	25	20	Dipole_4
							Dipole_4_2
				95 (70+25)	25	20	Dipole_5
				45 (20+25)	25	12	Dipole_6
				40 (30+10)	5	5	Dipole_7
LTG GaAs				40 (30+10)	5	5	Dipole_8
				195 (170+25)	25	20	Dipole_9
GaAs	As^+	50KeV/5×$10^{15}$$cm^{-2}$ 100KeV/5×$10^{15}$$cm^{-2}$ 200KeV/5×$10^{13}$$cm^{-2}$	600℃/30mins (furnace)	195 (170+25)	25	20	Dipole_10

Substrate Material	Ion type	Ion implantation dosage	Annealing temperature	Spiral Antenna parameters			Mark of Devices
				Linewidth(μm) /separation(μm)	Turns	Figure / gap (μm)	
SI GaAs (110)	O^+	500kev/6×$10^{13}$$cm^{-2}$ 800kev/6×$10^{13}$$cm^{-2}$ 1200kev/1×$10^{14}$$cm^{-2}$	300℃/5s 500℃/60s	10/10	3.5	2/2	Spiral_1
					2.5		Spiral_2
GaAs (100)		500kev/2.5×$10^{13}$$cm^{-2}$ 800kev/2.5×$10^{13}$$cm^{-2}$ 1200kev/4×$10^{13}$$cm^{-2}$	300℃/5s 500℃/60s	10/10	3.5	2/2	Spiral_3
					3		Spiral_4
LTG GaAs			300℃/5s 500℃/60s	10/10	2.5	2/2	Spiral_5

Table3.3: Devices and their parameters

Chapter 4: Pulsed THz wave generation pumped by femtosecond laser

4.1 Introduction

Pulsed THz wave generated by fs laser pumping is a very common technology used in terahertz time domain spectroscopy (TDS)[65]. The transient photocurrent induced by fs laser pump will emit EM wave to the space from the PC devices. A higher strength of transient photocurrent is normally corresponding to a higher THz output power. The potential THz power generation ability of the PC devices is mainly determined by the material on which the devices fabricated. As discussed in chapter 2, the LTG GaAs is common material used for THz wave generation by Photoconductive method, for its high resistivity, ultrashort carrier lifetime and high breakdown field. But it still has disadvantages on some aspects, for example, the critical preparation condition and the relative low saturation level of pumping power. Some possible substitute materials of LTG GaAs have been studied during the past several years. In this work, we try to optimize the preparation condition of oxygen ion implanted GaAs materials and to see whether it can obtain such kind of THz generation properties like LTG GaAs materials, or has some prior aspects than LTG GaAs. In this chapter, we will focus on the pulsed terahertz generation properties of GaAs:O based PC devices.

At first, some theoretical models on pulsed terahertz wave generation and its saturation behavior will be reviewed in the early part of this chapter. And then, several experimental systems (power measurement and calibration, FTIR, TDS, and CW background illumination) for our devices testing will be introduced. The third part of this chapter is focusing on the THz generation properties of GaAs:O materials. Several samples with different preparation conditions and device

structures are tested and compared. Some devices fabricated on GaAs:As and LTG GaAs materials are also contrastively tested for better understanding of the advantage and disadvantage of GaAs:O in the field of THz generation.

4.2 Generation mechanisms

When a biased semiconductor is pumped by an ultrashort (such as, fs) laser pulse , the rapid change of photocurrent through the emitter causes the emission of ultrafast electromagnetic wave (such as THz wave). The transient photocurrent density J (given by Eq.(4.1)) arises from the rapid change of carrier density *via* ultrashort laser pumping and the acceleration of the photogenerated carrier under an electric filed.

$$J = env \tag{4.1}$$

Where e is the elementary charge, n is the carrier density and v is the carrier velocity.

4.2.1 Drude-Lorentz Model

To model this carrier transports in semiconductor, a simple one-dimensional Drude-Lorentz model[66, 67] can be used. The time dependence of carrier density is given by equation (4.2), where τ_{trap} is the carrier trapping time (Here we use τ_{trap} to present the effective carrier lifetime τ, for $1/\tau=1/\tau_{trap}+1/\tau_r+1/\tau_{drift}$, since the trapping time is smaller than recombination time and the carrier drift time). G(t) is the generation rate of free carriers generated by the laser pulse:

$$\frac{dn}{dt} = -\frac{n}{\tau_{trap}} + G(t)\,. \tag{4.2}$$

As discussed in Chapter 2, the carrier trapping time is related to the concentration of defects (trapping centers). The generation rate is proportional to the incident light power.

The time dependence of average carrier velocity is in the Drude-Lorentz picture

is given as:

$$\frac{dv}{dt} = -\frac{v}{\tau_s} + \frac{e}{m^*} E_{loc}, \tag{4.3}$$

where τ_s is the momentum relaxation time, m^* is the effective mass of carrier, and the E_{loc} is the local electric field. The local electric field is smaller than the applied bias field (E_b), because of the existence of the space-charges field E_{sc},

$$E_{loc} = E_b - E_{sc} = E_b - \frac{P_{sc}}{\eta_{geo}\varepsilon}, \tag{4.4}$$

where P_{sc} is the space-charge polarization induced by the carriers' separation in the electrical field, η_{geo} is the geometrical factor of material which equals to three for an isotropic dielectric material, ε is the permittivity of the substrate. Without the applied electric bias E_b, the effective carrier velocity will be slowed down by the carrier-carrier scattering (collision) and the screening of space-charge.

The time dependence of the space-charge polarization is given as:

$$\frac{dP_{sc}}{dt} = -\frac{P_{sc}}{\tau_r} + J, \tag{4.5}$$

where τ_r is the carrier recombination time. The band-to-band recombination or Auger recombination is expected to be roughly on the order of 100 ps[68, 69].

Using the Green's function method, one can find the solution of Eq.(4.5) with inserting Eq.(4.1):

$$P_{sc} = e \cdot \exp(\frac{-t}{\tau_r}) \int_{-\infty}^{t} dt' n(t') v(t') \exp(\frac{t'}{\tau_r}). \tag{4.6}$$

The physical meaning of the convolution integral is that the photogenerated carriers move in the applied electric field with a velocity v until they are trapped by the defects[70]. The screening of space-charge field will stop increasing once the photogenerated carriers are trapped by the defects. However, the trapped carriers still continue to statically contribute to the screening on the applied electric field until these carriers fades by recombination. As the decay time of recombination is in the order of 100 ps, the static screening of trapped carrier is a long-living

phenomenon compared with the ultrashort pumping light which is normally on the level of sub-ps (5~300fs).

In an elementary Hertzian dipole theory, the far radiation field E_{THz} is proportional to the change of photocurrent,

$$E_{THz} \propto \frac{\partial J}{\partial t} \tag{4.7}$$

By inserting Eq.(4.1) into Eq.(4.7), the electric field of radiation can be expressed as,

$$E_{THz} \propto ev\frac{\partial n}{\partial t} + en\frac{\partial v}{\partial t} \tag{4.8}$$

From Eq.(4.1-4.8) one can know the terahertz radiation field will increase with the intensity of incident laser pulse at first, and then fall into a saturation state. This is because the increasing of space-charge screening is also proportional to the intensity of incident light. And, terahertz radiation field E_{THz} can also be increased by the increasing of carrier velocity which is caused by the increasing of the electrical bias field.

From the above discussion, the saturation is related to the space-charge screening, however, another screen effect also can give contribution to the saturation behavior. The THz field generated from PC emitters is also related to the impedance of antenna which will shares the applied electric field with the photoconductive gap where the pumping light inject. An increasing of photocurrent will also increase the voltage on the antenna impedance leading to the decrease of local electric field for carriers' acceleration in photoconductive gap area. This kind of screening is called radiation field screening, and it is also considered as the main reason for the pump saturation behavior.

For detailed study of the saturation behavior, two saturation models commonly used by researchers will be introduced in the following subsection. One is for large aperture PC emitters[71-73] (Conducting electrodes with a spacing in the range of 500μm to 30mm), and the other is for small-size PC emitters[74, 75].

4.2.2 Saturation behavior of Large aperture PC emitters

For THz PC emitters, whose dimensions are much larger than the wavelength of the emitted THz wave, the saturation behavior is approximately described by equation (4.9) for the radiation near electric field[72]:

$$E_{THz} = -E_b \frac{\sigma_s Z_0}{\sigma_s Z_0 + (1+\sqrt{\varepsilon})}. \tag{4.9}$$

Where E_b ,as mentioned before, is the applied bias field. And the σ_s is the surface photoconductivity, ε is the dielectric constant of the photoconductor. And Z_0 is the characteristic impedance of the free space, about 377Ω[73].

The surface photoconductivity can be expressed by[76, 77]:

$$\sigma_s(t) = \frac{e(1-R)(1-\exp(-\alpha l))}{\hbar\omega} \int_{-\infty}^{t} dt' \mu(t-t') I_{opt}(t') \cdot \exp[\frac{-(t-t')}{\tau_{carrier}}], \tag{4.10}$$

where R is the optical reflectivity, $I_{opt}(t)$ is the incident optical pulse intensity as function of time, l is the thickness of semiconductor absorption layer. $\tau_{carrier}$ is the lifetime of the excited carriers, which is a function of trapping time τ_{trap} recombination time τ_r, and drift carrier lifetime τ_{drift}:

$$\frac{1}{\tau_{carrier}} = \frac{1}{\tau_{trap}} + \frac{1}{\tau_r} + \frac{1}{\tau_{drift}}. \tag{4.11}$$

From Ohm's law, the surface current J_s is given by [78]:

$$J_s = \sigma_s (E_b + E_{THz}) \tag{4.12}$$

Insert Eq. (4.9) into Eq.(4.12), then we can get:

$$J_s = E_b \frac{\sigma_s (1+\sqrt{\varepsilon})}{\sigma_s z_0 + (1+\sqrt{\varepsilon})} = E_b \frac{\sigma_s}{\frac{\sigma_s Z_0}{(1+\sqrt{\varepsilon})} + 1}. \tag{4.13}$$

For those semiconductors under high electric fields, the Ohm's law does not apply(i.e. greater than 5.0kV/cm[71]), the Eq.(4.10) and Eq.(4.12) should take into account the electric field dependence of the surface conductivity.

The value of the radiation electric field on a distance z from the emitter is given

as

$$E_{THz,far}(z) \cong -\frac{1}{4\pi\varepsilon c^2}\frac{\partial J_s}{\partial t}\frac{A}{z} = -\frac{A}{4\pi\varepsilon c^2 z}E_b\frac{\frac{\partial\sigma_s}{\partial t}}{(1+\frac{\sigma_s Z_0}{1+\sqrt{\varepsilon}})^2}, \tag{4.14}$$

where c is the speed of light, A is the illuminated area of the emitter.

From Eq.(4.14), one can easily find the amplitude of THz wave measured in a distance z from emitter is proportional to the change of surface photoconductivity and the applied bias. As the beam size of THz wave will expands with the increasing of distance z, to collect all THz waves generated by emitter, one need to use some components (like Si lens, Parabolic mirror, and Picarin lens) to adjust the beam shape and focus them.

As the Eq.(4.14) is still complex, it is not easy to grasp the sprit of saturation behavior. To get simple expression for better understanding on the saturation behavior, one could do following simplify work.

Suppose the surface current increases to its maximum on the order of the pulsewidth of the radiated field τ_p[71], then one can assume that

$$(\frac{\partial J_s}{\partial t})_{\max} \cong \frac{J_{s,\max}}{\tau_p} = \frac{E_b}{\tau_p}\frac{\sigma_{s,\max}(1+\sqrt{\varepsilon})}{\sigma_{s,\max}z_0+(1+\sqrt{\varepsilon})} = \frac{E_b}{\tau_p}\frac{\sigma_{s,\max}}{1+\frac{\sigma_{s,\max}Z_0}{(1+\sqrt{\varepsilon})}}. \tag{4.15}$$

So, the electric field of THz wave in a distance z from emitter will have its maximum value as:

$$E_{THz,far,\max}(z) \cong -\frac{1}{4\pi\varepsilon c^2}(\frac{\partial J_s}{\partial t})_{\max}\frac{A}{z} = -\frac{A}{4\pi\varepsilon c^2 z}\frac{E_b}{\tau_p}\frac{\sigma_{s,\max}}{1+\frac{\sigma_{s,\max}Z_0}{(1+\sqrt{\varepsilon})}}. \tag{4.16}$$

Note the time σ_s reaches it maximum is not the time of μ and $I_{opt}(t)$ reach their maximum respectively, because the relatively slow increase in the conductivity compared with the rapid varying optical intensity is presented by the slow change of $\mu(t)$ in this theory model. So, here uses the average incident optical fluency F to simplify the question.

$$F = \int_{-\infty}^{\infty} I_{opt}(t)dt = \int_{-\infty}^{\infty} I_0 \exp(\frac{-t^2}{T_0^{\ 2}})dt = \sqrt{\pi} I_0 T_0 = \frac{E_{opt}}{A}, \tag{4.17}$$

Where E_{opt} is the measured average optical energy. A is as defined before, the illuminated area of the emitter. Then,

$$I_{opt}(t) = \frac{F}{\sqrt{\pi} T_0} \exp(\frac{-t^2}{T_0^{\ 2}}). \tag{4.18}$$

Insert Eq.(4.18) into Eq.(4.10), then we can get:

$$\sigma_s(t) = \frac{e(1-R)(1-\exp(-\alpha l))F}{\hbar\omega} \int_{-\infty}^{t} dt' \mu(t-t') \frac{1}{\sqrt{\pi} T_0} \exp(\frac{-t^2}{T_0^{\ 2}}) \cdot \exp[\frac{-(t-t')}{\tau_{carrier}}]. \tag{4.19}$$

Now, let using $\mu_{eff}(t)$ to present the time dependant part in the Eq.(4.19),

$$\mu_{eff}(t) = \int_{-\infty}^{t} dt' \mu(t-t') \frac{1}{\sqrt{\pi} T_0} \exp(\frac{-t^2}{T_0^{\ 2}}) \cdot \exp[\frac{-(t-t')}{\tau_{carrier}}]. \tag{4.20}$$

When $\mu_{eff}(t)$ reach its maximum $\mu_{eff,max}$, the surface photoconductivity will also reach its maximum value $\sigma_{s,max}$. Insert Eq.(4.20) and Eq.(4.19) into Eq.(4.16), then one can get the simple expression of far field THz radiation field:

$$E_{THz,far,\max}(z) = -\beta_s \frac{F}{F_{s,\max} + F}, \tag{4.21}$$

Where

$$F_{s,\max} = \frac{\hbar\omega(1+\sqrt{\varepsilon})}{e\mu_{eff,\max}(1-R)(1-e^{-\alpha L})Z_0} \tag{4.22}$$

$$\beta_s = \frac{A}{4\pi\varepsilon c^2 z \tau_p} \frac{(1+\sqrt{\varepsilon})}{Z_0} E_b \tag{4.23}$$

With a given ultrashort pumping laser, the value of $F_{s,max}$ will be different in different materials, which presents the different saturation behavior of materials. The main reason should be the different value of effective carrier mobility of materials (μ_{eff}), which mainly confined by the density of defects[79].

The value of $F_{s,max}$ is also affected by the change of absorption coefficient under high incidence light, which can both influence the refractive index of material ($n_{refractive} = \sqrt{\varepsilon}$)and the power efficiency of pumping light ($(1-R)(1-\exp(-\alpha l))$) in

some level. Maybe this is a possible reason for some experimental results obtained by J.Zhang [80], where the THz field amplitude will have an increase with the increasing power of the additional CW pumping.

Normally, the curve of THz electric field versus the intensity of pumping light will saturate at the value β_s, when the surface photoconductivity becomes comparable to the reciprocal of the impedance of antenna. The additional pump light adding on the emitter after the saturation threshold will slight change the THz electric field through the term $\sqrt{\varepsilon}$ in β_s. Under high pumping condition, the change of refractive index will come to be obvious through the bandfilling effect, bandgap shrinkage effect and free carrier absorption effect[52, 53]. The integration effect normally causes the refractive index to decease[81]. When the refractive index changed, it also presents the change of effective dielectric constant, as $\sqrt{\varepsilon} = n$. This may be the possible reason that the SI GaAs material will have a decay phenomenon under higher pumping power in the paper[51].

4.2.3 Saturation behavior of small-size PC emitters

For a small-size PC emitter, the theory model of large aperture PC emitters will be not valid all the time. Because large aperture PC emitters have much smaller center wavelength compared to the current distribution dimensions, the radiated field can be well approximated to plane waves. And that model assumes the inward and outward radiated fields are equal, this is not true in case of a Hertzian dipole antenna on a dielectric material[82].

Normally, small-size THz PC emitter can be looked as a photoconductive antenna with external circuits like Figure 4.1 shows. In this equivalent circuit picture, we also neglect the capacitance presented by the photogap, because the capacitance in photogap is on the order of ~100aF for small dimensions of THz PC emitter[75]. The planar antenna can be presented as a load with an impedance Z_a (A resonant structure is assumed for the dipole antenna used in this work), which has

only resistive part.

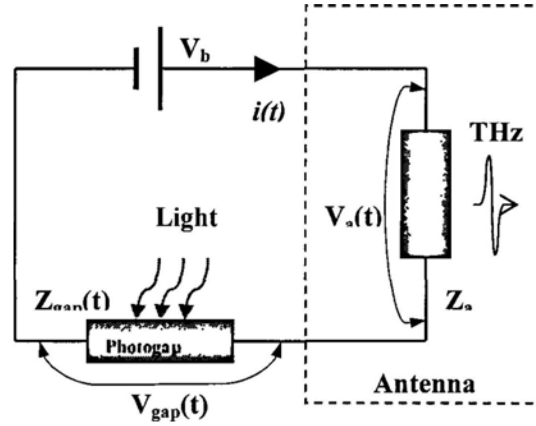

Figure4.1: Schematic of equivalent circuit of GaAs:O based PC antenna.

Without light pumping on the photogap area, the applied bias are mainly occupied by the photogap (because the impedance of photogap $Z_{gap}(0)$ is much larger than that of antenna Z_a), and generate constant dark current i_0 in the emitter. When the photogap area is illuminated by ultrafast pumping laser, the impedance of photogap $Z_{gap}(t)$ will decrease dramatically and be modulated by pumping laser through the change of the density of photogenerated carriers. The change of Z_{gap} will cause photocurrent *i(t)* to be generated with a given applied bias. When the photocurrent passes though the antenna, the THz waves are generated and radiate away. So we can get the expression of $V_{gap}(t)$ as:

$$V_{gap}(t) = V_b - V_a = V_b - i(t)Z_a . \tag{4.24}$$

As we know, the photogenerated current density in the photogap is given by:

$$j_{pc}(t) = en(t)\mu E_{gap}(t) = en(t)\mu \frac{V_{gap}(t)}{d_{gap}}, \tag{4.25}$$

where d_{gap} is the distance between the two terminals of antenna (metal electrodes).

If take look $E_{gap}(t)$ in detail, one can find the “screening” effect:

$$E_{gap}(t) = \frac{V_{gap}(t)}{d_{gap}} = \frac{V_b}{d_{gap}} - \frac{i(t)Z_a}{d_{gap}} = E_b - E_a(t), \tag{4.26}$$

where

$$E_a(t) = \frac{i(t)Z_a}{d_{gap}}, \tag{4.27}$$

E_a is the electric field applied on the antenna and contributes to the generation of THz wave. The increasing of E_a will cause the electric field E_{gap} which added on the gap to decrease, like a screening effect. So this kind of screening caused by the radiation field is normally called as "radiation field screening".

The time-varying photocurrent *i(t)* can be obtained by multiplying the photocurrent density with the acting area A as:

$$i(t) = j_{pc}(t) \cdot \frac{Al}{d_{gap}}. \tag{4.28}$$

Where A is the area of photogap which illuminated by pumping laser, *l* is the absorption depth of substrate.

Insert Eq.(4.25) and Eq.(4.24) into Eq.(4.28), we can get new expression of *i(t)*:

$$i(t) = V_b \frac{en(t)\mu \cdot \frac{Al}{d_{gap}^{\ 2}}}{1 + Z_a en(t)\mu \cdot \frac{Al}{d_{gap}^{\ 2}}}. \tag{4.29}$$

Using carrier mobility σ_{pc}(t) in the photogap to simplify the term of $en(t)\mu$, we can obtain a similar expression like Eq.(4.13)

$$i(t) = V_b \frac{\sigma_{pc}(t) \cdot \frac{Al}{d_{gap}^{\ 2}}}{1 + Z_a \sigma_{pc}(t) \cdot \frac{Al}{d_{gap}^{\ 2}}}, \tag{4.30}$$

Then the far field THz can be deduced by taking time derivative of Eq.(4.30):

$$E_{THz,pc}(t) \propto \frac{di(t)}{dt} = \frac{AlV_b}{d_{gap}^{\ 2}} \cdot \frac{\frac{d\sigma_{pc}(t)}{dt}}{(1 + \frac{\sigma_{pc}(t)Z_a Al}{d_{gap}^{\ 2}})^2} \tag{4.31}$$

From Eq.(4.30) and Eq.(4.31), we can find these expressions in this model are similar to Eq.(4.13) and Eq.(4.14). So, small-size PC emitter should also have similar equations like Eq.(4.21-4.23) to describe the saturation behavior,

$$E_{THz,pc} = -\beta_{pc} \frac{F}{F_{s,pc} + F} . \quad (4.32)$$

The main difference of these two models in the expression equation of saturation is the impedance of antenna, which relates to the dimensions of emitter. The antenna impedance of small-size PC emitter can be calculated by[83]:

$$R_{a,rad} = 10\pi^2 (\frac{L_{ac}}{\lambda})^2 \quad (4.33)$$

In some paper, the saturation behavior is also looked as the depletion of the electrostatic energy stored in the PC gap. This kind of energy is partly released after the photoexcitation as THz radiation energy. So, one phenomenon should have not only one possible explanation. Researcher should know the theoretical model is only a simple description of natural phenomenon, but not the natural phenomenon itself.

4.3 Experimental systems

As discussed above, when ultrafast light pulse incites the biased antenna which fabricated on GaAs:O (or LTG GaAs) substrate, the terahertz wave will be generated. To test the Pulsed THz generation performances of the GaAs:O materials grown by us, we use femtosecond (fs) mode-locked Ti:sapphire laser as the pumping source. The pulse width of this laser is around 100fs (FWHM), and the repetition rate is about 82MHz. Its center wavelength is adjusted to ~800nm.

4.3.1 THz wave generation system

As Figure 4.2 shows, the fs laser pulse is focused by an objective lens onto the photogap area of PC antenna which fabricated on GaAs:O substrate. A DC bias is also added onto the PC antenna to give an applied electric field on the photogap. The generated THz wave beam will be reshaped by Si lens, and then be focused into 4.2K liquid-helium-cooled Si bolometer by a pair of off-axis parabolic mirrors. The intensity of THz wave can be measured by Si bolometer detector (described in mV

units). This kind of Si bolometer has a response from 0.09 to 3 THz and a noise equivalent power of ~$1.5x10^{-13}$ $W/Hz^{1/2}$.

As the output data of the Si bolometer is a voltage signal. If one wants to know the real power of THz wave in μW units, a calibration work is required. In this work, we use a thermal source as the blackbody radiation source to radiate electric wave to calibrate the Si bolometer detector [84].

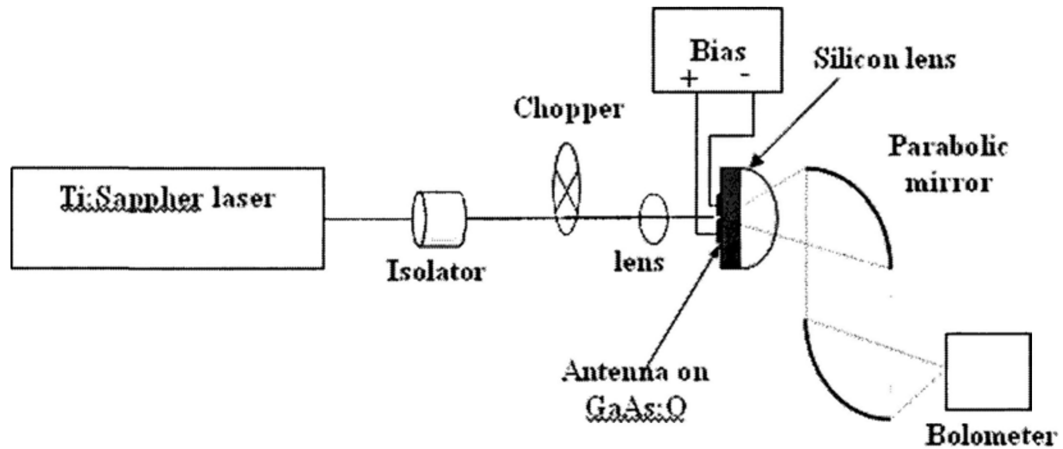

Figure4.2: Schematic of experimental setup for THz generation by fs laser pumping. (THz Power measurement)

After very careful calibration, the relationship between the real power in μW units and the measured value of Si bolometer in mV units is obtained. For our case, 1mV from the Si bolometer (channel 1000) output voltage refers to around 0.02μW real THz power generated by PC antenna **(1mV≈0.02μW),** without including the chopping loss and calibration distance decay factor during the calibration. If count them in, then one should multiply the original one with the chopping ratio 2 and the calibration decay ratio 2.45 ($R_{cal}(0)/R_{cal}(30)$=35.7/14.56=2.45, Supposing the distance is 7.5*2+15=30cm from device to bolometer, $R_{cal}(z) = 12.56 + 23.14e^{-z/12.26}$. The 7.5cm in equation is the focal length of parabolic mirror). Then the modified relationship will come to be 1mV≈0.98μW (0.02*2*2.45= 0.98).

But in this thesis, without additional mention, we use the former one **(1mV≈0.02μW)** as the calibration ratio for calculate the real THz power, to have easier comparison with other reference papers supposing they were also not

including the chopping loss and calibration distance decay factor.

Then, one can estimate the real THz output power generated from GaAs:O based PC devices in μW unit through this kind of relationship, after getting the measurement data from Si bolometer.

Note: The calibration method with blackbody radiation may have some errors during the calibration procedure, like following: 1). As one can see the blackbody radiation source used for this calibration is not really a blackbody, there should be some difference in the relationship between the radiation energy (for certain wavelength) and the operation temperature from that calibration calculated assuming a true blackbody. 2). The slight temperature instability of the blackbody radiation source, the inaccurate calculated effective radiation aperture of blackbody source compared with the aperture of bolometer detection window after passing some distance, and the effect of inserted filter (crystal quartz or Black polyethylene) in the bolometer, will all bring some calibration errors into the final calibration results. 3). The spectral response of the bolometer is assumed to have a rectangle shape here, but the real response of bolometer decreases slightly with the decrease of the frequency.

To overcome some possible calibration errors encountered in this method, one can try to use some laser sources, which has a higher temperature stability and a better collimation beam shape, to replace the blackbody radiation source [85].

About the Si lens used in this experimental system, maybe someone will have some question like, "As the pair of parabolic mirrors are used in the system, why the Si lens still be adopted?" The main reasons are as follow:

1.) The large difference between the dielectric constant of SI GaAs substrate (where GaAs:O layer grown on) and that of air, will cause strong reflection at the dielectric-air interface at the backside of substrate, like Figure 4.3(a) shows.

2.) The reflective waves will form standing waves for certain frequency (wavelength) THz components in the substrate. The more power are reflected back from the interface of dielectric-air, the substrate modes will be more obvious and

leads to more power to be trapped inside of the substrate.

So, to decrease these unwanted effects, a material with lower dielectric constant (which is between GaAs and air), is desired. Silicon is one of the best choices for its low cost and easy achievement. By fabricating Silicon bulk material into hemisphere or hyper-hemisphere, the detection efficiency will be much enhanced, like Figure 4.3(b) shows.

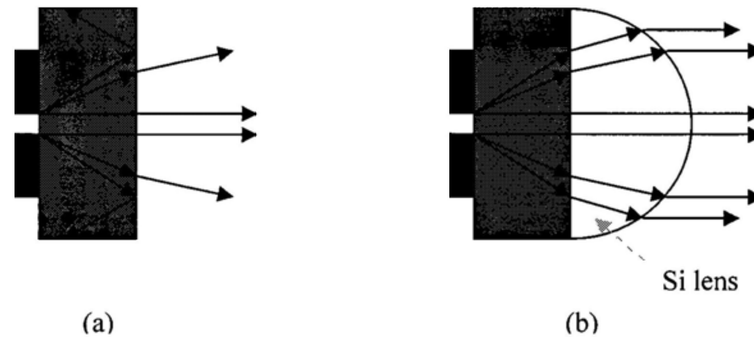

Figure4.3: The increase of detection efficiency with Si lens.

4.3.2 FTIR system for THz wave spectrum measurement

The system discussed above can only tell us information about THz power, it can't tell us any spectrum information of the THz wave generated by GaAs:O materials. If one wishes to know the frequency components of such THz wave, a spectrum measurement system should be added. One of spectrum measurement system is Martin-Puplett-type Fourier transform infrared spectrometer. M-P type interferometer (originally produced by Martin and Puplett in 1969 [86]) is a polarization interferometer similar to the well-know Michelson interferometer. But, comparing with the classical Michelson interferometer, M-P polarization interferometer can get higher modulation efficiency with the polarizing beam splitter and more uniform performance in a wide spectral range. M-P polarization interferometer is the most popularly used interferometer system in THz frequency range and sub-millimeter wavelength range. In this work, we also set up a Martin-Puplett type polarization interferometer system, cooperating with Fourier transform mathematic calculation method to get the information of THz frequency

components. The schematic of such system is showed in Figure 4.4.

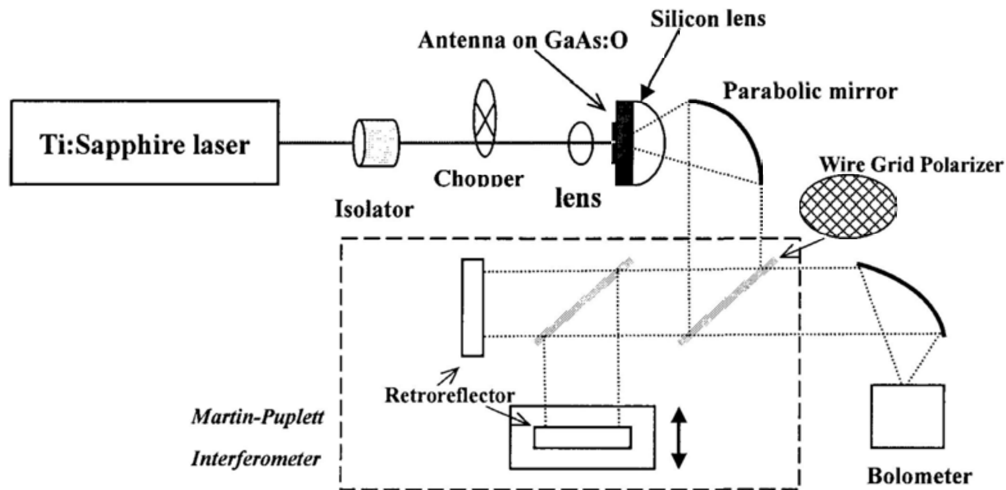

Figure4.4: Schematic of Martin-Puplett-type Fourier Transform Infrared Spectrometer (FTIR) System.

Two wire grid polarizers are used as the splitter and polarization selection mechanism. The THz wave beam generated by PC device (emitter) will be reshaped to a parallel beam with a Si lens and a parabolic mirror. Then use the first wire grid polarizer near the parabolic mirror is used to select a certain percents of THz wave beam and reflect them into the interferometer, by controlling the polarization of wire grid. The propagating THz beam will be divided into the transmission beam and the reflection beam by 50:50, with the second wire grid polarizer. Two retroreflectors are used to reflect back these two separated beams. One of them is fixed, and the other is mounted on a translation stage. The two reflected beams from the retroreflectors will come back and be focused into Si bolometer detector by the second parabolic mirror. By adjusting the path length of the movable arm, one can get the interference curve (power intensity vs. difference of path length). The different path length between these two propagation beams also means a different time delay between them. Then, after changing the interference curve into time domain (power intensity versus difference delay time) and using Fourier transform calculation method, one can easily get the frequency domain information of such THz wave generated by GaAs:O based PC devices.

4.3.3 TDS system for THz wave spectrum measurement

Another approach for THz wave spectrum measurement is TDS (time domain spectroscopy) system. This kind of system is the mostly used technique for measuring THz wave spectrum. Unlike M-P FTIR system, TDS system don't utilize interference conception. It is more like the system for carrier lifetime measurement as introduced before. As the semiconductors and some crystals also have slight response effect to the THz waves like normal light. The fast varying effects of materials caused by THz wave can also be detected by pump-probe technology. Then from the measured data, one can know the relative intensity of THz wave versus the time delay between the pump and probe light. Again, with the help of Fourier transform mathematic method, one can finally get the information of frequency components of THz wave generated by GaAs:O based PC devices.

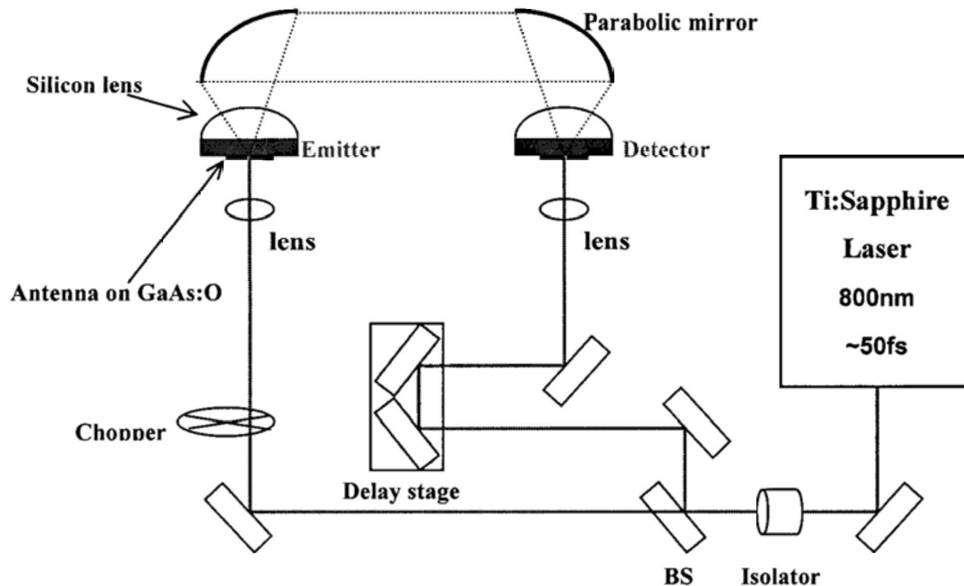

Figure4.5: Schematic of Terahertz Time-Domain Spectroscopy System.

Figure 4.5 shows the schematic of the normal Terahertz Time domain spectroscopy system. The ultrafast laser beam is separated by a beam splitter. One beam is used as the pump light, and the other is used as the probe light. The pump light will be focused onto the biased photogap of PC antenna, with an objective lens. The probe light will propagate in a delay sub-system before it be focused onto the

unbiased photogap of PC detector, which can response to THz wave in broad spectrum range. Normally such kind of PC detector is fabricated on the LTG GaAs substrate. In this work, we also used a LTG GaAs based dipole antenna (with antenna gap 35μm) as the detector.

By changing the delay line of this delay sub-system, the probe light will scan the PC detector in time domain. The interaction of THz wave and the probe light in the material will be presented as the intensity of photocurrent from the PC detector. The time-domain waveform of photocurrent can be directly looked as the THz wave intensity curve in time-domain. To increase the signal-to-noise ratio, a chopper is used on the arm of pump light. The pump light was modulated at 1KHz, and the output photocurrent signal from PC detector was measured with a lock-in amplifier. This kind of lock-in measurement technique was also adopted in M-P FTIR system and THz generation system above, in those case, the signal to amplifier is from Si bolometer detector and the chopping frequency is set around **200Hz**.

4.3.4 Experimental setup for studying pulsed THz wave generation with CW background illumination.

THz power will increase with the increasing of pumping power, and at the end reaches to its saturation level for the reason of pumping power saturation behavior, as discussed in the Chapter 4.2. The main reason is suggested as bias-filed screening (space charge screening and radiation field screening) [51, 68, 87-92] . To particularly investigate the screening effect, a CW background illumination is utilized to generate additional screening effect. In such experiment, we used a Golay Cell detector to replace bolometer detector, and place it very close to the THz PC emitter. The whole experimental setup is showed in Figure 4.6. The fs laser beam and CW light beam are combined together with a beam splitter, and then focused onto the PC antenna. In this experiment, the chopper only modulate fs laser beam to take data of pulsed THz wave signal. The chopping frequency is set about 20Hz.

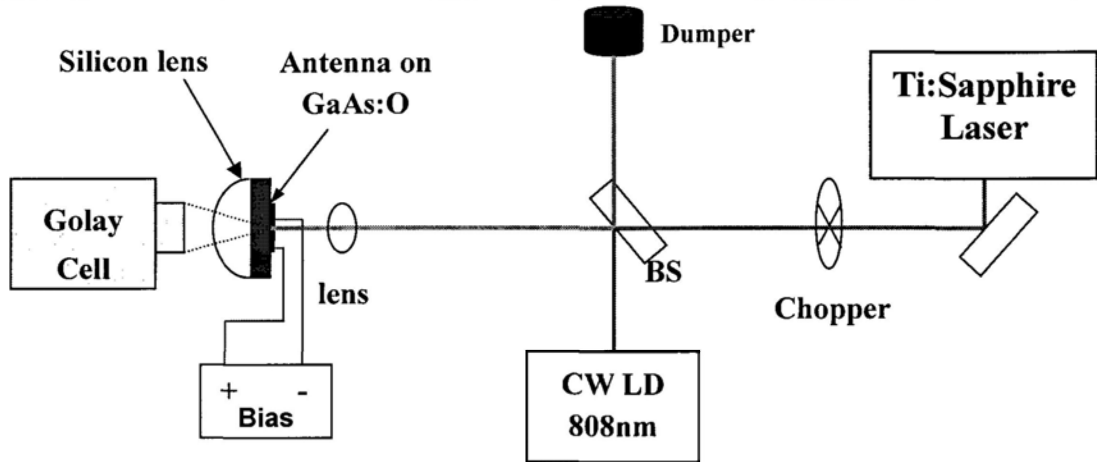

Figure4.6: Schematic of experimental setup for studying pulsed THz wave generation efficiency as a function of CW background illumination

4.4 Results and Discussion

Now, with those experimental systems introduced above, we can test the THz generation properties of GaAs:O based PC devices, and comparing them with other material based devices, for example LTG GaAs and GaAs:As.

4.4.1 Photocurrent and THz power

As discussed in Chapter 4.2, the THz power is proportional to the derivative of photocurrent. For a giving fs laser pumping source, a larger average photocurrent normally means a larger THz power one can achieve. So, to investigate the THz generation performance of our GaAs:O samples, the first work is to get the photocurrent relationship with bias or pumping power, and then to see how large THz power we can achieve.

At first, we tested the device which fabricated on GaAs:Oe14 material (SI GaAs(110) substrate, O^+ ion multi-implanted with 500keV/6×10^{13}cm^{-2}+800keV /6×10^{13}cm^{-2}+1200keV/$1\times\mathbf{10^{14}}$cm.), which was annealed under 550℃. The device structure is dipole, and the separation between the centers of these two striplines (D_s) is 195μm. This device is named as "dipole_1", the other details of this device can be found in Table 3.3.

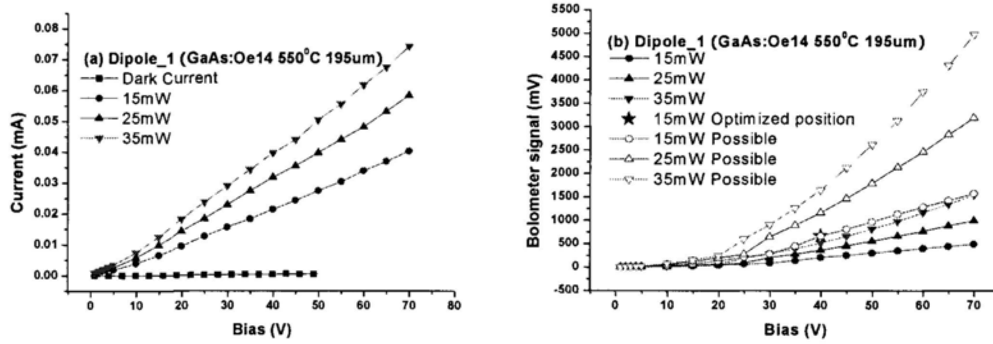

Figure 4.7: I-V curve and Power-Bias curve of Dipole_1 (GaAs:Oe14 550℃, 195μm)

Figure 4.7(a) shows the I-V curve of device dipole_1. Its dark current is very small, because the dark resistance of this device is as high as 16.13MΩ. A smaller dark current is always what we desire, as it corresponds to a possible higher SNR (signal to noise ratio) value. After injecting fs pumping light, the current increases dramatically, which means the device has a good optical response, or to say, the material is in a good semi-insulating state. The photocurrent (chopped) is about 0.075mA when the pump power and the dc bias are 35mW and 70V respectively.

Under **Gain=200 channel** of Bolometer detector, the power of THz wave (in Pulse mode) is about 0.31V when the pump power and the dc bias are 35mW and 70V respectively. After optimizing the position of Si Bolometer detector and Parabolic mirror to collect most of power into Bolometer detector, the total power in that condition should be about 1V. (A 0.133V output power of THz wave for the condition of 15mW pump power and 40V bias after optimization, comparing the 0.0414V output power under the same condition before optimization. In other testing conditions, the ratio should be the same.).

As in this thesis the most of THz power data were measured with Gain=1000 channel, so the data in Figure 4.7(b) is also adjusted by simple mathematic calculation (multiply 5) to get the same order.

Note: without additional mentioning, the data in subsequent figures represent measurements with bolometer detector Gain=1000.

As mentioned before, after carefully calibrated by using a blackbody source, we know the relationship between the output data of Si Bolometer and the common THz power in Watt unit, that is 1mV≅0.02μW under Gain=1000 for this Si bolometer. Then from the Figure 4.7(b), we can know the possible power of this device should be around **100 μW** . If considering the losses during the measurement, such as chopper loss, propagation loss, the output power of THz-pulse wave should be even higher. This means the material of oxygen ion implanted GaAs is a good material selection for generating high power THz wave.

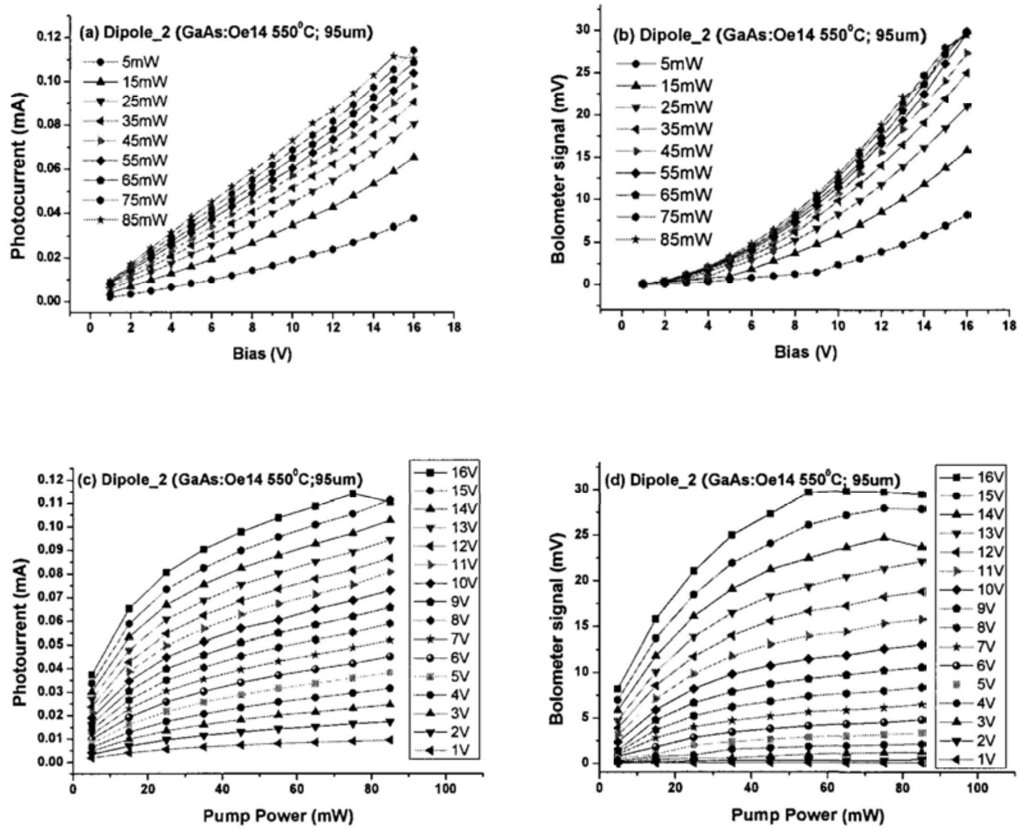

Figure4.8: Electrical properties and THz generation performance of Dipole_2 (GaAs:Oe14 550℃, 95μm). (a) I-V curve; (b) THz power vs. Bias voltage; (c) Current vs. pump power; (d) THz power vs. pump power.

To study the I-V curve and Power-Bias curve under different pumping power in detail, now, we switch to the next device, **dipole_2** (SI GaAs(110) substrate, O^+ multi-implanted with 500keV/6×10^{13}cm^{-2}+800keV/6×10^{13}cm^{-2}+1200keV/1×10^{14}cm, 550℃ annealing. D_s=95μm), which is fabricated on the same substrate material, but

only different on the dipole antenna scale.

From Figure 4.8(a), one can easily find the dark current is also very low like dipole_1. Its dark resistance is around 11.11MΩ. The photocurrent increases with bias by little nonlinear trends under low pump power, and slowly come to linear curve profile with the pump power increasing. This suggests that under lower pump power condition, the electric field is the dominate factor, even little increasing in electric field will lead to the current increasing dramatically. With the pump power increasing, as discussed in the Chapter4.2, the space charge field also increases quickly, which will decrease the local field in photogap area and slow down the current increasing with bias voltage. If the increase speed of space charge field is higher than bias voltage, the I-V curve should be more like inversely nonlinear curve profile compare with the situation under lower pump power in Figure 4.8(a). The relationship between the pump power and current can be easily figured out from Figure 4.8(c). Under a giving bias voltage, the photocurrent slowly closes to its saturation level with the increasing of pumping power. The reason is the decrease of local field in photogap area with the space charge field increasing (screening effect). As we know, the THz power is proportional to the derivative of the photocurrent, so from the saturation behavior of photocurrent we can easily suppose the THz power will also be saturated under higher pump power. The curve of THz power vs. pump power in Figure 4.8(d) gives us the evidence of THz power saturation. The THz power versus Bias voltage curve is also showed in Figure 4.8(b) for reference. In this figure view, the pump power saturation phenomenon can also be figured out from the congregated data points on the top.

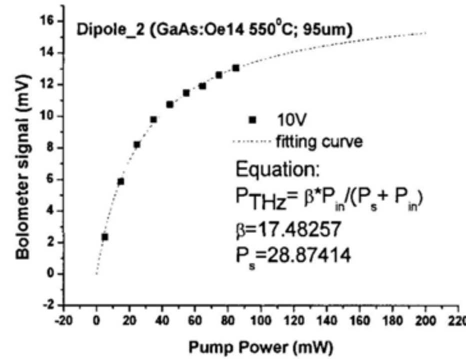

Figure 4.9: Saturation behavior of dipole_2 under 10V bias.

Using calculation equation like Eq.(4.21) or Eq.(4.32) to fit the curve "10V" in Figure 4.8(d), we can get the calculate data in that kind of model, **$\beta \approx$ 17.48257 and $P_s \approx$ 28.87414**. The fitting result is showed in Figure 4.9. The THz signal looks to be limited in the range of 14.5mV to 17.5mV, when pumping power is higher than 120mW, which is only quarter to half of the total power that can be achieved by common ultrafast laser sources. This means we only utilized part of capability of current fs-laser source, because of the power saturation of device. To circumvent this, one choice is to use temporally longer optical excitation pulses to generate narrowband THz signal, as they have lower fluencies intensity for the same total average power. The increasing temporal duration of the pulses, when appropriately shaped[93-96], does not decrease the amount of THz emission in the desired spectral range, but it really does diminish the saturation effects in the photoconductive materials[87].

Above, GaAs:Oe14 based devices have been tested. Then, how about the THz generation performance of device fabricated on other kind of substrate materials? Is it similar to the results above, or it is very different with those? Let's study the third device (dipole_5) which has the same dipole antenna scale (D_s=95μm) as dipole_2, but it is fabricated on GaAs:Oe13 material (SI GaAs(110) substrate, O^+ multi-implanted with 500keV/2.5×10^{13}cm^{-2}+800keV/2.5×10^{13}cm^{-2}+1200keV

$/4\times10^{13}$cm, 500℃ annealing). Figure 4.10 shows the I-V curve and Power-Bias curve of this device. Its I-V curve is very similar to dipole_2, which also has a very low dark current. The behavior of dipole_5 is almost the same as dipole_2 in small voltage range (<16V). That means these two substrate materials have similar electrical properties and THz power generation performance.

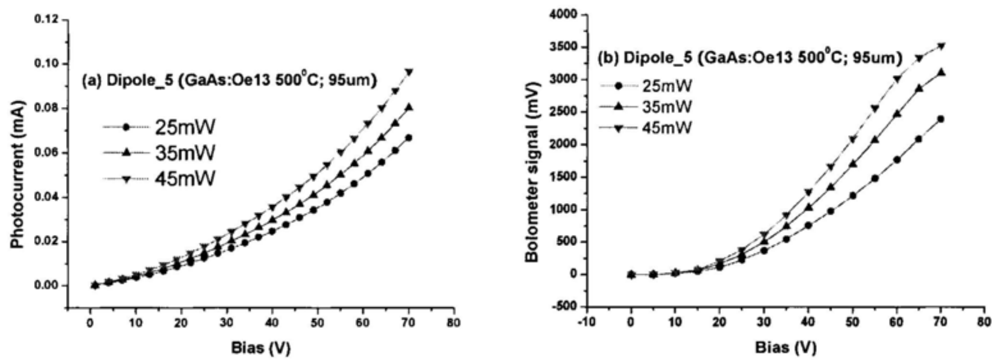

Figure4.10: I-V curve and Power-Bias curve of Dipole_5 (GaAs:Oe13 500℃, 95μm)

In this experiment, we also test the device under higher bias voltage, extending to 70V level (see Figure 4.10(b)). Unlike dipole_1, the THz power looks starting to saturate under DC bias higher than 60V with relative high pump power level (>35mW), although the photocurrent is still increasing without any obvious saturation behavior happened under the same conditions (see Figure 4.10(a)). Why the THz output power doesn't increase with current linearly in this testing condition range? There are some possible reasons which maybe cause this kind of result. One is some of THz power loss in the substrate which device fabricated on, the high density of free carriers in such device absorb part of power of THz wave. It is more obvious under high current level. The second possible reason maybe is the increased photocurrent is not all used to generate THz wave for some unclear reason (factor) under such relative high current level. As we know, there exists a long stay current phenomenon in some semiconductor material[97]. When the pump power and bias reach the threshold, the current will increase dramatically and stay at that level for a relative long time, even the pump power was little decreased during that period. Then the change of current will not follow well with pump power varying, which at

the end should lead to that the THz Power generation can not increase like those under the normal situation.

The devices like dipole_6 and dipole_7 (which fabricated on the same type substrate material as dipole_3), and dipole_8 (which fabricated on LTG GaAs substrate) were also tested for THz power generation performance. The separation distance between two stripline (D_s) of Dipole_6 is 45μm, other structure parameters of this device are similar to Dipole_1 to Dipole_5. Unlike those devices, the dipole_7 and dipole_8 have most different structure parameters (L_s=30μm, W_s=10μm, W_a=5μm, and d_{gap}=5μm). Other details of devices can be obtained from Table 3.3.

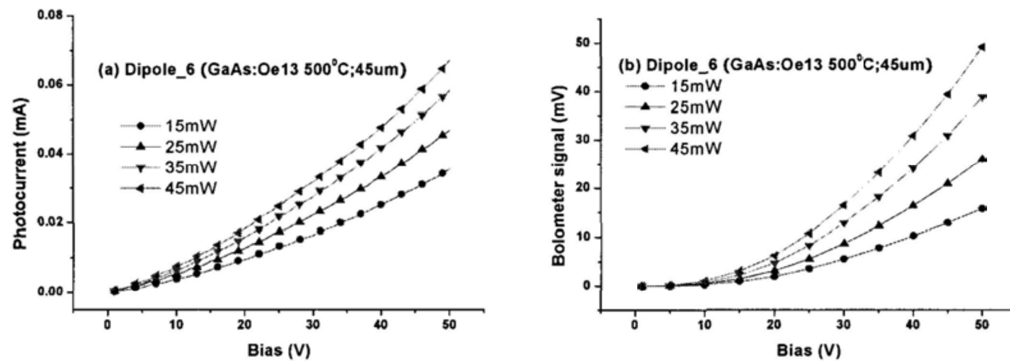

Figure4.11: I-V curve and Power-Bias curve of Dipole_6 (GaAs:Oe13 500℃, 45μm)

Figure 4.11 to Figure 4.13 shows the electrical properties and THz power generation performance of device for dipole_6, dipole_7 and dipole_8 respectively. From these figures, one can find some phenomenon like following.

For the dipole_6 and dipole_7, as they are fabricated on the same substrate material, the behavior of I-V curve and THz power versus Bias curve are very similar to dipole_5 under relative lower pump power and bias voltage. The only big difference is their THz power is around one or two orders lower than dipole_5. Their intensity sequence are dipole_5>dipole_6>dipole_7, just like the sequence of their structure scale. This relationship also can be found between dipole_1 and dipole_2 on the same substrate material, the larger scale device always potentially can generate relative higher power. The reason maybe is that the resonance

frequency is relative lower for its larger scale device. Another possible reason should be the enhancement of photocurrent caused by the different drift velocity between electron and hole in such electrical bias field.

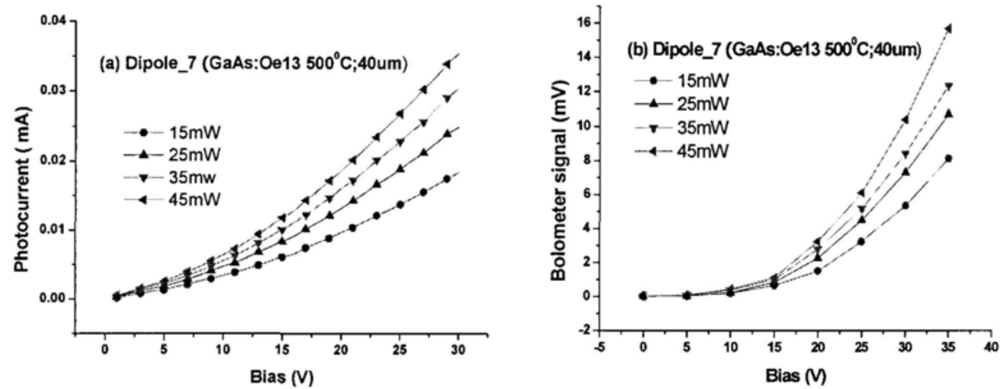

Figure4.12: I-V curve and Power-Bias curve of Dipole_7 (GaAs:Oe13 500℃, 40μm)

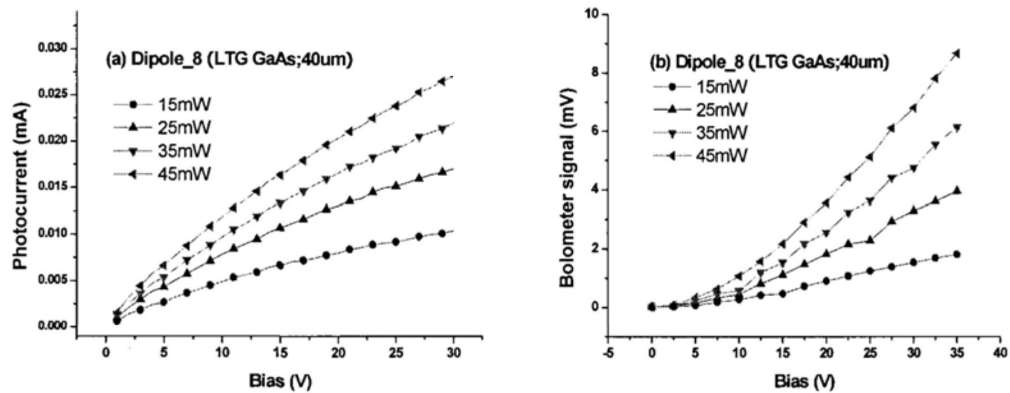

Figure4.13: I-V curve and Power-Bias curve of Dipole_8 (LTG GaAs, 40μm)

As fabricated on different substrate material (LTG GaAs) and with different structure parameters, dipole_8 have very different behavior on these curves. The photocurrents of dipole_8 in Figure 4.13(a) don't increase like other figures showed above. The dark current of dipole_8 is the lowest one among these devices, because LTG GaAs material normally has a very big resistivity [98]. With light injection, the photocurrent increase slowly comparing with those devices fabricated on GaAs:O materials, and its increasing speed lowers down obviously under bias voltage >16v. As discussed above, when the increasing speed of space charge field is beyond that of applied bias field (which cause the increasing speed of local field slower down,

$E_{loc}=E_b-E_{sc}$), the I-V curve will bend down which is different with those in Figure 4.12(a), although they have the same antenna structure. This exhibits the difference characteristics of materials.

But, it is interesting that the curve of THz power vs. Bias doesn't bend down like I-V curve under those testing conditions. It looks the LTG GaAs material maybe has relative higher photocurrent utilization efficiency in such testing situation compare with GaAs:O materials.

To compare the pump power or DC bias field dependence behaviors of different substrate materials under the same testing condition, some data were picked out from the figures above and re-plotted in Figure 4.14. Figure 4.14(a) tells us a story about THz power increase with pump power. Under 30 V bias, dipole_5 (GaAs:Oe13 500 ℃, 95 μm) has the highest output THz power among these devices, and dipole_8 (LTG GaAs,40μm) has the lowest output THz power. For the same antenna structure, dipole_7 (GaAs:Oe13 500 ℃, 40 μm) has higher output power of THz wave than dipole_8, but smaller power increasing rate when the pumping power increases. And from this figure, comparing the upper two curves with those lower three, one can also easily get idea on the potential of large scale device in THz power generation area. Figure 4.14(b) shows us a bias dependence view of THz generation under **25 mW pump power** condition. From it, one can find the THz power increase dramatically with the bias for dipole_1, dipole_2 and dipole_5, which are large scale devices, comparing with the others in figure. One can also find the dipole_7 has larger power increasing rate than dipole_8 (which having the same device structure) and generates higher THz power under higher bias field.

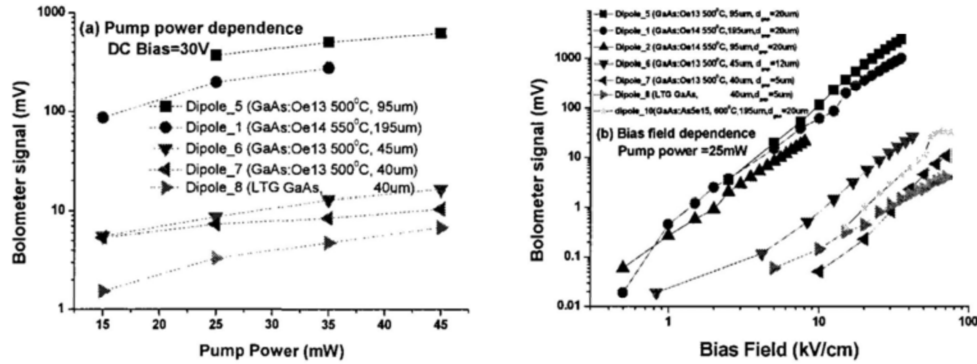

Figure4.14: Comparison of THz power generation performance of different devices. (a) Pump power dependence; (b) Bias dependence.

For detailed observation on Figure 4.14(b), firstly, one can find that a photoconductive device with a smaller gap distance (d_{gap}) generates less THz power when biased at the same electric field strength, as evidenced by the reduction of power from Dipole_5, Dipole_1 and Dipole_2 (all having 20 μm gap distance) to Dipole_6 (12μm) and then to Dipole_7 and Dipole_8 (both at 5μm). One possible explanation of the results observed above may be related to the existence of a region of high field strengths around the anode within the gap region of PC device which will cause an enhancement of THz waves generated [39, 99]. In Dipole_7 and Dipole_8, the size of laser spot (diameter around 5μm for all case) is similar to the entire gap and the region of high field strength can only affect a small part of the excited area. As the gap length increases in Dipole_6 and more so in Dipole_1, Dipole_2 and Dipole_5, the whole photo-excited area will overlap more and more with the high field region because the signal was optimized by moving the beam relative to the gap region until the maximum signal was obtained, thus generating an increasing amount of THz waves.

The second observation is on the results of Dipole_7 and Dipole_8, which have the same device structure but different materials (GaAs:Oe13 versus LTG GaAs respectively), GaAs:O material outperforms LTG GaAs at high field strength in terms of the emitted THz power. We do not understand very well about this difference as it stands and a more comprehensive research into the material

properties of these two materials is necessary to explain it. Some preliminary investigations were taken under CW generation mode. The detail will be discussed in Chapter 5.

The third observation in Figure 4.14(b) shows that the GaAs:O:e13 device (Diople_5) emits more THz power than an identical device made of GaAs:Oe14 (Dipole_2), while the device Dipole_1 with structure T_D1 yields a higher power than Dipole_2 of the same material but with a different structure T_D2. The former result can be explained by the better crystalline quality of the Low-Dose material (Oe13) over that of the High-Dose material (Oe14) so that the quantum efficiency is higher in the Low-Dose material (Oe13). The latter result is a little hard to understand, although one can speculate that the frequency response (lower resonant frequency) of the dipole antenna in T_D1 matches better with the broadband THz wave generated by the pulsed photocurrent (which relates to the material response limited by the carrier lifetime), which therefore produces a larger emitted power. The spectral response of these of the dipole structures will be discussed in a later section.

A fourth observation is that at the maximum biasing field tested, the emitted power of these six devices (except dipole_10) still has not shown any saturation, which means that even higher power levels can be obtained by merely increasing the biasing field and the fact that this had not been undertaken by us was only because we did not want to sacrifice the devices prematurely. Finally, the photoconductive switch Dipole_5 emits a THz power as high as 48 μW when biased at 70 V and pumped by a laser beam of 25 mW. This value is even higher than that reported in Ref.[100], although the corresponding optical-to-THz conversion efficiency is only ~0.2%, which is about 60% lower than that achieved in the same reference. As just mentioned above, the THz power, we believe, can still be raised had we further increased the applied bias or the laser pump power. In order to assess the effect of increasing the applied bias, we selected device Dipole_6 for the power saturation measurement because its gap is neither too small nor too large. Figure

4.15 shows the peak power of THz waves measured from TDS experimental system. These data are taken under 55mW pump power condition. From Figure 4.15, one can find the peak THz power of dipole_6 increases with the bias field until it reaches its saturation level around 230V, for the reason of effective local field lowering down. The device looks still work well under 270 V (225 kV/cm, 12 μm gap), and haven't reached its breakdown voltage yet.

Supposing the electric field strength at the saturation of emitted power is 200 kV/cm, it still far exceeds the maximum value actually employed in the measurements (40 kV/cm) shown in Figure 4.14(b). The power ratio between these two biasing electric fields is about 3:1 in Figure 4.15. Hence, one may expect that the absolute THz power at saturation for the 6 devices tested may be roughly 3 times their highest values shown in Figure 4.14(b), implying that **~150 μW** of output power is conceivable from Dipole_5 if it could be biased at 400 V. Considering that breakdown may commence before the bias can reach 400 V in D3, a reference to Figure 4.15 indicates that even at a bias of 240 V (120 kV/cm), which is very likely without causing breakdown, Dipole_5 may still be able to emit ~100μW of THz power while keeping the pump laser power at 25mW. It is worth to note that this high power level is achieved without any of the following optimization designs: a material structure which enables complete absorption of the incident laser power, an anti-reflection coating on the top surface of the device, an efficient heat removal scheme, or an optimized antenna electrode design which matches best with the THz wave generated. Consequently, if one can implement all the above design considerations, THz power on the order of **200 μW** should not be too difficult to obtain from a photoconductive switch fabricated on GaAs:O materials.

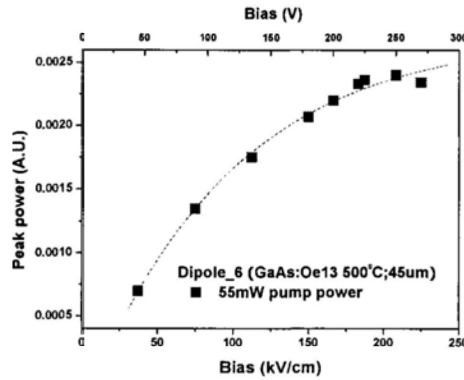

Figure4.15: Peak power vs. Bias curve of Dipole_6 (GaAs:Oe13 500℃, 45μm) measured from TDS

From Figure 4.14 and Figure 4.15, the testing results of dipole_6 suggest us that the GaAs:Oe13 material with 500 ℃ annealing is a very good selection of substrate material for PC antenna device fabrication. It also has relative high breakdown voltage (field), higher than 225 kV/cm. Although it looks haven't reach to the level of LTG GaAs material around 320 kV/cm (160 V for 5 μm gap[51]), the advantages of this kind of material (GaAs:O) are still obvious. For example, it could potentially generate higher output power of THz wave than LTG GaAs material under the same testing condition, as Figure 4.14 shows.

At last, the output THz power of dipole_10 which fabricated on GaAs:As substrate(GaAs:As, 50keV/5×10^{15}+100keV/5×10^{15}+200keV/5×10^{15}, 600℃ furnace annealing for 30min, D_s =195 μm) is also showed in Figure 4.14(b). Its THz output power is lower than that of GaAs:O based device (dipole_1) which has the same antenna scale as it. And some bias-dependent saturation behavior is appeared at relative higher bias field in GaAs:As based device.

So, from these comparisons, GaAs:O material has some advantages (high power and high saturation level) in THz power generation area, compared with GaAs:As or LTG GaAs materials.

Note: Maybe someone will question like "As the breakdown field of air is around 30kV/cm, how can our device (dipole_6) be tested under a high bias field (>100kV/cm) without any dielectric deposition process during device fabrication?"

At first, we should realize that the value 30kV/cm is measured in air by two separated metal rods (normally the end of rod is angled). Its testing condition is very different from the PC antenna case, where that most of the bias field was added on the substrate (GaAs:O). There should be several reasons could help the device (Dipole_6) to withstand higher bias field than 30kV/cm. 1).The rectangular shape of metal terminals (electrode shape, see Figure 3.1), will sustain higher breakdown threshold than rod terminals [101]. 2). The good quality of metal surface grown by E-beam deposition, few has defects or burrs to accumulate charges. 3.) The existence of a substrate disturbs the field lines between the electrodes. So that the actual field in air is smaller than that when the substrate is not present but otherwise under the same condition.

Many papers, whose devices were without dielectric deposition layer, also reported a breakdown field higher than 30kV/cm. (GaAs >200kV/cm [102], GaAs:As^+ >60kV/cm [33], and LTG GaAs >100kV/cm-360kV/cm [103]. So, the value 30kV/cm is not an absolute limit for those devices without dielectric cover layer. So, the real breakdown field for a device should be discussed case by case and to be considered during testing

Certainly, the dielectric deposition layer (SiO_2 or Si_3N_4) on the top of device will diminish the effect of air and other environmental contamination, and mechanical damage. With such a kind of layer, the breakdown field could be even higher. By the way, the dielectric layer can also act as an anti-reflection coating layer, which can enhance the efficiency of pumping light for the device [26].

4.4.2 THz spectrum

The THz spectrum is another very important factor for THz PC devices. Although the bandwidth of PC antenna is mainly limited by the laser pulse width (>10 fs) [74], it is still affected by the characteristics of substrate material, for example carrier lifetime and carrier momentum relaxation time. With a giving fs laser source, the

different performance of spectrum in THz range for those devices having the same antenna structure will mainly represent the different characteristics of substrate material. So, in this part, we used two spectrum measurement methods (FTIR and TDS) to get spectrum information of those devices, which we discussed before.

At first, we select the FTIR method (introduced in Chapter 4.3.2) to obtain information of spectrum in THz range, for its system setup only requiring little change on the power measurement system (which has been introduced in Chapter 4.3.1).

Figure 4.16 shows the THz spectrum of some devices. The bandwidth of spectrum of dipole_1 (GaAs:Oe14 550℃;195 μm) is around 0.6THz, under 30mW pump power and 70V bias voltage testing condition. The spectrum bandwidth of dipole_3 (GaAs:Oe14 550℃;45 μm) is little broader than dipole_1. Unlike dipole_1 and dipole_3, It looks the device dipole_6 (GaAs:Oe13 500℃; 45 μm) has narrower bandwidth comparing with dipole_5 (GaAs:Oe13 500℃; 95 μm), which are both fabricated on GaAs:Oe13 substrate with 500℃ annealing. For reference, the spectrum of dipole_2 (GaAs:Oe14 550℃;95 μm) is also showed in Figure 4.16(e). It has a resonance peak at 0.12 THz. Dipole_5 has the broadest spectrum among these five devices in Figure 4.16, around 0.75 THz, under 35 mW pump power and 70 V bias condition.

From Figure 4.16(f), one can see clearly the resonance frequency in linear scale. The resonance frequency of these devices are most in the range of 0.1 to 0.4, lower than the calculated data from Eq.(3.1) in Chapter 3. For larger scale device like dipole_5 and dipole_1 are more close to the calculated data 0.461 THz and 0.255THz respectively. But the small scale devices like dipole_3, dipole_6 and dipole_2, the resonance frequencies have a big difference with the calculated data.

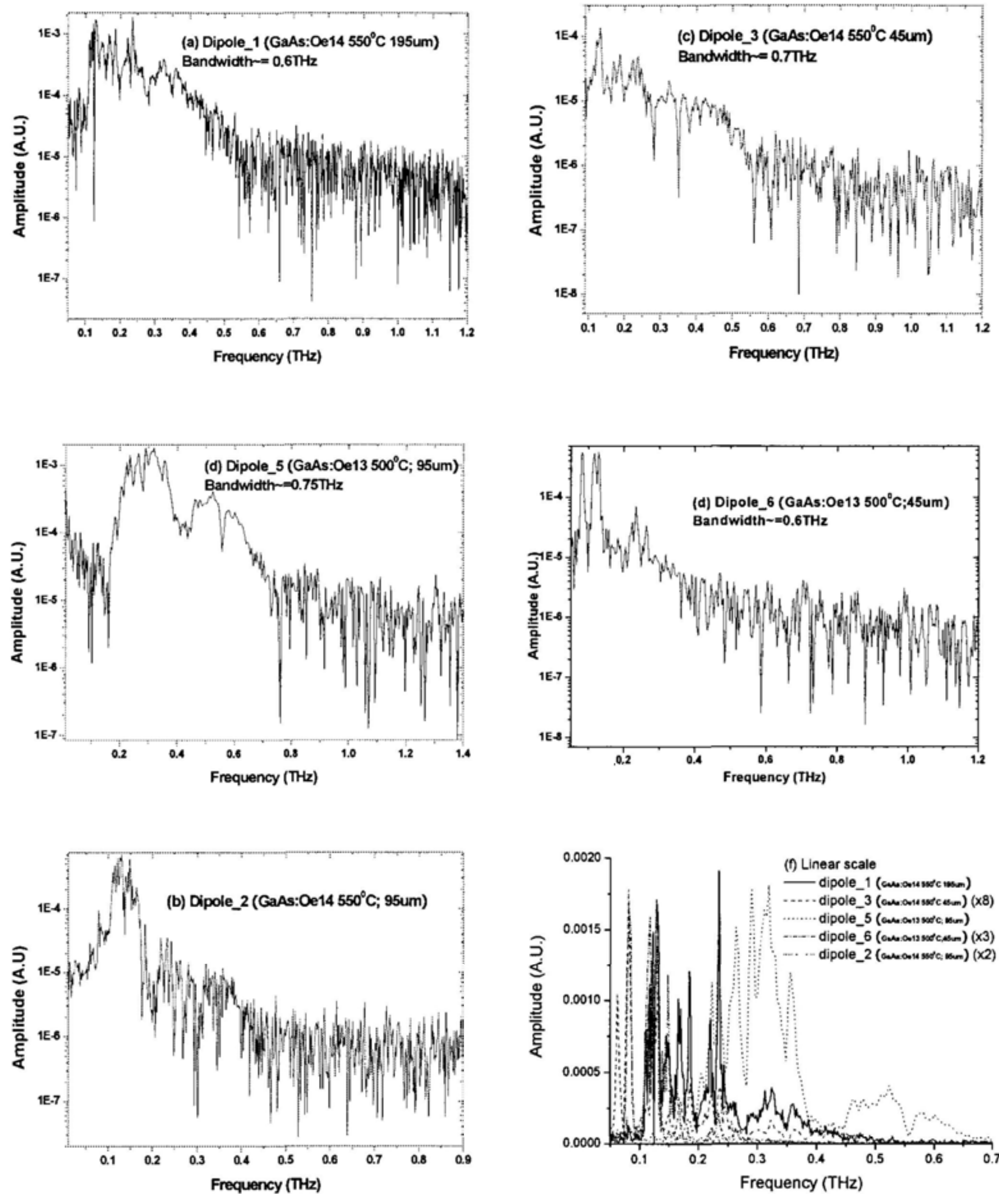

Figure4.16: THz spectra of devices measured by FTIR method. (a) Dipole_1, (b)Dipole_3, (c)Dipole_5, (d)Dipole_6, (e)Dipole_2. (f)Spectra of devices in linear scale.

Is this the reason of the measurement method? To check this question, we also tried to measure the devices with TDS method. Using the TDS method introduced in Chapter 4.3.3, the terahertz signal waveforms of dipole_1_2 (GaAs:O e14 550℃, 195um) are measured and plotted in Figure 4.17(a). The FWHM (Full Width of Half Maximum) of the main pulse of dipole_1_2 under 100V bias and 55mW pump power is around 1.8 ps, which lead to the spectrum obtained from Fourier transform calculation does not extend to very high frequency range (Figure 4.17(b)), but it still

reach to around 1.4 THz. For reference, the FTIR spectrum curve of the same kind device (dipole_1) is also showed in the Figure 4.17(b). Comparing these two curves in the figure, we can find that the TDS method can give more information in higher frequency range, because it has higher sensitivity (SNR value) comparing with the FTIR method. But it is not good at frequencies detailed plotting compared with the FTIR method, as one can see from the detail in the range of 0.1 to 0.4 THz.

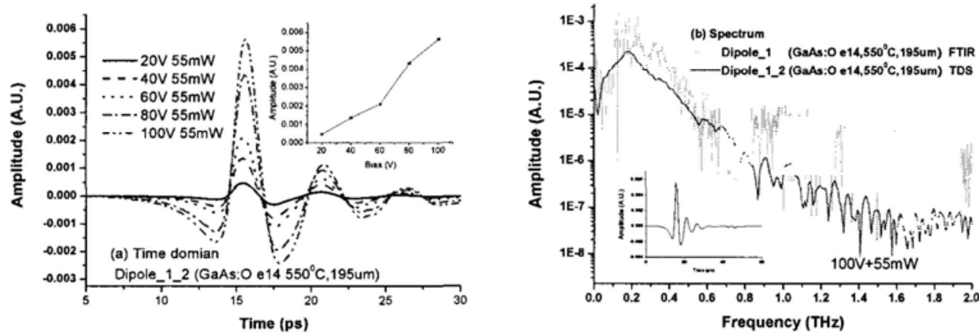

Figure4.17: TDS measurement of dipole_1_2 (GaAs:O e14 550℃,195μm). (a) THz signal waveforms under different DC bias. Insert figure: curve of peak power versus bias. (b)THz spectrum of dipole_1_2 (under 100V bias, 55mW pump power). The light gray curve is from dipole_1 measured by FTIR method. Insert window: waveform of THz signal in time domain for dipole_1_2.

The insert figure in Figure 4.17(a) gives us a view of peak power of THz signal versus DC bias. It shows the device is still working in the normal range, and has not reach its field saturation point like Figure 4.15 shows.

If we take the value of amplitude of THz signal 10 times higher than the noise level as the point of the end of bandwidth of device for TDS method, then from the Figure 4.17, the bandwidth of dipole_1_2 is around 0.8 THz. If we look the start point of data close to the noise level as the end point of bandwidth, then the bandwidth should be close to 1.4 THz. In this work, we prefer the 10 times value point to be the end of bandwidth point, only for TDS measured spectrum.

And one can also get the measured bandwidth from FTIR method. The bandwidth of the dipole_1 is around 0.6 THz. Other details are showed in Table 4.1. The resonance frequency of these two devices, which having the same dipole

structure and size, are 0.18 THz and 0.185 THz respectively.

As the resonance frequency is about one third smaller than the calculated data (by Eq.(3.1), see Table 3.1) from both FTIR and TDS measurement method, it suggests the result is mainly not only determined by dipole structure, but it maybe also has very tight relationship with the substrate material properties, which normally looked as the key factor for bandwidth but not resonance frequency. If thinking things along this direction, the problem will be more complex. So we are trying to explain this phenomenon in anther point of view.

As the parameter ε_e used for Eq.(3.1) is calculated from $\varepsilon_e = (1+\varepsilon_d)/2$, an adjusted equation considering the THz signal is just generated at the interface of air and substrate material, the value 1 in that equation is the permittivity of air. If the THz signal is not just generated in the interface, but more part in the air or more part in the material, then the parameter ε_e should be a value between 1 and ε_d (normally it should in the range from $(1+\varepsilon_d)/2$ to ε_d, as the electrical field is in the substrate material, but not in the air).

If submitting the maximum value, $\varepsilon_e = \varepsilon_d = 13.08$ into the Eq.(3.1) for structure T_D1 (D_s=195μm) , then one can get the resonance frequency is around **0.18732 THz**, which is very close to the results of measurement from FTIR or TDS.

So, one possible explanation is, in this case, the THz wave is generated more deep in the substrate material, but not the air-material interface like the equation $\varepsilon_e = (1+\varepsilon_d)/2$ considered.

We also tried to test some device which also has the same dipole structure (T_D1) as dipole_1_2, but fabricated on difference substrate material. Figure 4.18 shows the THz spectrum of dipole_10 (GaAs:As5e15,600℃,195μm). And the spectrum from FTIR method is also plotted for reference with light gray color. Unlike GaAs:Oe14 material which annealed under 550℃, this GaAs:As5e15 (annealed under 600 ℃) material looks it can support a broader bandwidth. The

bandwidth is around 1 THz both from FTIR and TDS measurement methods. An interesting thing is the resonance frequency is not close, one is around 0.215 THz and the other is around 0.155 THz, but the average value is still very close to the calculated value above, around **0.185 THz**. So one could speculate, in these testing cases, the THz signal is more like generated in the deep of substrate material comparing to the air-material interface. And the characteristics of material determine the bandwidth of devices.

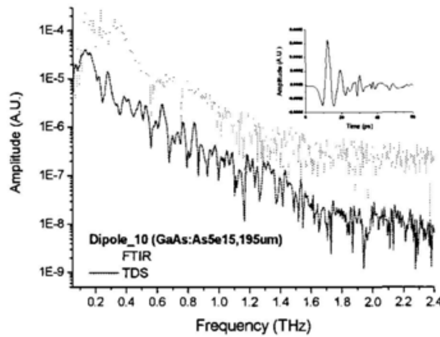

Figure4.18: Spectra of dipole_10 (GaAs: As5e15,600℃,195μm). Insert: waveform of THz signal in time domain.

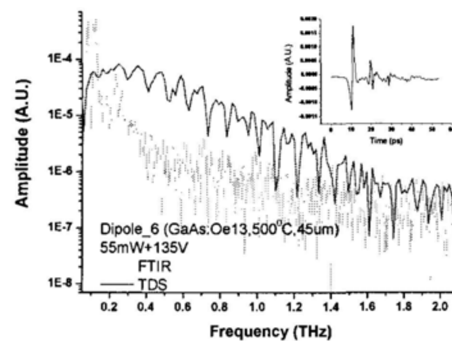

Figure4.19: Spectra of dipole_6 (GaAs:O e[13] 500℃,45μm). Insert: waveform of THz signal in time domain.

The TDS measurement results of other devices are showed in Figure 4.19 and Figure 4.20. Under 55mW pump power and 135V bias voltage testing condition, the bandwidth of dipole_6 is about 1.3 THz, and the resonance frequency is at about 0.25 THz. The Figure 4.20(a) shows the spectrum of dipole_7 has a bandwidth little broader than dipole_6, it is around **1.4 THz**. The resonance frequency of dipole_7 is also close to 0.25 THz. Its testing condition is 65mW pump power and 25V bias voltage.

The Figure 4.20(b) shows the broadest spectrum of these devices tested in this work. LTG GaAs material gives us a relative broader spectrum, but is still only about **1.6 THz**. The reason should be the dipole antenna structures intrinsically have a narrower bandwidth comparing to those broadband antenna structures, like bow-tie or spiral. As we know, the dipole antenna structure has a resonance frequency, which takes most power of THz signal into that range (or to say,

enhances the frequency components in that range) and limit the whole bandwidth of device. From Figure 4.20(b), one can find the resonance frequency of dipole_8 (LTG GaAs, 40μm) is around 0.26 THz.

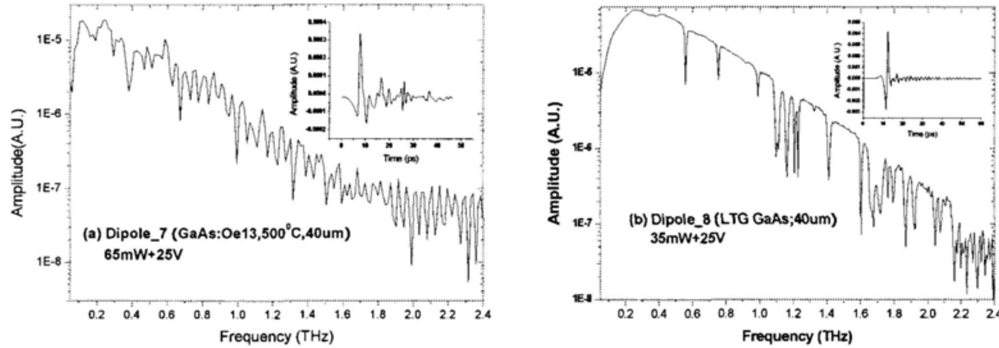

Figure4.20: Spectra of dipole_7 (GaAs:O e13 500℃,40μm) and dipole_8 (LTG GaAs,40μm). Insert windows in (a) and (b): waveform of THz signal in time domain of dipole_7 and dipole 8, respectively.

From the insert figures of Figure 4.17 to Figure 4.20, one can find some resonance pulses after the main pulse peak. The main reason should be the feedback of THz signal at the end of striplines (contact pads of dipole antenna), because the striplines are not long enough in this work. It is only 2mm, comparing with 6mm-10mm in some papers.

Table4.1 shows all the spectrum information of these devices, collected from the figures showed above. From this table, one can easily find the resonance frequency of devices increasing with the decrease of antennas length from T_D1 to T_D4. And the material (GaAs:Oe14, 550℃ annealing) has the narrowest bandwidth among these materials. LTG GaAs material has the broadest bandwidth. The material (GaAs:Oe13, 500℃ annealing) and (GaAs:As5e15, 600℃ annealing) should have similar bandwidth, and their bandwidth are broader than GaAs:Oe14 material, but little narrower than LTG GaAs material. As the carrier lifetime is inverse proportional to THz bandwidth, so, it means these materials should have a relationship of carrier lifetime like:

LTG GaAs<GaAs:Oe13 ≤GaAs:As5e15<GaAs:Oe14.

Material	Structure	Resonance frequency	Bandwidth
GaAs:Oe14, 550℃ Annealing	T_D1 (D_s=195μm,d_{gap}=20μm)	~0.18THz (FTIR) ~0.185THz(TDS)	~0.6THz (FTIR) ~0.8THz (TDS)
GaAs:As5e15 600℃ Annealing	T_D1 (D_s=195μm,d_{gap}=20μm)	~0.215THz (FTIR) ~0.155THz (TDS)	~1THz (FTIR) ~1THz (TDS)
GaAs:Oe14, 550℃ Annealing	T_D2 (D_s=95μm,d_{gap}=20μm)	~0.13THz (FTIR)	~0.4THz (FTIR)
GaAs:Oe13 500℃ Annealing	T_D2 (D_s=95μm,d_{gap}=20μm)	~0.33THz(FTIR)	~0.76THz (FTIR)
GaAs:Oe14 550℃ Annealing	T_D3 (D_s=45μm,d_{gap}=12μm)	~0.12THz(FTIR)	~0.7THz (FTIR)
GaAs:Oe13 500℃ Annealing	T_D3 (D_s=45μm,d_{gap}=12μm)	~0.11THz (FTIR) ~0.25THz(TDS)	~0.8THz (FTIR) ~1.3THz (TDS)
GaAs:Oe13 500℃ Annealing	T_D4 (D_s=40μm,d_{gap}=5μm)	~0.25THz (TDS)	~1.4THz (TDS)
LTG GaAs	T_D4 (D_s=40μm,d_{gap}=5μm)	~0.26THz (TDS)	~1.6THz (TDS)

Table 4.1: Resonance frequency and bandwidth of devices measured by FTIR or TDS.

Maybe someone will question like "Is the LTG GaAs sample used in this work of good quality? Because in this work the spectrum of LTG GaAs material looks not broad enough as some papers described." or "Is this LTG GaAs material the one commonly used in THz research? It looks its bandwidth not broad enough." To answer these kind of questions, we should discuss some related factors at first.

Some papers show that one can generate THz wave with frequency bandwidth up to several THz (3~5THz [104]) from LTG GaAs materials. Some of them even can achieve up to several tens THz (30THz) [105]. If one reads those papers carefully, one can find two main differences exist between them and our work. One is the measurement system, the other is the device structure.

For measurement system, one can find in their system, they use an ultrashort pumping source one pulse width is narrower than ours. From the study of Zhisheng PIAO in 1999 [66], one can get some idea about the relationship between the pulse width of pumping source and the THz spectrum. Even for the same emitter, under

different fs laser sources, the spectra will be very different. The narrower pulse width of the laser source will help to generate a broader THz spectrum. So it is not strange that our spectrum is not broad as they are. In the measurement system, another important factor also can't be neglected. That is the detector used in the system. Compared with antenna detection using a LTG GaAs detector, the free space electro-optic sampling normally has a broader detection range [106]. This is another reason why our spectrum is not broad enough like others.

For device structure, the dipole antenna in our samples is more suitable for narrow band THz generation compared with bow-tie or spiral structure, for its resonance enhancement effect. The resonance behavior of dipole antenna limits its performance away from the resonance frequency. This is also an important factor that should be counted in when one considers its spectral performance.

Among these three factors discussed above, the pulse width of fs laser source is the most important factor, which will affect the spectrum dramatically.

Now, let us compare the performance of our LTG GaAs with other LTG GaAs samples. Papers like [51], [107] show that in LTG GaAs devices with carrier lifetime and dipole antenna structure similar to ours, their bandwidth of THz spectra are also similar to ours, which means our LTG GaAs are similar to theirs.

Of course, we can't guarantee our LTG GaAs sample is the best of such material. So the comparison between our GaAs:O material and our LTG GaAs sample is just to show that the GaAs:O is also as good material as common LTG GaAs material for THz generation. The comparison study of GaAs:N and LTG GaAs [108], shows that for different preparing conditions, the performance of GaAs:N samples will be very different. Some of them are better than LTG GaAs, some of them are not. Similarly, the LTG GaAs samples under different growth conditions will also have different performance compared with our GaAs:O samples. So if one wishes to do a comparison between the best of each material, he (she) should do more work upon the results discussed in this work, by fabricating the same device on the best sample of each material type, and testing them with the

same testing system.

4.4.3 Pulsed THz wave generation with a CW background illumination

As Figure 4.9 shows, the THz signal will be saturated under relative high pump fluency (power). This saturation behavior is attributed to the screening of bias-field which induced by the photo-induced carriers. Two main screening mechanisms should be accounted into this saturation phenomenon. One is "space-charge screening" which should not be neglected in a small gap PC emitter, which caused by the spatial separation of the photogenerated electron-hole pairs under the influence of the electric field. The other one is "radiate field screening", which caused by the back action of the THz field on the photocurrent. As we discussed in Chapter4.1, the intensity of the THz signal generated by PC devices is proportional to the effective local field in photogap, which driving the photocurrent to generate THz wave. Then, we can slightly adjust Eq.(4.4) to describe the effective local field more exactly:

$$E_{loc} = E_b - E_{sc} - E_a \text{ [87]} \tag{4.34}$$

Where, E_{sc} and E_a presents space-charge screening field and radiation screening field respectively. E_{sc} can be calculated from Eq.(4.4) and Eq.(4.5). E_a can be obtained from Eq.(4.27).

One method to study this bias-field screening is double-pump-pulse THz-emission spectroscopy [88]. From this kind of method, one can know more information of the screening effect, for example, which one is the main reason in certain case. In this work, we will not repeat this kind of experiment. Here, we are interested in the steady state screening effect caused by CW background illumination with the following aspects: 1).The change tends of THz power with the increasing intensity of CW illumination. 2).The maximum modulation ratio that could be obtained by CW illumination. 3).The tends of modulation ratio under different fs laser pumping condition (pump power). 4.) The relationship between the DC bias (or applied field) and the modulation ratio, and so on.

Figure4.21 The device (spiral antenna) for CW background illumination experiment.

As we are not focusing on the THz spectrum and the THz power, but the tendencies of the THz power change with CW background illumination, in this work we adopted the experimental setup like that shown in Figure 4.6. To minimize the effect of resonance frequency on THz power distribution from dipole antenna, we use some broadband antenna structure, like spiral antenna[26], to pursue the study work. To enhance the electrical field, in this experiment, we add some fingers (mixer) structure into the device structure as shown in Figure 4.21. Three 2μm×8μm fingers are loaded onto the photogap area of spiral antenna. The gap between each finger is 2μm. Other parameters of this kind of device can be found in Table 3.3. In this experimental setup (Figure 4.6), the CW laser diode is the normal 808nm high power laser diode, whose linewidth is around 3nm.

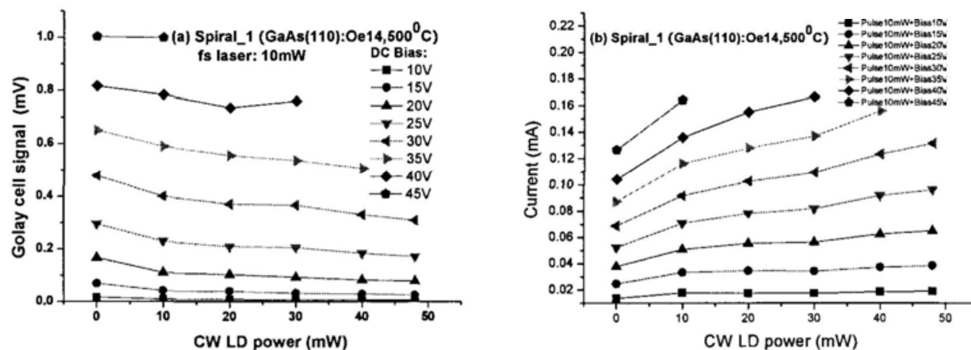

Figure4.22: THz power and photoinduced current under CW background illumination for device spiral_1 with 10mW fs laser pumping. (a) THz power vs. CW LD power; (b) Current vs. CW LD power.

Firstly, we try to answer some of those questions by testing the device spiral_1,

which is fabricated on the substrate material GaAs(110):Oe14 (a lower annealing temperature at 500℃ is selected). Figure 4.22 shows the measurement results of this device under different power illumination by CW laser diode. From Figure 4.22(a), one can easily find the decreasing tends with the CW LD power. The THz power generated by fs laser pumping is screened by CW background illumination, and it decreases with the increasing of CW LD power. Different DC bias voltage gives it different start pedestal, which because the THz power is proportional to the Bias voltage (applied electrical field). Figure 4.22(b) gives the information of the current change with the power increasing of CW laser diode. Under different DC bias voltage, the same CW LD power gives different contribution on current and at the end to the screening effect.

By dividing the THz power in Figure 4.22(a) by the THz power generated by fs laser pumping without any CW LD illumination under the same DC bias voltage, (the modulation rate, $P_{THz}/P_{THz,CW=0mW}$), and calculating the increasing of current by CW LD illumination under the same DC bias ($\Delta I=I_{current}-I_{current,CW=0mW}$), then we can plot the curve of THz modulation ratio versus photocurrent generated by CW LD illumination (ΔI) in Figure 4.23. From it, the relationship between the THz power modulation ratio and photocurrent generated by CW light is obvious. The more photocurrent generated by CW light will cause more THz power (which generated by fs laser pumping) to be screened. The maximum modulation ratio is around 65% (measured data 1:0.35 for without and with CW light), under the testing condition of 10mW fs laser pumping, 10V bias voltage and 48mW CW LD power. The modulation ratio is similar to the results of ref.[109]. From the curve, it looks the value of modulation ratio still could be larger and larger if the CW LD keep increasing. By increasing the DC bias voltage, the contribution of photocurrent on screening effect looks coming down, and go to a lower modulation level within 10% when the bias voltage higher than 40 V.

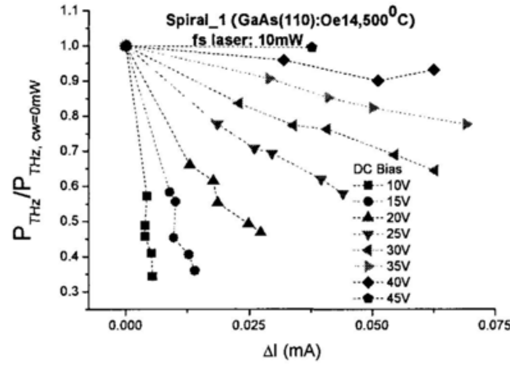

Figure4.23: The effect of CW LD background illumination on pulsed THz wave generation versus the photocurrent induced by the CW LD illumination

If trying to use another site to view, it maybe can give us more tips on the relationship between the screening effect and the CW LD power or DC bias. Figure 4.24 shows the curves of THz modulation ratio vs. CW LD power, or DC bias voltage. From them, the increasing tends of modulation ratio with the increasing of CW LD power and its decreasing tendency with the increasing of DC bias are both clear in the figures. The possible reasons will be discussed later.

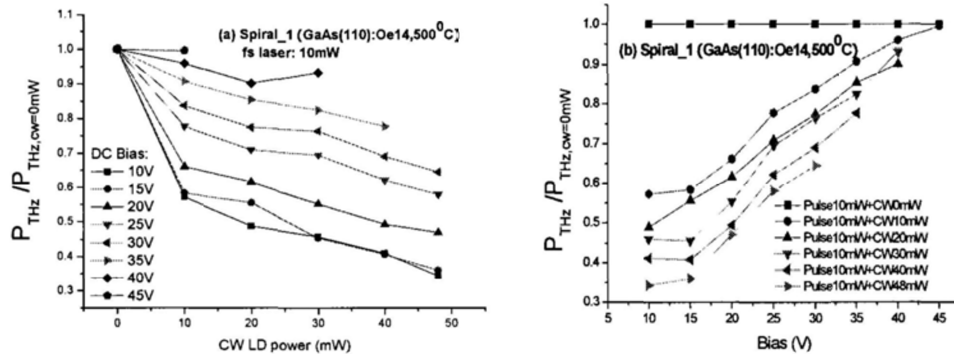

Figure4.24: The Change of THz power versus CW LD power or DC bias voltage for device spiral_1. (a)The modulation ratio of THz power vs. CW Laser diode power; (b)The modulation ratio of THz power at different bias voltages.

Three questions (1, 2 and 4) raised above are obtained their answers from the experimental results of spiral_1. Now, let's switch to another device (spiral_4) and take a look about the third question. With the same testing system as spiral_1, the device spiral_4 (GaAs(100):Oe13,500℃) is tested under 10mW and 20mW

pumping power of fs laser respectively . Comparing to the spiral_1, the THz power of spiral_4 is almost one order higher under the same testing condition. This allows us to investigate lower bias voltage within detect resolution of Golay cell, because the screening effect is more easily for observing under low electrical field. The reason will also be discussed later.

Figure 4.25(a) plots the traces of the THz power with different power of CW Laser diode. And the modulation ratio of THz power is also calculated and illustrated in Figure 4.25(b). From then, the normal tendencies discussed above are the same as spiral_1, but the additional one is the modulation ratio of THz power under different fs pumping power. Firstly, the THz power level is increased with the power of fs laser (Figure 4.25(a)), and, secondly, the effective screening effect is lowered down with the increasing of fs laser power (decreasing of modulation ratio with fs laser power), see Figure 4.25(b).

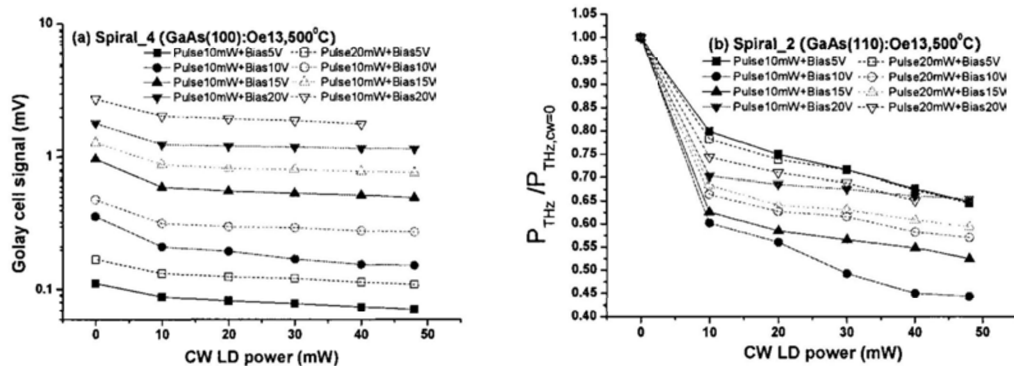

Figure4.25: THz power and modulation ratio under CW background illumination for device spiral_4 with different fs laser pumping power. (a) THz power vs. CW LD power; (b) The modulation ratio of THz power vs. CW LD power.

The further study about the fs pumping power versus modulation ratio of THz power is taken by spiral_3, which also fabricated on the substrate material the same as spiral_4. The power of fs laser injecting onto the PC device is increased from 4mW to 64mW for this testing. As we can see, in Figure 4.26, the screening effect is obviously decreased under higher fs laser injection level. This phenomenon is easy to understand, because the photocurrent generated by CW laser diode is only

occupy small percent of total photocurrent generated by fs laser and CW laser, under higher fs laser injection level, and it is lowered down with the increasing of fs laser power, which leading to the relative change of THz power by screening effect is also lowered down.

Come back to the Figure 4.25(b), one can find the curves of 5V bias are on the top both for 10mW and 20mW power of fs laser, little different with Figure 4.24(a) for spiral_1 which the curve of lowest bias voltage is in the bottom of the figure. To see this difference, the data in Figure 4.25(b) are re-plotted in the form of modulation ratio vs. bias curves (see Figure 4.27). The change of THz power is going down at first in the range of 8 to 14V, and then come back at bias higher than 15V like Figure 4.24(b). The data for which bias higher than 20V is moving toward lower modulation ratio should be expected in this figure from that tends of spiral_1 (Figure 4.24(b)).

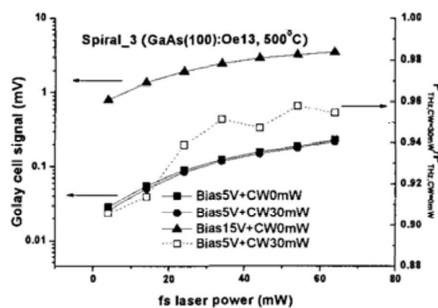

Figure4.26: THz power of spiral_3 under different bias voltages vs. fs laser power. Open square represents the modulation ratio under 5V bias and 30mW CW LD illumination (right y axis)

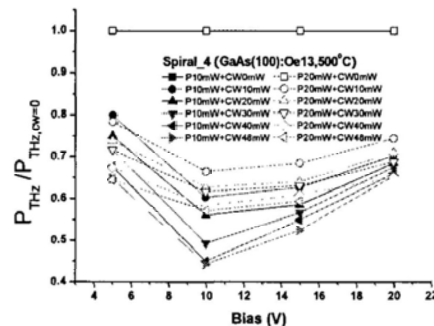

Figure4.27: The modulation ratio of THz power under different bias voltages for device spiral_4. The solid symbols and open symbols are for 10mW and 20mW fs laser pump powers respectively.

Another two devices were also tested to check these tends whether are common tends in Photoconductive THz devices. Device spiral_2 is fabricated on the same substrate material as spiral_1, the only difference between them is the turns of spiral antenna, which should only effect on the effective antenna resistance. The device spiral_5 has the same antenna structure as spiral_2, but its substrate material is Low temperature(200℃) grown GaAs (**Note**: this LTG GaAs material is different with

that one for dipole_8 and dipole_9, which is from different wafer.) and annealed at the same temperature,500℃, like other spiral antenna devices introduced above. Figure 4.28(a) and (b) illustrate the THz power vary with the power of CW laser diode from spiral_2 and spiral_5, respectively. Their decreasing tends of THz power under CW background illumination are similar to those spiral devices introduced above. From them, one can confirm this kind of tends essentially exists in the PC THz devices. Figure 4.28(c) and (d) show the modulation ratio of THz power under CW background illumination versus different DC Bias voltage. The tendency in them are also similar to those of other devices discussed above as showed in Figure 4.24(b) and Figure 4.27. The little difference among them should come from the measurement error which was magnified during the dividing calculation. Although the little difference exists, the main tends still could be deduced for common PC THz devices. The tendency is, for a given power of fs laser and CW Laser diode, the modulation ratio increases at first and then moves back to a lower modulation level under higher bias voltage.

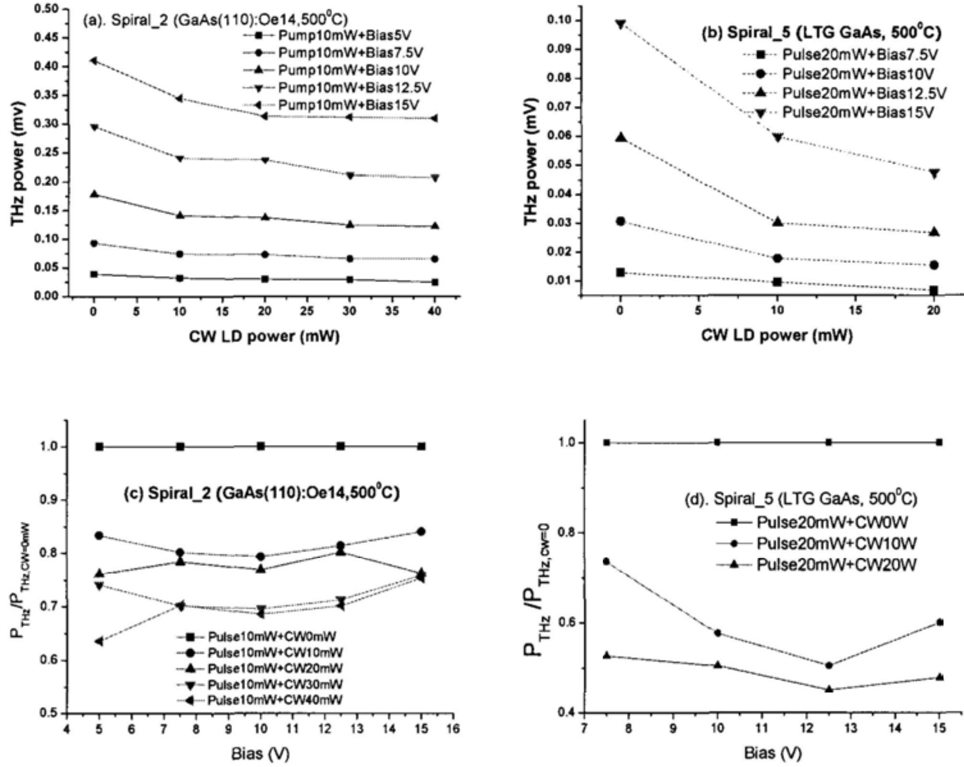

Figure4.28: THz power of spiral_2 and spiral_5 under different illumination power of CW laser diode: (a)spiral_2 and (b)spiral_5. THz power modulation ratio vs. bias voltage: (c)spiral_2 and (d)spiral_5.

The experimental results are already showed above, but the reasons haven't been discussed yet, only knowing the change is possible caused by screening effect. Now, let's try to discuss them by using a simple theory model.

From Eq.(4.34), we know the screening effect is mainly come from the space charge field and THz radiation field (or to say the part of bias field occupied by antenna resistance). As in this experiment, we measured the average power of THz wave, we don't need to know the dynamic space charge polarization or drift current from Eq.(4.5). Suppose the space charge polarization have an average value as $\langle P_{sc} \rangle$, then from Eq.(4.5), one can get:

$$\langle P_{sc} \rangle = J\tau_r \tag{4.35}$$

Where τ_r is recombination time of photocarrier. As introduced in chapter4.1, it is on the level of 100 ps. J is the photocurrent density. Then from Eq.(4.4), the average

space charge field should come to be:

$$\langle E_{sc} \rangle = \frac{\langle P_{sc} \rangle}{\eta_{geo}\varepsilon} = \frac{J\tau_r}{\eta_{geo}\varepsilon} = \frac{e\langle n \rangle \mu \langle E_{loc} \rangle \tau_r}{\eta_{geo}\varepsilon}. \tag{4.36}$$

The THz radiation field, in this case we prefer to call it as **Antenna field** (The electrical field from Bias field occupied by antenna impedance), can be calculated from Eq.(4.27) and Eq.(4.28)

$$\langle E_a \rangle = \frac{J \cdot \frac{A}{d_{gap}} lZ_a}{d_{gap}} = \frac{en\mu \langle E_{loc} \rangle \cdot \frac{A}{d_{gap}} lZ_a}{d_{gap}}. \tag{4.37}$$

In this experiment, the photocarrier density in Eq.(4.36) and Eq.(4.37) is contributed by two parts. One is from fs laser injection and the other is CW background illumination. So,

$$< n >=< n_{pulse} > + n_{CW} \tag{4.38}$$

Where, $<n_{pulse}>$ is the average value of photocarrier density caused by fs laser, when one use bolometer or Golay Cell as the detector to measure the THz wave. The factor $<E_{loc}>$here, also presents the average effective local field in photogap area.

Insert Eq.(4.36-4.38) into Eq.(4.34), one can get the effective local field which contributes to the generation of THz wave:

$$\langle E_{loc} \rangle = \frac{V_b}{d_{gap}} - \frac{e(\langle n_{pulse} \rangle + n_{CW})\mu \langle E_{loc} \rangle \tau_r}{\eta_{geo}\varepsilon} - \frac{e(\langle n_{pulse} \rangle + n_{CW})\mu \langle E_{loc} \rangle \cdot AlZ_a}{d_{gap}^2}, \tag{4.39}$$

A simplified expression is like follow:

$$\langle E_{loc} \rangle = \frac{V_b}{d_{gap}[1 + e(\langle n_{pulse} \rangle + n_{CW})\mu(\frac{\tau_r}{\eta_{geo}\varepsilon} + \frac{AlZ_a}{d_{gap}^2})]} \tag{4.40}$$

Considering the power of THz wave is proportional to the effective local electrical field and photocurrent density which generated by fs laser, $P_{THz} = E_{THz}^2 \propto (en_{pulse}\mu E_{loc})^2$, and the photocarrier density is proportional to the power of injection light ($\langle n_{pulse} \rangle \propto \eta_{e,pulse} \langle P_{pulse} \rangle \tau$ and $n_{CW} \propto \eta_{e,cw} P_{CW} \tau$, where $\eta_{e,pulse} \approx \eta_{e,CW} \approx \frac{(1-R)(1-\exp(-\alpha l))}{\hbar\omega Al} = \eta_e$,

$\tau = \tau_{trap}\tau_r / (\tau_{trap} + \tau_r)$), then we can get the expression of THz power as:

$$\langle P_{THz} \rangle \propto \left(\frac{e\eta_e \langle P_{pulse} \rangle \tau\mu V_b}{d_{gap}[1 + e\eta_e(\langle P_{pulse} \rangle + P_{CW})\tau\mu(\frac{\tau_r}{\eta_{geo}\varepsilon} + \frac{AlZ_a}{d_{gap}^2})]} \right)^2 \tag{4.41}$$

Now, from the model one can deduce several tendencies.

1.) When the P_{CW} equal to zero, which means no CW background illumination, the Eq.(4.41) will come back to the form of normal saturation equation as discussed above,

$$P_{THz} \propto (\beta \frac{P_{pulse}}{P_s + P_{pulse}})^2 , \tag{4.42}$$

which is similar to Eq.(4.21) and Eq.(4.32). As we have discussed the tendency in this situation before, so here it will not be mentioned again.

2.)When the P_{CW} is not equal to zero, which means the PC THz device is under CW background illumination, the output power of THz wave will be decreased (or limited) by a factor $d_{gap} e\eta_e \mu(\frac{\tau_r}{\eta_{geo}\varepsilon} + \frac{AZ_a}{d_{gap}^2})P_{CW}$ in the denominator. The larger P_{CW} leads to big value in denominator of Eq.(4.41), and at the end causes a smaller THz output power what could be generated by such PC device. This tendency can be found its proof in the figures (Figure 4.22(a), Figure 4.25 and Figure 4.28(a, b)).

3.) With a giving CW background illumination power (P_{CW}), one could obtain a larger P_s in Eq.(4.42), which leads to the saturation behavior curve to bend down. This can be proved by the data in Figure 4.26.

4.) If all the other parameters are fixed in the Eq.(4.41) and only DC bias is variable, then we could presume the curve of THz power vs. CW LD power will move upward step by step with the increasing of DC bias, keeping the curve profile no changed. The experimental results can reference to Figure 4.22(a), Figure 4.25 and Figure 4.28(a, b)). As we can find the little changes of the curve profile in those figures at this kind of situation, it implies some of those parameters what we thought unchanged with the bias voltage is practically related to the bias voltage (or to say it is a function of Bias voltage). To address this problem, we will discuss it

together with the tendencies of THz power modulation ratio under CW background illumination.

To discuss the tendencies of THz power modulation ratio under CW illumination, we should adjust the Eq.(4.41) like:

$$\frac{\langle P_{THz}\rangle}{\langle P_{THz,CW=0mW}\rangle} \propto \left(\frac{1+e\eta_e\langle P_{pulse}\rangle\tau\mu(\frac{\tau_r}{\eta_{geo}\varepsilon}+\frac{AlZ_a}{d_{gap}^2})}{1+e\eta_e(\langle P_{pulse}\rangle+P_{CW})\mu\tau(\frac{\tau_r}{\eta_{geo}\varepsilon}+\frac{AlZ_a}{d_{gap}^2})}\right)^2 \quad (4.43)$$

Firstly, from Eq.(4.43), one can deduce that the increasing of CW LD Power could increase the modulation ratio (which is inverse proportional to the value of $P_{THz}/P_{THz,CW=0mW}$). The value of $P_{THz}/P_{THz,CW=0mW}$ will come down from original 1 to a lower value, but higher than 0. The results in Figure 4.24(a) and Figure 4.25(b) can prove this deduction.

Secondly, the increasing of fs pump power (P_{pulse}) will increase the value of $P_{THz}/P_{THz,CW=0mW}$ and move it towards 1. The modulation ratio of THz power will go opposite way and go to decrease. Figure 4.26 shows the experimental results which match with this tendency deduced from Eq.(4.43).

Now come to the question, how to explain the tendency what we found in Figure 4.24(b), Figure 4.27 and Figure 4.28(c & d)? From Eq.(4.43), one can only get a deduction that the modulation ratio of THz power will never change with the bias voltage. But experimental results tell us another story. Then we have to check Eq.(4.43) more carefully and try to find out the possible reasons which cause the change in practical results showed in those figures. One possible reason is the effective mobility μ which is also not a constant but relative to the intensity of Bias voltage. As we discussed in Chapter4.1, commonly it is looked as a constant relative to the DC bias field. So, here we will neglect the possible effect of mobility vary under different bias voltage.

Then, the slight bias dependent factor should be the effective recombination lifetime τ_r. From Schockley-Read-Hall (SRH) theory [5] and field-dependence emission theory [110, 111], the effective carrier recombination lifetime is

proportional to the bias field and inverse proportional to the density of photocarrier on depletion regions. And, for the case the injection area larger than original depletion regions, the increasing of depletion regions with the bias field will enhance the inverse proportional relationship between the incidence light power and the effective recombination lifetime.

The effective carrier recombination lifetime should be slight bias dependence, like the form: $\tau_r \approx \tau_{ro} \exp(-bV_b)\exp(-c(V_b)n)$ .where τ_{r0} is the original effective recombination lifetime, b is the relative factor of bias field effecting on recombination lifetime, $c(V_b)$ is the scaling factor for the depletion regions with the bias field ($c(V_b)=cr*(V_b/(V_{sat}+V_b)$, Cr is the fitting factor, V_{sat} is the voltage for depletion region to saturate). So we can get the expression of τ_r in this case:

$$\tau_r(V_b, P_{light}) = \tau_{ro} \exp(-bV_b)\exp(-c_r \frac{V_b}{V_{sat}+V_b} \cdot \eta_e \tau P_{light}), \tag{4.44}$$

where, P_{light} is the total power of incidence light.

Then one can get a new form of Eq.(4.43) like:

$$\frac{P_{THz}}{P_{THz,CW=0mW}} \propto \left(\frac{1+F_1\mu \cdot t_r(V_b, \langle P_{pulse}\rangle)\cdot\langle P_{pulse}\rangle + F_2\mu\langle P_{pulse}\rangle}{1+F_1\mu\cdot\tau_r(V_b, \langle P_{pulse}\rangle + P_{CW})\cdot(\langle P_{pulse}\rangle + P_{CW}) + F_2\mu(\langle P_{pulse}\rangle + P_{CW})}\right)^2 \tag{4.45}$$

Where $F_1 = e\eta_e\tau\frac{1}{\eta_{geo}\varepsilon}$, $F_2 = e\eta_e\tau\frac{AlZ_a}{d_{gap}^2}$.

Now, let's use Eq.(4.45) to calculate the theoretical value of modulation ratio to see whether these calculation values can be good matching with those data showed in Figure 4.24. By setting the parameters $\tau=\tau_{trap}$=0.35 ps, μ=250 cm^2/V, $\langle P_{pulse}\rangle$ =10 mW, P_{cw}=10 mW, τ_{r0}=400 ps, we find the simulation curves are match with the experimental data in some degree (see Figure 4.29), with following fitting values for other parameters in Eq.(4.45), b=0.07; Cr=2.4e-21; V_{sat}=90.

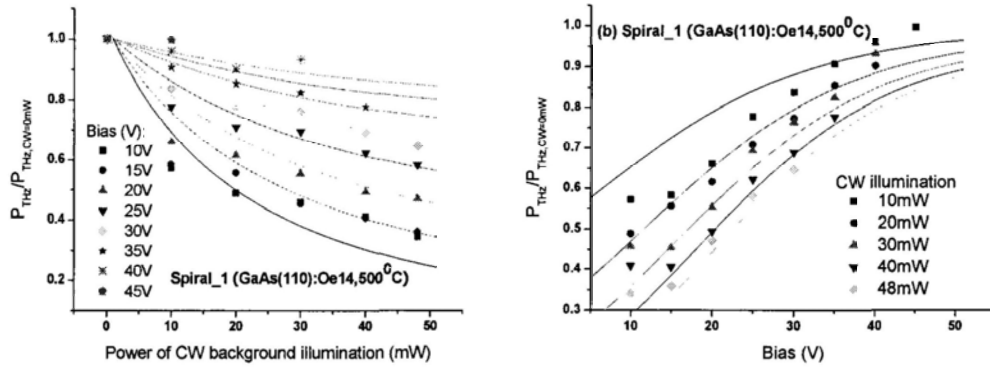

Figure4.29: Simulation results of the screening effect under CW background illumination for device spiral_1 tested under 10mW fs pumping.

From the simulation results, one could find the theoretical model is adequate in explaining the effects of CW background illumination on THz generation in photoconductive devices.

4.5 Summary

In this chapter we have reviews some theory models of pulsed THz wave generation. From them, one can understand the reason of pulsed THz wave generated from PC devices, and know the important factors for THz output power. To investigate properties of our oxygen ion implanted GaAs material on pulsed THz generation field, four experimental systems are set up in this work and help to study the GaAs:O materials.

From the THz output power testing experiment, we found GaAs:O based THz PC devices can generate relative high power (≈100μW). And GaAs:O potentially can generate higher output power of THz wave than LTG GaAs, with same antenna structure, although the dark current of GaAs material is larger than LTG GaAs (which means lower SNR value for THz signal).

The breakdown field of GaAs:O is not smaller than 225 kV/cm (270 V), which is close to that of LTG GaAs although there is still a long distance to catch up. But the pump power saturation level of GaAs:O materials is high than LTG GaAs

material, which allows GaAs:O to generate higher THz power by injecting additional pumping power.

From Figure 4.14(b), one can find the generation abilities of THz power of these materials tested in this work, they have a relationship like: GaAs:O>GaAs:As>LTG GaAs. As GaAs:O and GaAs:As are both grown by ion implantation method, this means the ion implanted materials have larger potential ability for generating high THz power, comparing with LTG GaAs material (which grown by MBE or MOCVD).

By measuring the THz spectrum of these devices with both FTIR and TDS method, we found LTG GaAs material has the broadest bandwidth among them. Although the GaAs:O could generate higher THz output power, their spectrums are scarified in some degree. The relationship of bandwidth of these materials is like following: LTG GaAs>GaAs:Oe13 (500℃) ≥GaAs:As >GaAs:O^{14}(550℃). (see Table 4.1). The different behaviors of GaAs:O materials (Oe13 and Oe14) suggests that, the preparation condition is very important, and it will lead to the big change of THz generation properties of the ion implanted material. There still have a lot space to optimize the preparation conditions (including the ion dosage, implant energy, and annealing temperature) of GaAs:O material to improve their performances, for example on THz spectrum if someone has another focusing point unlike ours (on THz power).

At last part of this chapter, we have investigated the pulsed THz wave generation with a CW background illumination. The experimental results tell us, the presence of CW background illumination will limit (or screen) the output power of pulsed THz wave. A larger illumination power of CW light, the smaller power of pulsed THz wave one could obtain. From this kind experiment, one can also find the modulation ratio is also a bias dependent factor. It will have a small value under high bias voltage (field), unlike that under low bias range.

For better understand such kind of screening behavior, a simple theoretical model is also introduced. The tendencies deducted from such theoretical model can

be testified by the practical measured data, which means the theoretical model is adequate in describing such kind of behaviors. Combining the experimental results and the simple theoretical model, this kind of investigation can help one to know more about "screening effect" and to think about some possible application of it.

Chapter 5: CW THz wave generation pumped by two single-mode lasers system

5.1 Introduction

For identifying the fine spectral features of certain materials, in practice, continuous wave (CW) THz imaging and sensing systems is desired, because of its distinct narrow band. Then, the devices which can generate CW THz wave are also attractive to researchers.

Above, we have tested our GaAs:O based devices under pulsed THz generation mode, in this chapter the GaAs:O material were further studied under the CW generation mode. We studied the CW THz power generation performances of different material based PC devices, and scanned their THz spectrum by varying the detuned frequency of the two single-mode CW lasers in this chapter. From experimental results, we found the GaAs:O based PC device can generate relative high power (hundred nW to several μW) CW THz wave, in 0.35 THz range.

At last, the bias dependent THz power generation behavior has also been studied experimentally and theoretically together. As in pulsed THz generation mode the bias field will also affect the THz spectrum in some degree by accelerating the carriers, so THz spectrums will be little different under different bias field. And the THz spectrums are also different for different materials. So, to compare the bias dependent behaviors (especially output power) under Pulsed generation mode, it looks little unsuitable (or to say little unreasonable). That is the reason why we didn't comparing the bias field-dependent saturation of these two materials (GaAs:O and LTG GaAs) in Chapter4, and left it to this chapter. The experimental results tell us, GaAs:O material has a relative higher saturation level for bias field, comparing to LTG GaAs.

5.2 Mechanism of CW THz generation in photoconductive device

Optical heterodyne downconversion (or photomixing) method is one of common approaches to generate CW terahertz wave from PC device. By this kind of method, CW THz wave can be generated by two single-mode CW laser beams with detuned frequencies in the THz range.

The heterodyne downconversion process occurs when the photoconductive device was illuminated by two single-mode CW laser beams, which having average powers P_1 and P_2 and frequencies f_1 and f_2, respectively. The instantaneous optical power incident on the PC device is given by [112]:

$$Pi = (P_1 + P_2) + 2\sqrt{mP_1P_2}[\cos 2\pi(f_2 - f_1)t + \cos 2\pi(f_2 + f_1)t] \qquad (5.1)$$

Where, m is the mixing efficiency which ranges in value between 0 and 1 depending on the spatial overlap of these two incidence laser beams and their relative polarization. (For example the mixing efficiency is 0, when the overlap beams have perpendicular polarization). The last term of Eq.(5.1) varies on a time scale much shorter than the carrier lifetime τ, and thus does not modulated the photoconductance significantly. The instantaneous photoconductance can be expressed as:

$$G_p(\omega, t) = en(\omega, t)\mu . \qquad (5.2)$$

Where, q is the electron charge and μ is the carrier mobility. And the $n(\omega,t)$ is the density of photocarrier produced by the incidence lights. $\omega = 2\pi f_d = 2\pi(f_2 - f_1)$ means the beating frequency of the two laser beams (It is also the center wavelength of THz wave generated by these two laser beams).

So, Eq.(5.1) can be written as a new form by neglecting the last term:

$$Pi = P_0 + 2\sqrt{mP_1P_2}\cos \omega t , \qquad (5.3)$$

Where, $P_0 = P_1 + P_2$ means the total incident power averaged over a long time period.

Like Eq.(4.2), the dynamic equation for the photocarrier density in this case can

be expressed like:

$$\frac{dn(\omega,t)}{dt}=\frac{\eta_e P_i}{hfAl}-\frac{n(\omega,t)}{\tau} \tag{5.4}$$

Where η_e is the external quantum efficiency (number of photocarrier pairs generated per incident photon), hf is the photon energy ($f_1 \approx f_2 \equiv f$), A and l are effective light incident area and thickness of absorption layer (or the absorption depth of material).

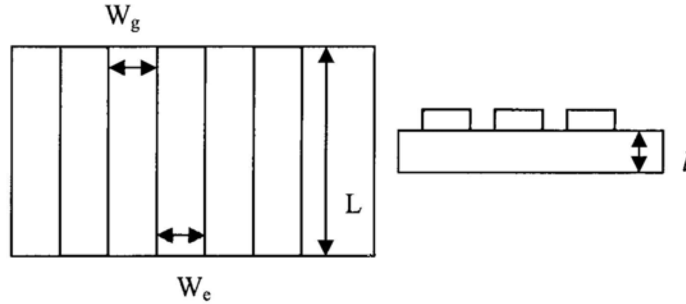

Figure 5.1 Interdigitated electrode configuration of photomixer

For the case of photomixer like Figure 5.1 shows, the effective light area and the external quantum efficiency can be calculated by following equations:

$$A=(N_e W_e + N_g W_g)L \tag{5.5}$$

$$\eta_e = \frac{N_g W_g}{N_g W_g + N_e W_e}\cdot \eta_i \cdot T \tag{5.6}$$

Where, W_g and W_e are widths of photogaps and electrodes, respectively. N_e and N_g are the number of electrodes and photogaps respectively. L is the length of electrodes, η_i is the internal quantum efficiency (number of photocarrier pairs generated per photon entering the substrate material). T is the transmission efficiency of incident light power.

By inserting Eq.(5.3) into Eq.(5.4), we can get:

$$\frac{dn(\omega,t)}{dt}=\frac{\eta_e (P_0 + 2\sqrt{mP_1P_2}\cos\omega t)}{hfAl}-\frac{n(\omega,t)}{\tau} \tag{5.7}$$

From Eq.(5.7), we can get the solution of photocarrier density like:

$$n(\omega,t)=\left(\int\frac{\eta_e[P_0+2\sqrt{mP_1P_2}\cos\omega t]}{hfAl}e^{\int\frac{1}{\tau}dt}dt+C\right)e^{-\int\frac{1}{\tau}dt}$$

$$=\left(\int\frac{\eta_e}{hfAl}[P_0+2\sqrt{mP_1P_2}\cos\omega t]e^{\frac{t}{\tau}}dt+C\right)e^{-\frac{t}{\tau}}$$

$$=\{\frac{\eta_e}{hfAl}[P_0\tau\cdot e^{\frac{t}{\tau}}+2\sqrt{mP_1P_2}\int(\cos\omega t)e^{\frac{t}{\tau}}dt]+C\}e^{-\frac{t}{\tau}} \tag{5.8}$$

As, $\int(\cos\omega t)e^{\frac{t}{\tau}}dt=\frac{\tau e^{\frac{t}{\tau}}(\cos\omega t+\tau\omega\sin\omega t)}{1+\tau^2\omega^2}+C'$, so

$$n(\omega,t)=\frac{\eta_e}{hfAl}[P_0\tau+2\sqrt{mP_1P_2}\frac{\tau(\cos\omega t+\tau\omega\sin\omega t)}{1+\tau^2\omega^2}]+C''e^{-\frac{t}{\tau}} \tag{5.9}$$

By setting $\sin\phi=\frac{1}{\sqrt{1+(\tau\omega)^2}}$, $\cos\phi=\frac{\tau\omega}{\sqrt{1+(\tau\omega)^2}}$, then one can get $\phi=arctg\frac{1}{\omega\tau}$ and $\cos\omega t+\tau\omega\sin\omega t=\sqrt{1+\tau^2\omega^2}\sin(\omega t+\phi)$. As the factor of the form $C''e^{-\frac{t}{\tau}}$ in Eq.(5.9) can be neglected since it decays on picosecond timescales, we can get the simplified expression of Eq.(5.9):

$$n(\omega,t)=\frac{\eta_e\tau}{hfAl}[P_0+2\sqrt{mP_1P_2}\frac{\sin(\omega t+\phi)}{\sqrt{1+\tau^2\omega^2}}] \tag{5.10}$$

For the case like Figure 5.1, the instantaneous photoconductance should be adjusted into:

$$G_p(\omega,t)\approx\frac{e\mu N_g Ll}{W_g}n(\omega,t)\,. \tag{5.11}$$

Insert Eq.(5.5-6) and Eq.(5.10) into Eq.(5.11), then one can get:

$$G_p(\omega,t)\approx\frac{e\mu N_g^2\cdot\eta_i\cdot T\tau P_0}{hf(N_eW_e+N_gW_g)^2}[1+2\sqrt{mP_1P_2}\frac{\sin(\omega t+\phi)}{P_0\sqrt{1+\tau^2\omega^2}}]$$

$$\equiv G_0[1+2\sqrt{mP_1P_2}\frac{\sin(\omega t+\phi)}{P_0\sqrt{1+\tau^2\omega^2}}]\,. \tag{5.12}$$

The Photoconductive devices can be drawn as the equivalent circuit like Figure 5.2 shows

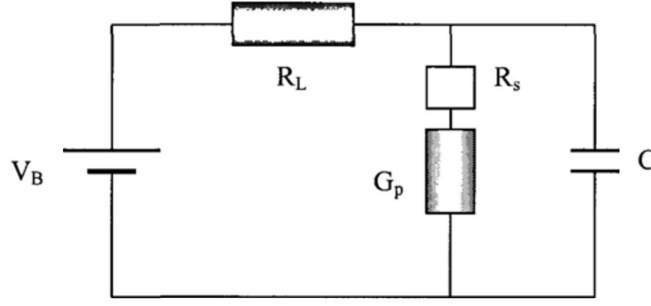

Figure 5.2: Equivalent circuit of PC device (Photomixer)

Where, R_L is the load impedance of antenna. C is the capacitance of the light incident area, V_b is the additional applied bias. Here the original series resistance R_S was neglected as long as $G_0R_S<<1$ and $R_L/R_S>>1$. Then the total impedance of equivalent circuit should be:

$$Z(\omega,t) = R_L + \frac{1}{G_p(\omega,t) + j\omega C}. \tag{5.13}$$

And taking the real part and disregarding the constant offset, one can get the output power of CW THz wave generated from load impedance:

$$P_{out}(\omega,t) = R_L[\frac{V_B}{Z(\omega,t)}]^2. \tag{5.14}$$

To get more information about the output power of CW terahertz wave with different beating frequency, the Kirchoff current law is required. From Kirchoff current law, one can write the time-varying voltage V_{loc} across the photogap as the solution of the following differential equation:

$$\frac{dV_{loc}(t)}{dt} = \frac{V_b - V_{loc}(t)}{R_L C} - \frac{V_{loc}(t)}{C} G_p(\omega,t). \tag{5.15}$$

For $G_p(\omega,t)$ in the form of Eq.(5.12), the Eq.(5.15) cannot be solved in a closed form. An approximate solution is found if $V_{loc}(t)$ is assumed to be of a harmonic form and neglecting the phase shift in the photoconductance. The radiation THz power is given by [31]:

$$P_{out}(\omega,t)=\frac{\frac{1}{2}(V_bG_0\beta)^2R_L[(1+G_0R_L)^2+(\omega R_LC)^2]}{(1+G_0R_L)^2[(1+G_0R_L)^2+(\omega R_LC)^2-\frac{1}{2}(G_0R_L\beta)^2]^2} \tag{5.16}$$

Where, $\beta=\frac{2\sqrt{mP_1P_2}}{P_0\sqrt{1+\tau^2\omega^2}}$. In the small-signal limit, where $G_0R_L \ll 1$, and under the assumption that $P_{out}(\omega,t)$ is the maximized ($m=1$, $P_1=P_2=P_0/2$), the Eq.(5.16) reduces to

$$P_{out}(\omega,t)=\frac{\frac{1}{2}(V_bG_0)^2R_L}{[1+\tau^2\omega^2][1+(\omega R_LC)^2]} \tag{5.17}$$

When $\omega\tau \gg 1$ and $\omega R_LC \gg 1$ (in the limit of high frequencies), the above small signal expression for $P_{out}(\omega,t)$ will reduce to $P_{out}(\omega,t)=\frac{1}{2}(V_bG_0)^2/\tau^2\omega^4C^2R_L$. It is very important for the PC devices to have low τ and C, since the difference -frequency power is dropping by 12dB/octave in this high frequencies limit. For the case under $\omega\tau \gg 1$ **or** $\omega R_LC \gg 1$, the spectral bandwidth of the PC device is limited by the free-carrier lifetime τ and the RC time constant of the device respectively, the power is roll-off by 6dB/octave. In Eq.(5.17), V_bG_0 can be looked as the dc photocurrent $I_{DC,ph}$ ($I_{DC,ph}=V_bG_0$) , which generated by the two laser beams under certain bias voltage (V_b). Then

$$P_{out}(\omega,t)=\frac{\frac{1}{2}I_{DC,ph}^2R_L}{[1+\tau^2\omega^2][1+(\omega R_LC)^2]}. \tag{5.18}$$

Figure 5.3 is the simulation results of THz power against the beating frequency, through the theoretical model discussed above. For the THz wave which frequency is above 3 THz, the effect of material carrier lifetime is very closely. But for those the frequency components below 3 THz, they will be more related to the material carrier lifetime. For the materials with the longer carrier lifetime, the effects of carrier lifetime on each frequency component will be much different. THz wave output power will decay fast with the increasing of frequency.

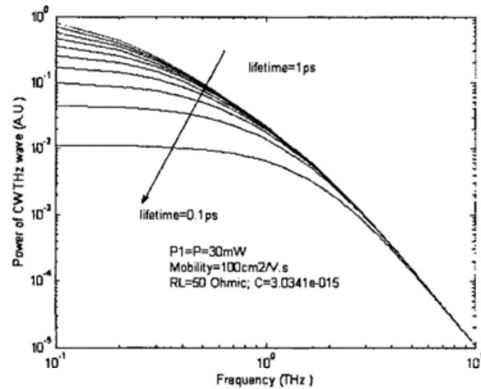

Figure5.3: THz power vs. beating frequency (simulation results)

For the materials which have shorter carrier lifetime, the effects of lifetime on each frequency components are more closely. For example, the curve (lifetime=0.1 ps) for the frequency components from 0.1 THz -0.8 THz. If one is only focusing on the THz wave in the range (below 0.5THz), he (she) don't require material with an ultrashort carrier lifetime like 0.1ps. Otherwise the power generation efficiency will be sacrificed unnecessarily. This is also one reason why the GaAs:O material is more suitable for generating THz wave in this range, comparing with LTG GaAs.

From figure 2.19, one can find the slow decay part of the carrier lifetime, which should be an important factor effective THz generation. A long carrier lifetime limit the CW THz generation performance in high frequency range (in Figure 5.3). But if one is interested only in high power CW THz generation in the low frequency range, the long decay may not matter much.

In the case of pulsed THz generation, the effect on THz generation performance for high frequency components is similar to CW THz generation. In pulsed THz generation case, as most energy of the pumping power is located in a short time range, the fast decay part of the carrier lifetime should be the dominating factor for the THz spectrum of pulsed THz wave.

5.3 Experimental results and discussion

5.3.1 CW THz wave generation and detection system

To test CW THz wave generation properties of our GaAs:O based PC devices, a typical experimental system for generation and detection of coherent CW THz wave was implemented as Figure 5.4. This kind of system includes three parts: 1. Laser source and beam combination sub-system, 2. THz wave generation sub-system, 3. THz wave collection and detection sub-system.

The laser source is normally constituted by two single-mode lasers [113] or a single laser which operating in two-color mode [114, 115]. In this work, two frequency-independent circular laser diodes (SANYO: DL-8032-001, 830nm) were used to generate two laser beams with a detuned frequency ω. Their center wavelength and linewidth are 830nm and 22MHz, respectively. To keep the laser source work more stably, two isolators utilized to prevent the optical feedback (from other optics) into the LDs. After passing through the PBS (polarization beam splitter), these two beams will be combined with two crossed polarization directions. By rotating the λ/2 plate placed after PBS, the components of two polarization directions through the polarizer can be controlled. Finally, each component of those two laser beams passed through polarizer are adjusted to have the same power.

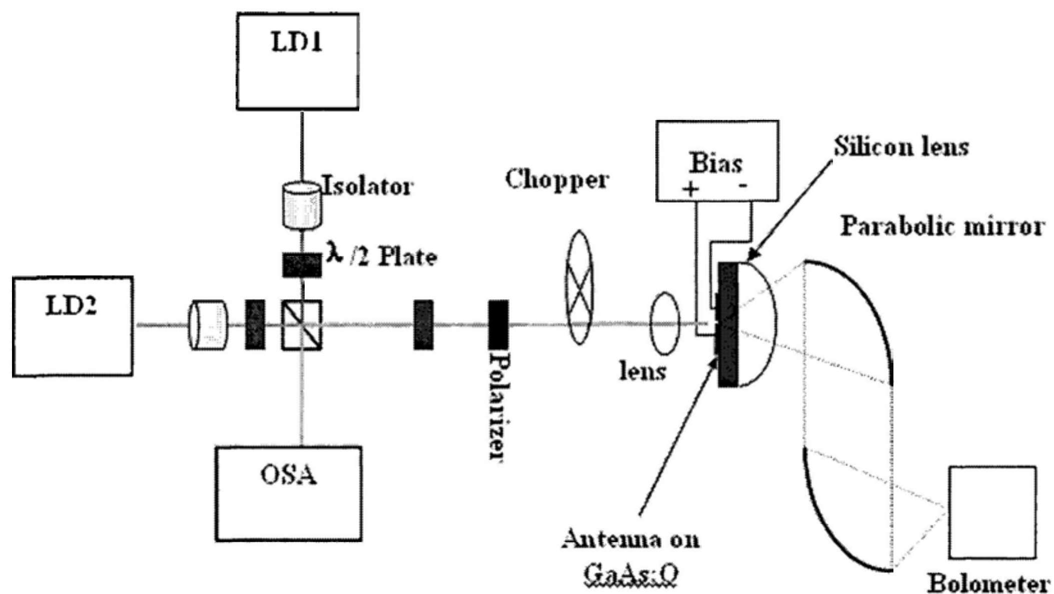

Figure5.4: Schematic of experimental setup for CW THz generation with two color laser system. (Measure output power and other electrical parameters.)

The THz wave generation sub-system and the THz wave collection and

detection sub-system are similar to the setup in Chapter 4 for pulsed THz wave generation. A 40× objective lens is used to focus the combined laser beam onto the photogap area of device. With the help of electrical bias, the modulated photocarrier density will create a modulated electrical current, which at the end leads to the CW THz wave to generate from this PC device. Two parabolic mirrors are used to collect THz wave and focus it into the liquid-helium-cooled Si bolometer detector.

As the 0.3 THz range is more attractive to researchers than those lower frequencies. So we test the CW mode generation properties of devices focusing on this range. By adjusting the difference between the wavelength ($\Delta\lambda$) of those two 830nm laser diodes, we generated corresponding CW THz wave from PC devices (which fabricated on GaAs:O substrate), through difference frequency generation mechanism.

5.3.2 CW THz wave and high-dose GaAs:O material

In Chapter 4, we have tested the GaAs:Oe14 material under fs laser pumping (pulse mode generation), here we will test the same device (Dipole_1) under CW light pumping to see its generation performance of CW THz wave.

From Eq.(5.5)-Eq.(5.6) and Eq.(5.10)-Eq.(5.12), we can get:

$$G_0 = \frac{\mu e \eta_e \tau P_0 N_g L}{hfAW_g}. \tag{5.19}$$

The situation when the photocurrent ($I_{DC,ph}=V_b G_0$) increases with bias linearly, the parameters in Eq.(5.19) should be bias-independence, especially effective mobility μ and carrier lifetime τ. Under high bias field, the effective mobility μ should be a bias-dependent factor, because drift velocity v_d ($v_d = \mu E$) is nonlinear dependence on bias under high field range [116, 117]. And the carrier lifetime (carrier trapping time) also should be a bias-dependence factor under high bias field, because the effective cross-section of Coulomb-attractive electrons traps decreases with the increasing electrical field due to the electron heating and Coulomb-barrier lowering [118]. To simplify the testing condition, in this part, we just tested

Dipole_1 in relative low field range (<3.5kV/cm, 70V on 20μm photogap).

Figure 5.5 shows the photocurrent of dipole_1. Two CW laser beams (P_1=P_2=P_0/2) are combined together through polarization beam splitter and focused onto the photogap of PC device (dipole_1, on GaAs:Oe14 substrate). The detuned frequency of these two laser beams is set at **0.327 THz**. The photocurrents under different CW pumping power almost increase with bias linearly, it shows that the nonlinear behavior of effective mobility and carrier lifetime haven't appeared obviously yet, although there are some slight nonlinear in the curves. Then, in this situation, from Eq.(5.17) we can know the output power of PC device under CW generation mode should be quadratic dependence on bias voltage (Power law).

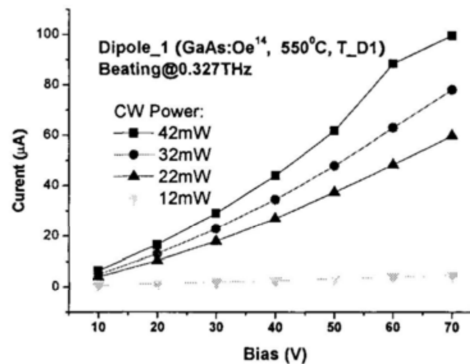

Figure 5.5: photocurrent of dipole_1 under the pumping of two CW laser beams

Figure 5.6 shows the CW THz power generated by dipole_1 under CW generation method. The fitting curves (dash line) for 42mW and 32mW pumping show the experimental results are good matching with the theory model. Under 42mW pumping and 70V DC bias condition, the CW terahertz wave power is around 0.55mV (≈0.011μW).

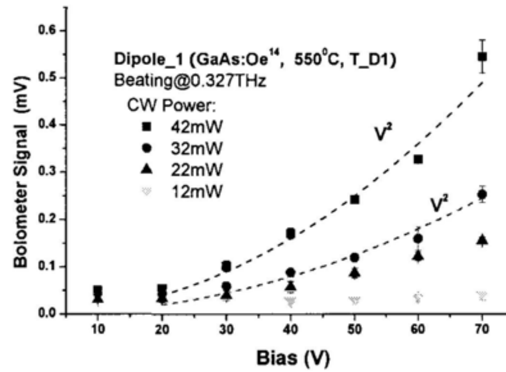

Figure5.6: CW THz power of dipole_1. The beating frequency is set at 0.327 THz. Dash lines are the curve fitting with quadratic law.

Such level output power is about 2~3 orders smaller than that achieved by pulsed generation method under the same bias voltage and pumping power (average). Although the theoretical model (equations) for them are different and it is not fair to compare them directly, if one wish to know why they have so much different output level, there are still some points that could be discussed. At first, both pulsed or CW generation methods are generating THz wave by modulating the photocurrent of semiconductor material, on which PC antenna fabricated. The pulsed generation method was using fs laser beam to generate photocurrent, while CW generation method uses two frequency-detuned laser beams. With the same average pumping power, fs pulse has higher peak power than CW beating wave. From Eq.(4.7) or Eq.(4.8), we can find the THz output power is proportional to the derivative of photocurrent. It means, under the same average pumping power, the one with narrower pulse width will have higher peak pumping power, and then more significant variation of photocurrent, at the end leading to a higher output THz power generated. So this is intrinsic reason why CW method will generate lower average THz power than Pulsed method. This also suggests that to generate higher narrow band THz wave, one can choose quasi-CW generation method, which uses two pulsed (time domain) laser source with a detuned frequency (frequency domain) [119]. This kind of method can combine the advantages of pulsed and CW THz

generation method together, to generate high power narrow band THz wave.

Secondly, the 2~3 orders difference is not only caused by the reason discussed above. From Eq.(5.1), we can find the beating efficiency will be affected by the working condition (stability) of laser diodes. When the phase matching condition is fulfilled, then the best beating efficiency could be achieved. As we know, currently we use two independent laser diodes, without any phase locking control. Although the laser diodes have very good stability, the situation of phase mismatch will still happen, which will cause the THz generation efficiency to decrease in some degree. One solution is to use some phase locking technique to lock these two laser sources together [120]. Another choice is to using some laser source with dual-wavelength operation mode [114].

Thirdly, as there are two laser beams, the perfect spatial mode matching is also very important for efficient THz generation. The optical alignment procedure is not ideal in practical use, so the resulting mismatching of spatial mode will cause the THz generation efficiency to decrease obviously. One solution is to use fiber to guide these two laser beams before pumping on photoconductive antenna [121].

Fourthly, the average power measured by bolometer detector for pulsed THz wave will be not very accurate like that for CW THz wave, because the calibration work was done under CW mode with blackbody radiation source. And the bolometer is a device with relatively slow response time and reset time (the time to return to thermal equilibrium with the environment) compared with the fs laser pulse width. The real power of pulsed THz wave may be lower than the value obtained by bolometer detector.

One of the advantages of CW terahertz wave generated by Photoconductive method is its wavelength turning ability. By adjusting the beating frequency of the two pumping CW laser beams, one can get the designed THz frequency component. This technology is very important for high resolution THz spectroscopy or CW THz imaging.

From Eq.(5.17), one can expect the output power of THz wave at certain

frequency should be different to other frequency even their working conditions (for example, pump power and bias voltage) are the same. Another factor should be considered is the antenna structure. For a broadband antenna like bow-tie or spiral antenna, the output power of THz power should be decrease with the increasing of beating frequency like Figure 5.3 shows, because those two terms in the denominator of Eq.(5.17) are both increasing with the beating frequency (ω). The effective antenna impedance R_L is nearly the same for most frequency of THz wave in the certain frequency range. Unlike broadband antenna, dipole antenna has his resonance frequency for a giving dimension. So, as the sample what we test is dipole_1, its behavior of THz wave in frequency domain should be very different with that in Figure 5.3. The power of THz wave will increase with the increasing of beating frequency at first, and then go to decrease like Figure 5.3 after the beating frequency exceeds the resonance frequency.

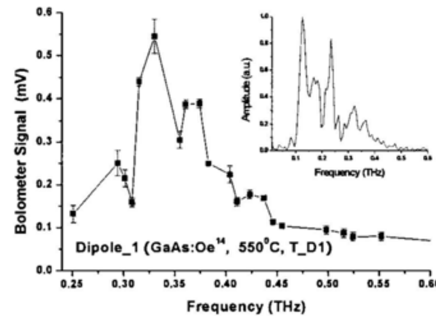

Figure5.7: Power of CW THz waves generated by dipole antenna fabricated on GaAs(110):Oe14 material. Insert shows the spectrum of THz wave generated by the same device under pulsed mode measured by FTIR System.

Figure 5.7 shows the test result of dipole_1 for its performance in frequency domain. It is obtained under the 40mW CW pump power and 70V bias condition. The insert window is the spectrum obtained by FTIR system (pulsed generation mode in chapter4). The curve of CW THz wave in frequency domain is good matching with the spectrum of Pulsed THz wave for the same device. As the calculated resonance frequency of dipole_1 is around 0.256 THz (**Table 3.1**), the unexpected deep in the curve below 0.32 THz should come from the cavity resonant

effect (like FP cavity effect), because the two smooth face of GaAs substrate make the sample more like FP cavity, which leads some THz frequency components and CW pump light resonant in the substrate material. This phenomenon is much clear in the insert window. So it is obviously that, the whole curve of CW THz wave spectrum in Figure 5.7 is good matching with the characteristics of antenna structure.

To minimize the effect of cavity resonance effect, one could try to polish the substrate to a thin film which thickness is smaller than the resonance length of certain THz frequency component. Another approach is to achieve best contact with Si lens, letting more resonant THz components going into the Si lens before the resonance happened in GaAs substrate.

From the result, one can find the peak power of CW THz wave near the 0.3 THz is found at 0.33 THz (the frequency near 0.3 THz is what we interesting), its power is around 0.55 mV (≈0.011 μW). Although the output power of CW THz wave is not very large, it could be enhanced by increasing the bias voltage and pump power. From Chapter 4, one can find the condition of 40mW pump and 70V bias has not reached to the saturation level of such kind of device, not only the pump power but also the bias voltage. There are still a lot of spaces for one to enhance or optimize.

5.3.3 Comparison of Low-dose GaAs:O and LTG GaAs

As introduced in Chapter 4, the GaAs(110):Oe13(500℃) material shows its better performance on THz spectrum comparing to the GaAs(110):Oe14(550℃), and its THz output power is also slightly larger. Now, here will show its performance on CW terahertz wave generation. Again we tested the device dipole_4_2, which is fabricated on GaAs(110):Oe13 substrate and its dipole type is T_D1 (Table 3.1). The calculation resonance frequency of such device is around 0.256 THz, like dipole_1 above. Like studying the dipole_1 by CW THz generation method, here we also plotted the spectrum curve of dipole_4_2 (see Figure 5.8). The maximum

output power (0.7444mV) was achieved at 0.333 THz under 70V bias and 45mW pumping power condition. The range (0.33 THz-0.34 THz) should be resonance peak range of this device. The fast decay of THz power for those THz components, which frequency slightly lower or higher than that value, represents the device's intrinsic characteristic of antenna structure. The further decay at high frequency should come from the normal frequency component decay mechanism like Figure 5.3 shows.

The 0.744mV (≈0.015μW) output CW terahertz power from dipole_4_2 (GaAs:Oe13) is also 40% higher than that obtained by dipole_1 (0.55mV, GaAs:Oe14), although during the testing dipole_4_2 (45 mW) had only a 12.5% additional pumping power larger than dipole_1 (40 mW). This also testify the good performance of GaAs:Oe13 in CW THz wave generation area, not only the spectrum, but also the output power.

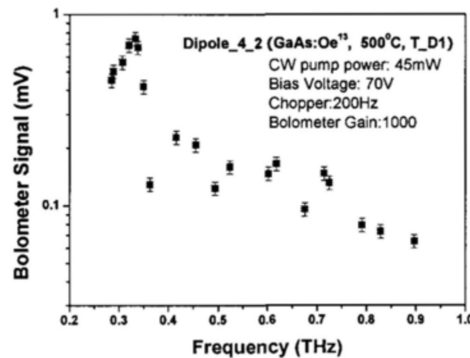

Figure5.8: Performance of CW THz wave generated from Dipole_4_2 under 70V bias and 45mW pumping condition.

As LTG GaAs material is the common material for THz application, so we also have tested the device (dipole_9), which fabricated on LTG GaAs materials, under CW generation method. This device has the same dipole structure as the dipole_4_2 (GaAs:Oe13) and dipole_1(GaAs:Oe14). Figure 5.9 shows the photocurrent and CW THz power under different bias voltage. The linear increasing of photocurrent shows that this device is working in normal linear bias-dependent range. The red

dash line is the fitting curve of CW THz output power of dipole_9. Its nearly quadratic behavior is good matching with the theory model as discussed above. The output power reaches to about 0.58mV at 0.366 THz under 60 V bias. In this figure, the low dark current and high photocurrent also shows the advantages of LTG GaAs materials in THz application area, especially SNR aspect.

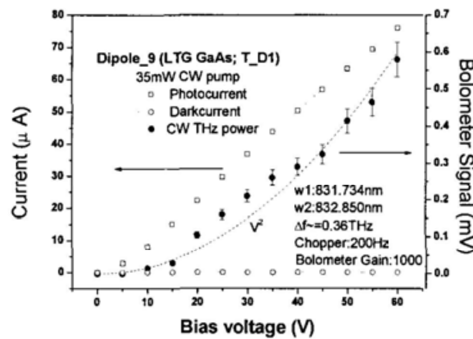

Figure5.9: CW THz power and photocurrent of dipole_9 (LTG GaAs) under 35mW pump. The red dash line is the fitting curve with quadratic law.

To achieve the best comparing results, we tested the dipole_4_2 (GaAs:Oe13) and dipole_9 (LTG GaAs) under the same testing condition. At first, let's take a look the performance of photocurrent of these two devices. The beating frequency is set at 0.359 THz and the pump power is set to 45mW for both of them. Figure 5.10(a) show the IV curve of these two devices. About dark current, these two devices both have small value comparing to the photocurrent, which shows these two kinds of material both having large dark resisitivity.

Unlike LTG GaAs material, GaAs:Oe13 material exhibits more obvious nonlinear bias-dependent behavior on photocurrent, this will affect the behavior of THz wave output power (About this we will discuss later).

From Figure 5.10(b) (solid symbols), one can find the LTG GaAs has a very good photocurrent behavior compared with GaAs:Oe13. The PDR value (photocurrent to dark current ratio) of LTG GaAs is at the level 1K, but that of GaAs:O^{13} is only at the level 10. The PDR values of these two samples both increase with the bias voltage, but it approaches the saturation level around 3K for

LTG GaAs material. From these results, one may suppose the PDR value of GaAs:O material will keep on increasing with the bias voltage before its breakdown. (The breakdown voltage of GaAs:Oe13 can be higher than 270V (Figure 4.15)).

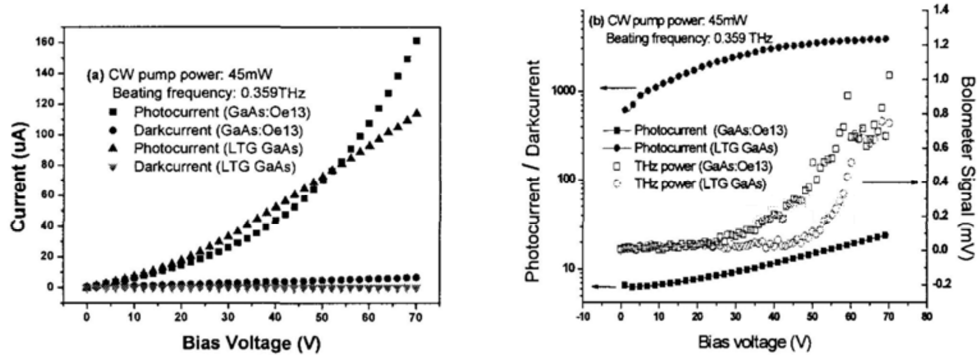

Figure5.10: Current and CW THz power of dipole_4_2 (GaAs:Oe^{13}) and dipole_9 (LTG GaAs). (a) IV curve measured under 45 mW CW pump power @ 0.359 THz, (b) The ratio of photocurrent to darkcurrent vs. bias voltage (solid symbols) and CW THz power under different bias voltages (open symbols).

The CW THz power of these two devices increases fast when the bias voltage is larger than 40V and 50V respectively (Figure 5.10(b)). The larger photocurrent leads to the larger CW THz power achieved by dipole_4_2 (GaAs:Oe13) comparing with the dipole_9 (LTG GaAs). The maximum output power achieved by GaAs:Oe13 and LTG GaAs are 1.0228mV(≈0.0205μW) and 0.756mV (≈0.0151μW), respectively.

From this figure, one also can find a bias dependent saturation behavior in LTG GaAs based devices when the bias voltage comes into the range (>60V). For GaAs:O material, this kind of behavior is not very obvious comparing with LTG GaAs, Its output power of THz wave still increases. This shows the GaAs:O material should have better performance of CW THz power generation in higher bias voltage range comparing with LTG GaAs material.

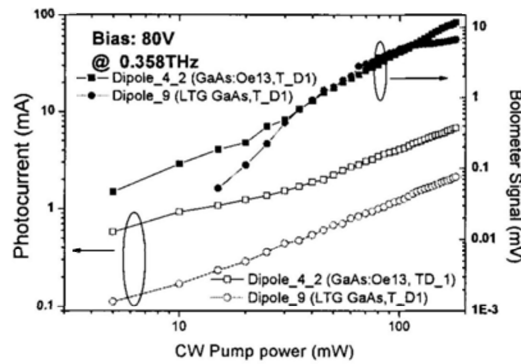

Figure5.11: Photocurrent (open symbol) and CW THz output power (solid symbol) under different CW pump powers for dipole_4_2 (GaAs:Oe^{13}) and dipole_9 (LTG GaAs). The beating frequency is set at 0.358 THz.

Now, let's take a look about their performance on photocurrent and THz output power under different CW pump power. Figure 5.11 shows the testing results of them under 80V bias voltage. The CW pump power is from 0mW to 180mW (Such high pumping power is achieved through MOPA, by amplifying the original laser beam. The setup detail will be showed later). Dipole_4_2 (GaAs:Oe13) and Dipole_9 (LTG GaAs) both have a linear increasing photocurrent with the pump power almost in the whole testing range. But, the CW THz output power of dipole_9 (LTG GaAs) is going to saturate around 120 mW, whereas that of dipole_4_2 (GaAs:Oe13) still keep increasing. These kind results shows that GaAs:Oe13 has larger pumping power saturation threshold, which endows it an ability to bear higher pump power compare with LTG GaAs material, and then generate higher CW THz wave output power.

The THz spectrums of these two devices are studied by turning the beating frequency, under 80V DC bias and 45mW CW pump power. Figure 5.12 shows the plotted CW THz spectrum curve from 0.02 THz to 1 THz. From the logarithm scale figure (Figure 5.12(a)), one can find dipole_9 (LTG GaAs) has a flat curve in high frequency rang(>0.5 THz) comparing with dipole_4_2 (GaAs:Oe13). This means

dipole_9 (LTG GaAs) has better performance in THz wave generation at frequency higher than 0.5 THz. But for dipole_4_2 (GaAs:O), it looks it has better performance at lower frequency range for its relative higher output THz power. (About 1.2mV @0.358 THz for GaAs:Oe13 comparing with the 0.787mV @0.355 THz for LTG GaAs).

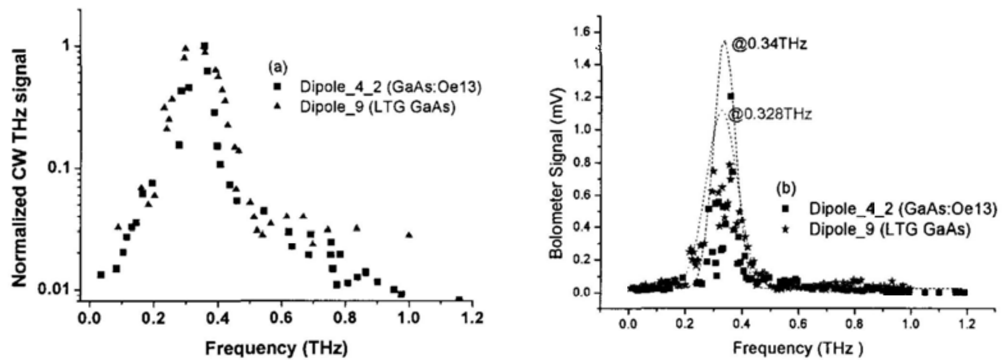

Figure 5.12: CW THz signal vs. beating frequency. (a) Normalized CW THz signal; (b) Original data in linear scale with Gaussian fitting curves [dash line for Dipole_4_2 (GaAs:Oe^{13}) , dot line for Dipole_9 (LTG GaAs)].

From the Gauss fitting curves in Figure 5.12(b), one can find the dipole_4_2 has a peak center (dash line) at 0.34 THz and dipole_9 (dot line) at 0.328 THz. And the resonance behavior of dipole antenna structure is more obviously in dipole_4_2 (GaAs:Oe13). This should be one of reasons for dipole_4_2 having the fast decay behavior at higher frequency range, as more possible power would transform to resonance frequency range.

To get more comparing results of these two kinds of devices (materials), we did further testing under high CW pump power condition (180mW). A Topica Master Oscillator Power Amplifier (MOPA) is used to amplifier the original two CW laser beams from (50mW) to a high power level (180mW). The testing system (Figure 5.4) is little adjusted into Figure 5.13 shows. An isolator is added before the MOPA to prevent the possible multi-reflection light going into the amplifier and increase the noise.

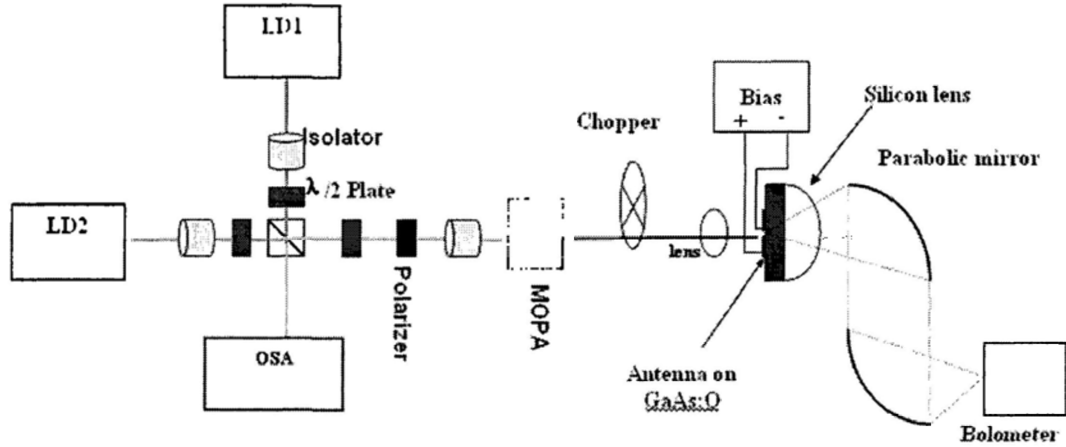

Figure5.13: Schematic of experimental setup for CW THz generation with two color laser system. (CW light is amplified by MOPA to around 180mW.)

Figure 5.14(a) shows the photocurrent of these two devices under 180mW CW pump power. The beating frequency of these two laser beams are set at 0.358 THz. The photocurrent of GaAs:Oe13 is going up linearly with DC bias below 10V, and then it increases with a quadratic law (superlinear photocurrent). Unlike GaAs:Oe13, the LTG GaAs device enter into the quadratic law until the bias voltage exceed 50V, but below 50V the photocurrent is also not linear dependent on bias voltage but more like with a relationship like $I \propto V^{1.5}$.

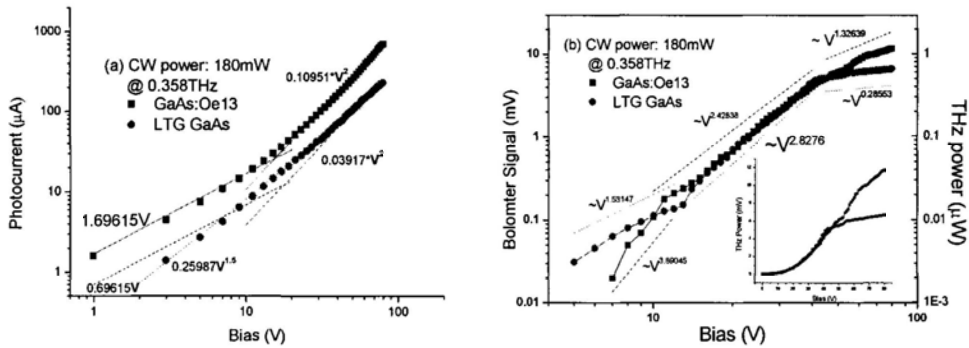

Figure5.14: Photocurrent and CW THz output power of dipole_4_2 (GaAs:Oe^{13}) and dipole_9 (LTG GaAs) under high CW pumping power (180mW). The beating frequency is set at 0.358THz. (a) Photocurrent (b) CW THz output power (1mV≈0.098μW). Insert

The CW THz output powers of these two devices are showed in Figure 5.14(b). From the results, one can find the GaAs:Oe13 device could potentially generate

higher output power than LTG GaAs device. By detailed observation, below 10V bias voltage, the CW THz output power of LTG GaAs device is slight larger than GaAs:Oe13. And then, from 10V to 40V, their CW THz output powers are similar. At higher bias voltage level, the output power of LTG GaAs device looks reach to its saturation level, however that of GaAs:Oe13 device keeps on increasing, with relative slight saturation behavior.

From Figure 5.14(b), one can also find, below 40V bias voltage, although the outputs of CW THz wave increase with bias voltage with a superquadratic law, they are not following the law of $P_{THz} \propto I_{DC,ph}^2 = (V_b G_o)^2$ (from Eq.(5.17) or Eq.(5.18)). The increase law of CW THz wave are more like $\sim V^{2.43}$ and $\sim V^{2.83}$ for GaAs:Oe13 and LTG GaAs respectively in this range, whereas the photocurrent is with a law more like V^2.

And, when the bias keep increasing, the CW THz wave output power of LTG GaAs device looks it is going to saturate, and the increase law with bias decreases to a level only $\sim V^{0.286}$. At the same time, although under the same bias voltage, the output power of GaAs:Oe13 device keeps increasing, the increase speed was slowed down to $\sim V^{1.33}$. But, in the same bias level (>40V), the photocurrent still increases with the bias with a law V^2.

These behaviors of CW THz wave and photocurrent could not be deduced from the Eq.(5.17) and Eq.(5.19) directly, if one think the other parameters in those equations are all bias-independence.

Note: the relationship (1mV≈0.098μW) used in Figure 4.14(b) is not the same as others quoted above (1mV≈0.02μW). Here we recover some factors which we have not accounted on the former one. One factor is about the power decay from the radiation source to the bolometer detector, during the bolometer calibration. If recover this part factor, the real power will be about 2.45 times(35.7/14.53) higher than that calculated from former one. And considering the chopping loss, there is also 2 times value could be recovered. So the relationship comes to 0.02*2.45*2=0.098 (μW/mV). So if all those power value calculated from the

former equation also considering like this, then their real power will also be about 5 times higher than current one.

5.3.4 Discussion on bias dependence behaviors

To study the saturation behavior of CW THz wave power happened at high bias range, one should consider some parameters are bias field dependence in fact. Now, we will try to discuss this kind of behavior (showed in Figure 5.14) with a theoretical model.

The nonlinear behavior of photocurrent of these two devices should be mainly caused by the bias dependent carrier velocity and carrier response time, which normally looked as bias independent in low electrical field for some semiconductors without or with low light power injection.

From Eq.(4.1)&Eq.(4.2) and under CW light pumping, the photocurrent should proportional to the effective carrier lifetime τ and the effective carrier velocity ν. And considering these two parameters are bias dependence factors ($\tau(E_b)$, $\nu(E_b)$) when the bias field exceeds a threshold, the DC photocurrent I_{DCph} should be following the virtue like:

$$I_{DC,ph} \propto \tau(E_b) \cdot \nu(E_b). \tag{5.20}$$

For bias dependence effective carrier velocity, the carrier velocity will start to saturate when the bias is keeping increasing in high bias field range. The effective carrier velocity can be expressed like following [79]:

$$\nu \approx \nu_e = \frac{\mu_e E_b}{\sqrt{1+(\mu_e E_b / \nu_{sat})^2}}, \tag{5.21}$$

where μ_e is effective electron mobility, and ν_{sat} is the velocity saturation value of electrons, E_b is the electrical filed ($E_b = V_b/d_{gap}$) on the PC devices. Here we take effective electron velocity as the effective of carrier velocity is because the velocity of electron is larger than the velocity of hole, which is neglected here during the calculation of the effective carrier velocity ν.

Because of the reduction of the electron capture cross section due to electron heating and Coulomb-barrier lowering, the effective carrier trapping time will increase with the bias field [118, 122] and leads to the effective carrier lifetime to increase. Then the effective trapping time can be expressed in a simple form like [123]:

$$\tau_{trap}(E_b)=\tau_{trap,0}+a_2E_b^2+a_3E_b^3+\cdots, \tag{5.22}$$

Where $\tau_{trap,0}$ is the effective trapping time without bias field. a_2 and a_3 are the fitting factors, $a_2, a_3>0$. For normal case, the first three terms dominate the value of trapping time.

Then, from Eq.(5.20)-Eq.(5.22), one can get the final expression of DC photocurrent, under the condition of $\tau_{trap}(E_b) \ll \tau_{recombination}$, $\tau_{trap}(E_b) \ll \tau_{drift}$.

$$I_{DC,ph}\propto(\tau_{trap,0}+a_2E_b^2+a_3E_b^3)\frac{\mu_eE_b}{\sqrt{1+(\mu_eE_b/v_{sat})^2}}, \tag{5.23}$$

where $E_b=V_b/d_{gap}$, as mentioned above.

When bias voltage is larger than V_b^{sat}, the threshold voltage for carrier velocity saturation, $\mu_e\frac{V_b}{d_{gap}}/v_{sat}>>1$, the effective carrier velocity will come to saturate at v_{sat}. Then Eq.(5.22) can be written in a new form:

$$I_{DC,ph}\propto(\tau_{trap,0}+a_2E_b^2+a_3E_b^3)\frac{1}{v_{sat}}. \tag{5.24}$$

To get equal form of Eq.(5.23), one should add the effect of carrier density generated by the light injection into the equation. So considering Eq.(4.1) and Eq.(4.2), one could use a fitting factor to describe the effect of the photocarrier.

$$I_{DC,ph}=Q_{qn}(\tau_{trap,0}+a_2E_b^2+a_3E_b^3)\frac{\mu_eE_b}{\sqrt{1+(\mu_eE_b/v_{sat})^2}}. \tag{5.25}$$

Where Q_{qn} is the fitting factor, it is proportional to the injection light power ($e\eta_eP_0$).

As the effective trapping time is smaller than other decay time factors, like carrier recombination lifetime, then one could get $\tau \approx \tau_{trap}$. Insert Eq.(5.22) and Eq.(5.25) into Eq.(5.18), one can get the new form of CW THz output power with some bias dependent parameters.

$$P_{out}(\omega,t) = \frac{\frac{1}{2} R_L [Q_{qn}(\tau_{trap,0} + a_2 E_b^2 + a_3 E_b^3) \frac{\mu_e E_b}{\sqrt{1+(\mu_e E_b / v_{sat})^2}}]^2}{[1+(\omega R_L C)^2][1+\omega^2(\tau_{trap,0} + a_2 E_b^2 + a_3 E_b^3)^2]}$$

$$= C_{rc} \frac{[Q_{qn}(\tau_{trap,0} + a_2 E_b^2 + a_3 E_b^3) \frac{\mu_e E_b}{\sqrt{1+(\mu_e E_b / v_{sat})^2}}]^2}{[1+\omega^2(\tau_{trap,0} + a_2 E_b^2 + a_3 E_b^3)^2]}. \quad (5.26)$$

Where C_{rc} is a factor relating to effective antenna resistance and capacitance,

$C_{rc} = R_L / 2[1+(\omega R_L C)^2]$.

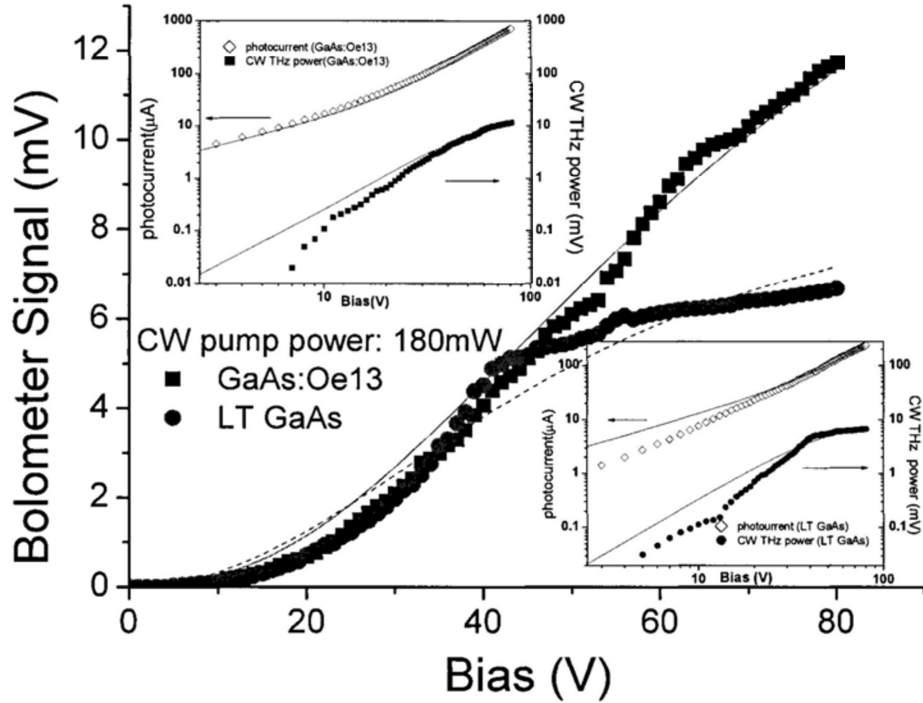

Figure5.15: Simulation results of CW THz power under different bias voltage [solid line is GaAs:Oe[13] (dipole_4_2) and dash line is LTG GaAs (dipole_9)]. Solid symbols are the measured values.) Insert window (left) is for photocurrent and CW THz wave of GaAs:Oe[13] and Insert window(right) is for those of LTG GaAs. (lines are fitting curves)

Figure 5.15 shows the simulation results of CW THz output power under different bias voltage using Eq.(5.26). The simulation curves (solid line and dash line) are good fitting to the measured data (solid symbols). For GaAs:Oe13 (dipole_4_2) and LTG GaAs(dipole_9), the values of parameters used during the simulation are different.

For GaAs:Oe13 device (dipole_4_2), we use the parameter values like: d_{gap}=20μm, ω =2π*0.358×10^{-12}, $\tau_{trap,0}$ =0.55 ps (measured by time-resolved photoreflectance technique pump-probe method). Other parameters are obtained by fitting the curve, μ_e =0.027 m^2/V·s, Q_{qn} =1.8×10^9, a_2 =2.9×10^{-25} m^2/V^2, a_3=3.2×10^{-33} m^3/V^3, v_{sat} = 1.0×10^5 m/s, C_{rc}=3.38×10^{-3}.

For C_{cr} in the equation Eq.(5.26) during the simulation process, one also should be mentioned that the power coupling loss induced during the measurement was accounted into this factor).

With these values of parameters, we can get the simulation results of photocurrent and CW THz output of GaAs:Oe13 (dipole_4_2) at the same time by Eq.(5.25) and Eq.(5.26). The fitting results are showed in the insert window (left) of Figure 5.15. From this insert window, one can find the fitting curves are good match with the measure data for both the photocurrent and CW THz output power at the same time.

For LTG GaAs device (dipole_9), The parameter values are set as: d_{gap}=20 μm (the same dipole structure as GaAs:Oe13), $\tau_{trap,0}$ =0.7ps (measured by time-resolved photoreflectance technique pump-probe method), μ_e =0.02 m^2/V·s [31], ω=2π*0.358×10^{-12} (0.358 THz, the same beating frequency as GaAs:Oe13). Other parameters are obtained by fitting the curve, Q_{qn}=1.8×10^9, a_2=1.55×10^{-25} m^2/V^2, a_3=2.2×10^{-33} m^3/V^3, v_{sat}=0.45×10^5 m/s, C_{rc}=7.4×10^{-3}.

Here we fitting the Q_{qn} factor for GaAs:Oe13 and LTG GaAs with the same value is supposing the photocurrent generation efficiencies of them are the same

under the same testing condition (CW pump power and beating frequency.)

The good matching of simulation results with the experimental results shows the theoretical model is adequate in describing the phenomenon happened in practice. Now, with the help of this theoretical model, we could discuss the behaviors of THz power saturation and quadratic photocurrent increasing in physics.

When the bias field is higher enough, the effective carriers trapping time and carrier velocity will follow into the bias-dependence range with a function like Eq.(5.22) and Eq.(5.21). When the bias keeps on increasing, the effective carrier trapping time will increase, but the carrier velocity will slowly close to its saturation level, normally <1e^7 cm/s [123]. The combine effect of them leads to the photocurrent increase with bias dramatically at high bias field, not Ohmic law but quadratic law. If the terms in the denominator of Eq.(5.26) are not bias-dependent, the output CW THz wave from PC devices should increase with the bias (quadratic law on the photocurrent). But the effective carrier trapping time increase with the bias field makes this term also increase with the bias field. This kind of increase forces the output power of CW THz wave follow into a fast decay status. Although the photocurrent keeps on increasing, the increasing of effective carrier trapping time counteracts some part of contribution by photocurrent on CW THz wave output power.

When the bias field is high enough (but below the breakdown value (>1e^5 V/cm) [31]) and makes the value of $\omega^2(\tau_{trap,0} + a_2E_b^2 + a_3E_b^3)^2$ more larger than 1, the output power of CW THz wave will come to its saturation level. In Figure 5.15, the measured data of LTG GaAs device shows this kind of saturation more obviously. The carrier velocity will dominate the output power of CW THz to keep increasing, if it hasn't reached its saturation level. As the values of $\omega^2\tau^2$ under the bias voltage (>40V) are both larger than 1 for GaAs:Oe13 and LTG GaAs devices, then, the higher saturation level of CW THz output power of GaAs:Oe13 should be mainly caused by the relative higher carrier velocity saturation value comparing with that

of LTG GaAs. The fitting parameters values of those two devices showed above prove the correctness of such kind of deduction (hypothesis).

The different value C_{rc} of these two devices mainly comes from the different effective capacitance, antenna resistance, and the power coupling loss. From the equations in the papers [124, 125], one could expect these two devices should have similar value of capacitance, because they have the same antenna structure and similar substrate material (GaAs). Then, the fact that the value of C_{rc} for GaAs:Oe13 is only about 3/4 of that of LTG GaAs, should be possible mainly coming from the power coupling loss during the measurement or effective resistance.

The curve of the photocurrent versus CW THz power in Figure 5.16 at low bias voltage range also suggests this possibility. In the figure, the CW THz power of GaAs:Oe13 does not increase with photocurrent by quadratic law like LTG GaAs under low bias field range, at which range the bias dependence effects on those factor (carrier trapping time and velocity) should be relative slight. This kind of result from Figure 5.16 suggests maybe there is relative less percentage of CW THz power of GaAs:Oe13 comparing to LTG GaAs device was coupled into the bolometer detectors during the measurement. If this possibility was true, then the CW output power generated by the GaAs:Oe13 device should be higher than current value.

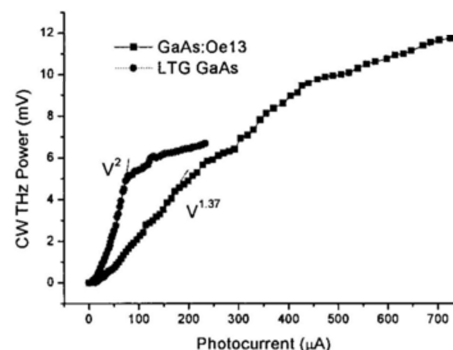

Figure5.16: CW THz power versus Photocurrent for GaAs:Oe^{13} and LTG GaAs devices.

From Figure 5.5, Figure 5.6 and Figure 5.9, one should be mentioned the bias dependent behavior is also pump power related. From those, under the same bias field (voltage), for lower pumping condition the photocurrent increases more like linear law with bias voltage and the CW THz power like quadratic law. Under the higher pumping power condition, the bias dependent behaviors of photocurrent and CW THz power are more obviously like above showed (Figure 4.15). So if one wants to get the more precise theoretical model for the all situation, he (she) should take into account those factors which would be pump power dependent.

5.4 Conclusion

In this chapter, The performances of GaAs:O materials (GaAs:Oe13 and GaAs:Oe14) on THz wave generation area were further studied, together with LTG GaAs materials. And the bias-dependent behavior was also studied experimentally and theoretically in this part.

From the electrical behavior (IV curve) of these materials, we found the LTG GaAs material has a higher SNR value comparing with GaAs:O material, but that of GaAs:O could be increased with the DC bias, whereas it will be saturated for LTG GaAs at certain bias.

Comparing the CW THz power and spectrum of these materials, one can find the GaAs:O material can generate higher CW THz output power, and its THz spectrum exhibits resonance behavior of dipole antenna structure more obviously. The maximum of CW THz wave measured in this work is on the level of μW (Achieved from GaAs:Oe13 based PC device, at 0.358 THz under 180mW pump power and 80V bias voltage condition).

Under low pump power condition, the photocurrent and CW THz power are more like following the normal law (linear or quadratic law with DC bias). With the help of higher pumping power, the bias dependent saturation behavior comes to be obviously and easy for observing and investigating. Comparing with the LTG GaAs material tested in this work, GaAs:O material has a relative slight bias dependent

saturation behavior, which allowing it to generate higher CW THz power than this type LTG GaAs material.

At the end, the good matching of simulation results and experimental data shows that the adjusted theoretical model is suitable for explaining this kind of bias dependent saturation. This kind of study on bias-dependent behavior gives us a possible explanation on the reason, why GaAs:O material could potential generate higher THz power than LTG GaAs material in CW THz generation mode. Considering this kind of behavior is more obviously under higher pump power, if one wish to get more precise theoretical model for the whole situation, he(she) should take into account those factors which would be pump power dependence.

Chapter 6: Conclusions and future work

The present work contains results obtained from investigating the pulsed and continuous-wave (CW) THz emission characteristics of photoconductive antennas based on GaAs:O (Oxygen ion implanted GaAs). The study is mainly aimed at evaluating the impact of material properties upon the THz generation performance, especially on the aspect of THz output power. From the Chapter 4 and Chapter 5, we find the GaAs:Oe14 material can generate about 1.55V **(≈31μW)** pulsed THz wave, under 35mW pump power and 70V bias voltage. And the GaAs:Oe13 material can generate higher THz power (≈48**μW**) than GaAs:Oe14, even its pump power is lower (25mW). This level THz output power is the highest one ever reported by such kind of generation method, to our knowledge. Comparing the high power pulsed THz wave generation ability of all those materials tested in this work, the sequence is like following: **GaAs:Oe13(500℃) ≥GaAs:Oe14(550℃)> GaAs:As > LTG GaAs**. Under CW generation mode (@**0.358 THz**), GaAs:Oe13 material can generate CW THz power as high as **11.72 mV** (μW level), compared with that 6.6765mV for LTG GaAs material under the same testing condition.

From the experimental results, We found GaAs:O material has a **relatively higher saturation threshold** compared with LTG GaAs material, which stresses the potential of GaAs:O materials on high power THz wave generation area. In this work, we also found the breakdown field of our GaAs:Oe13 material is larger than **225KV/cm**. Although it hasn't reached the level of LTG GaAs material (>500kV/cm [32]), the GaAs:O materials are good enough for generating high power THz wave, because its terahertz power generation efficiency is higher than that of LTG GaAs material, under the same high bias field testing condition **(>20kV/cm)**. If consider the relative high breakdown field of our GaAs:Oe13 and the THz power what we have achieved at 40kV/cm, one could expect that the power levels at **~200μW** may be achievable in GaAs:O materials.

The electrical property measurements (in Chapter 2) tell us the GaAs:O materials have a relative high dark resistivity (**>10^6Ω/sq**) and carrier mobility (**~200 cm^2/V·s**). And an ultrashort carrier lifetime (**<0.4 ps**) can also be achieved from oxygen ion implanted GaAs (GaAs:Oe13). These good performances of material endows GaAs:O material such kind of good performance of THz generation. To enhance its performance, by carefully optimizing the ion implant dosage and annealing temperature, one could achieve desired material properties (carrier lifetime, resistivity and carrier mobility) though the optimization of the density and characteristics of defects in certain material. Note: as these three properties have different proportional relationship with the density of defects, before starting the materials preparation process, one should make decision what is he (she) interesting (high THz frequency component or high output power of THz wave?), and then select a suitable preparing condition for material.

To enhance THz power generation from GaAs:O material, besides the method discussed above, one also can utilize some other useful technologies into his work. For example, grow a distributed Bragg reflector layer under absorption layer [126]. From the references [26, 30, 100], the highest field within the active layer is located near the metal contact, and it decrease extremely fast with distance between the contacts and depth of GaAs. With the help of Bragg reflector layer, one could decrease the normal GaAs:O layer to half thickness of the original one, which can not only enhance the bias field utilization efficiency, but also decrease the implant energy and then minimize the unwanted effect which could be induced by high energy implantation. And, this kind of technology also give one a chance to try some heavy ions, which are not easy to get as deeper as 1μm with normal low implant energy. Another technology for enhancing the bias field utilization efficiency is to fabricate some recessed interdigitated finger contacts, which can improve the electric field distribution in the active region. With this technology, the achieved power should be twice of that with conventional surface contacts [28]. Some other technologies like antireflection coating (a thin optically transparent

silicon nitride layer [100]) and AlAs heat spreader [126] could also be adopted for improving THz generation performance of PC devices. To enhance the thermal conductive efficiency, one can also use metal holder to replace the PCB we used in this work. By the way, if one wants to enhance certain frequency component, one should optimize the dipole antenna dimension and other parameters of the structure to move the resonance frequency of such a device to that frequency desired. A simplified resonance frequency calculation equation can be found in Chapter 3 (Eq.3.1). A more elaborate simulation should also account for the effect of substrate capacitance.

The best THz generation performance should be obtained after integrating all those technique mentioned above.

From the THz spectrum measured by FTIR and TDS systems in Chapter 4, the bandwidths of those materials tested in this work have a relationship like: **LTG GaAs >GaAs:Oe13(500℃) ≥ GaAs:As >GaAs:Oe14(550℃)**. To enhance the bandwidth of GaAs:O materials, one could decrease the carrier lifetime of GaAs:O material by creating enough defects (carrier trapping centers). The Optimized preparation condition (ion dosage and annealing temperature) of GaAs:O materials can help one to achieve such kind of purpose [127]. But it requires the THz output power to be sacrificed (as **Figure 5.3** shows). From scanning spectrum of materials under CW THz wave generation mode (Chapter 5), we found GaAs:O material presents a resonance peak sharper than LTG GaAs. This shows GaAs:O material has more potential for power enhancing in certain resonance frequency. If one is focusing on the aspect of THz power, this should be also one of good properties of GaAs:O material.

In Chapter2, one can find the defects created by the O+ ion though the ion implantation process act as deep trapping and recombination centers (mid-gap states within energy bandgap), which enhance the absorption coefficient from the traps to the upper excited states in the conduction band and the absorption coefficient of two-photon absorption. This kind of behavior is possible for one to fabricate some

special photoelectric devices. For example, one could use a CW light to act as the preload pumping (for example, 800nm) and creates enough trapped carriers in the trapping centers, then utilize a laser source (for example, 1550nm) to pump and re-excite those trapped carriers into the conduction band and be electrical active. So, like 800nm fs laser pumped LTG GaAs, the ion implanted material (for example GaAs:O) is also possible for one to generate THz wave by 1550nm fs laser pumping. This kind of method is little different with that through laser source frequency doubling [19] or the one through two photon absorption mechanism [128]. From Chapter 2, one can also find that the experimental method of light transmission looks can be used to quantitatively analysis of the relative defects (ions) densities of certain materials, because the different transmission rate is related to the different density of implanted materials. By such kind of method, one don't need to fabricate some metal contact on certain material and can get some useful information without sacrificing the samples.

In chapter 3, the photolithography technique is not reach to sub-micrometer level. As the bias-field is very important for THz wave generation, especially for CW THz wave generation from PC devices, a more compact structure (photomixer finger) is desired. To utilize the bias-field more efficiently, 0.2um wide electrode (finger) and 1.8um wide gap should be best structure for certain case [29]. For wide frequency turning application of CW THz wave from PC devices, one should adopt some antenna structures to replace the dipole antenna used in Chapter 5. Some antenna structures like bow-tie [61], spiral [60] are good selections.

From CW background illumination experiment in Chapter 4, one can find the pulsed THz wave generated by the fs laser pumping will be screened (reduced) by the CW background illumination. The high power of CW illumination, the higher modulation rate can be obtained (lower Pulsed THz power compared with the original level). And the bias voltage will also affect this modulation rate, this kind of screening behavior is more obviously in lower bias voltage range, and comes to be less in the high voltage level. One simple theoretical model is suggested in this

work for explaining such kind of behavior. Although it is still required to be optimized and modified, the theoretical model is adequate for deducing the trends of screening effect under CW background illumination. From this kind of experimental and theoretical investigation, one could find some applications of this kind of screen effect, for example, THz wave modulator fabrication or some physical studies (Appendix B).

Above, we have reviewed the valuable data and results achieved in this work, and discussed some possible optimize methods and directions. Now let's introduce some ongoing projects of ours. Unlike the laser system used in this work (chapter 4 and chapter 5), the fiber based system has all the pumping sources with fiber pigtail (or the laser beam could be coupled into fiber). Compared with the free space optics based laser source, the fiber based THz wave generation system generally has some advantages like compact size and high portability (for example, the device "quasi-optical UTC-PD module" [129]). Then, is it possible for GaAs based PC antenna pumped by 800nm light also through fiber (or fiber laser)? The answer is affirmative. The commercial product "Mini-Z" [19] is an instance already working. In such product, by doubling the 1550nm fiber laser beam to 780nm light, the GaAs based THz PC device can combine well with 1550nm fiber laser. Another approach could be like following: As the 800nm laser can generate higher output power than 1550 nm from current commercial products, if one can utilize its high power for THz generation that would be a very meaningful thing. So, currently one work we are trying to do is that, using a lens fiber to coupler the light of 800nm diode laser into a fiber, and using FBGs (Fiber Bragg Grating) to feedback certain wavelengths and to lock the radiation wavelength of such laser diode. Then, one could generate CW THz wave from GaAs:O based PC devices with the help of such kind of 800nm fiber laser (two-color fiber laser or two signal fiber lasers system). Then the size of THz wave generation system current used in this work (chapter 5) can be largely compressed.

As currently the 1550nm fs fiber laser is well developed compared to 800nm

fiber laser, another ongoing project is based on it. In this project we try to use some ion implanted materials which bandgap energy is corresponding to 1550nm. For example $In_{0.53}Ga_{0.47}As$:Fe [130] or $In_{0.53}Ga_{0.47}As$:O. Unlike GaAs material, the InGaAs material has small bandgap energy, which makes the work achieving high resisitivity to be more difficulty. As one can know from Chapter 2, to get good material properties of material for certain usage, the most preparation condition should be optimized step by step. Although we have tried several times, the electrical properties of our $In_{0.53}Ga_{0.47}As$:Fe or $In_{0.53}Ga_{0.47}As$:O materials are still not good enough for device fabrication. So this work is still at its just beginning. To test our fiber based generation system (source II, see Figure a.1 in Appendix C), some low temperature grown InGaAs material (LTG InGaAs) were tested at first. The LTG InGaAs based PC devices can generate about several tens μV output power of pulsed THz wave (Appendix C: Table a.1). The maximum value we currently achieved is about **93.2**μV. Although, this level output power looks not very large, it shows the fiber based generation system is suitable for work. The relative lower output power should be mainly related to the relative lower efficiency of device, because the LTG InGaAs material (grown on GaAs substrate) tested here is not well matched with 1550nm laser beam. So, for this kind project, there are some improve directions could be considered. *1*. Preparing good qualify material by continuing to optimize the preparation conditions of $In_{0.53}Ga_{0.47}As$:Fe or $In_{0.53}Ga_{0.47}As$:O, for ion implanted materials having some advantages compared with Low temperature grown one (have been discussed before). *2*. Adding photomixer structure (especially with recessed interdigitated finger contacts) to enhance the bias-field. **3.** Making the device more compact and system more integrated (pulsed and CW pumping combined together with fiber).

(PS: Some thoughts about the possible applications of THz wave or other research area, which are not directly related to this work, were showed in Appendix D just for reference.)

At the end, the author wishes to use the words of one excellent scientist (Prof.

Kodo Kawase) in this research area to finish this thesis, "A technology may end up a disappointment. THz is not technology, but frequency. A frequency region will not betray us!" So, let's

Love terahertz,

and

Grow with her!

Publication list

1. **Kejian Chen**, Yutai Li, WingYiu Cheung, Wei-wen Wang, Ci-Ling Pan, and Kam Tai Chan, "CW Sub-Terahertz wave generation by GaAs:O Materials," paper FH1-5, presented at CLEO/Pacific Rim 2007, Seoul, Korea, August 26 - 31, 2007
2. **Chen Kejian**, Li Yutai, Cheung Wingyiu, Wang Weiwen, Pan Ciling, Chan Kamtai, "THz waves generated by oxygen implanted GaAs", paper 1C5-5, presented at ISAP2007, Niigata, Japan, August 20-24, 2007
3. Y.T. Li (黎宇泰) and W.W. Wang (王韋文) and C.L. Pan (潘犀靈) and **K.J. Chen (陳克堅)** and K.T. Chan (陳錦泰), "低溫成長砷化鎵與多重氧離子佈植砷化鎵光導天線之 THZ 輻射特性之比較," paper CO-004, Optics and Photonics in Taiwan, Nov. 30-Dec.1, 2007, Taichung, Taiwan. (Best Student Paper Award, OPT 2007, 2007 年光電科技研討會學生論文獎)
4. C.W. He(何介暐) and Y.L. Lin(林俞良) and Y.T. Li(黎宇泰) and Ci Ling Pan(潘犀靈) and Hyeyoung Ahn(安惠榮) and **K.J. Chen(陳克堅)** and K.T. Chan(陳錦泰) , "CW THz Radiation Generated by Oxygen-ion-implanted GaAs Photoconductive Antenna", paper PE-67, presented at Annual Meeting of the Physical Society, Jan. 28-30, 2008, Hsinchu, Taiwan.
5. Kam Tai Chan, **Kejian Chen**, Yutai Li, WingYiu Cheung, Wei-wen Wang and Ci-Ling Pan, "GaAs:O Materials for Terahertz Generation", The 4th International Symposium on Ultrafast Phenomena & Terahertz Waves, Mar.29-31,2008
6. **Kejian Chen**, Yu-tai Li, Mong-huan Yang, Wing Yiu Cheung, Ci-Ling Pan, Kam Tai Chan, "A comparative study of bias-field-dependent output saturation of continuous wave THz radiation generated by oxygen-ion-implanted and epitaxial GaAs photoconductors", submitted to Optics Letters

References

[1] B. Ferguson and X. C. Zhang, "Materials for terahertz science and technology," *Nature Materials,* vol. 1, pp. 26-33, Sep 2002.

[2] E. Pickwell and V. P. Wallace, "Biomedical applications of terahertz technology," *Journal of Physics D-Applied Physics,* vol. 39, pp. R301-R310, Sep 7 2006.

[3] M. Brucherseifer, M. Nagel, P. H. Bolivar, H. Kurz, A. Bosserhoff, and R. Buttner, "Label-free probing of the binding state of DNA by time-domain terahertz sensing," *Applied Physics Letters,* vol. 77, pp. 4049-4051, Dec 11 2000.

[4] X. C. Zhang, "Terahertz wave imaging: horizons and hurdles," *Physics in Medicine and Biology,* vol. 47, pp. 3667-3677, Nov 7 2002.

[5] J. W. Shockley; W. T. Read, "Statistics of the Recombinations of Holes and Electrons," *Physical Review* pp. 835 - 842, 1952.

[6] A. W. M. Lee and Q. Hu, "Real-time, continuous-wave terahertz imaging by use of a microbolometer focal-plane array," *Optics Letters,* vol. 30, pp. 2563-2565, Oct 1 2005.

[7] D. Grischkowsky, S. Keiding, M. Vanexter, and C. Fattinger, "Far-Infrared Time-Domain Spectroscopy with Terahertz Beams of Dielectrics and Semiconductors," *Journal of the Optical Society of America B-Optical Physics,* vol. 7, pp. 2006-2015, Oct 1990.

[8] K. Kawase, Y. Ogawa, and Y. Watanabe, "Terahertz spectroscopic imaging and its application to drug detection," *Ieice Transactions on Electronics,* vol. E87c, pp. 1186-1191, Jul 2004.

[9] T. A. Liu, G. R. Lin, Y. C. Chang, and C. L. Pan, "Wireless audio and burst communication link with directly modulated THz photoconductive antenna," *Optics Express,* vol. 13, pp. 10416-10423, Dec 12 2005.

[10] G. A. Andreev, V. I. Leus, and V. N. Pozhidaev, "Space-earth radio links in the terahertz frequency band," *Journal of Communications Technology and Electronics,* vol. 49, pp. 867-873, Aug 2004.

[11] P. H. Siegel, "Terahertz technology," *Ieee Transactions on Microwave Theory and Techniques,* vol. 50, pp. 910-928, Mar 2002.

[12] D. H. Auston, "Picosecond Optoelectronic Switching and Gating in Silicon," *Applied Physics Letters,* vol. 26, pp. 101-103, 1975.

[13] M. Bass, P. A. Franken, and J. F. Ward, "Optical Rectification," *Physical Review,* vol. 138, pp. A534-&, 1965.

[14] D. Hashimshony, A. Zigler, and K. Papadopoulos, "Conversion of electrostatic to electromagnetic waves by superluminous ionization fronts," *Physical Review Letters,* vol. 86, pp. 2806-2809, Mar 26 2001.

[15] D. W. van der Weide, J. Murakowski, and F. Keilmann, "Gas-absorption spectroscopy with electronic terahertz techniques," *Ieee Transactions on Microwave Theory and Techniques,* vol. 48, pp. 740-743, Apr 2000.

[16] H. Zhong, N. Karpowicz, and X. C. Zhang, "Terahertz emission profile from laser-induced air plasma," *Applied Physics Letters,* vol. 88, pp. -, Jun 26 2006.

[17] N. Katzenellenbogen and D. Grischkowsky, "Efficient Generation of 380 Fs Pulses of Thz Radiation by Ultrafast Laser-Pulse Excitation of a Biased Metal-Semiconductor Interface," *Applied Physics Letters,* vol. 58, pp. 222-224, Jan 21 1991.

[18] A. Bartels, A. Thoma, C. Janke, T. Dekorsy, A. Dreyhaupt, S. Winnerl, and M. Helm, "High-resolution THz spectrometer with kHz scan rates," *Optics Express,* vol. 14, pp. 430-437, Jan 9 2006.

[19] B. Schulkin; and X.-C. Zhang, "mini-Z 1000 THz Time Domain Spectrometers."

[20] T. Kiwa, H. Murakami, and M. Tonouchi, "Generation of sub-terahertz waves using a semiconductor photomixer," *Superconductor Science & Technology,* vol. 16, pp. 1540-1543, Dec 2003.

[21] K. Kawase, J. Shikata, and H. Ito, "Terahertz wave parametric source," *Journal of Physics D-Applied Physics,* vol. 35, pp. R1-R14, Feb 7 2002.

[22] B. Gorshunov, A. Volkov, I. Spektor, A. Prokhorov, A. Mukhin, M. Dressel, S. Uchida, and A. Loidl, "Terahertz BWO-spectrosopy," *International Journal of Infrared and Millimeter Waves,* vol. 26, pp. 1217-1240, Sep 2005.

[23] V. Ryzhii, I. Khmyrova, and M. Shur, "Terahertz photomixing in quantum well structures using resonant excitation of plasma oscillations," *Journal of Applied Physics,* vol. 91, pp. 1875-1881, Feb 15 2002.

[24] R. Kohler, A. Tredicucci, F. Beltram, H. E. Beere, E. H. Linfield, A. G. Davies, D. A. Ritchie, R. C. Iotti, and F. Rossi, "Terahertz semiconductor-heterostructure laser," *Nature,* vol. 417, pp. 156-159, May 9 2002.

[25] Y. Cai, I. Brener, J. Lopata, J. Wynn, L. Pfeiffer, and J. Federici, "Design and performance of singular electric field terahertz photoconducting antennas," *Applied Physics Letters,* vol. 71, pp. 2076-2078, Oct 13 1997.

[26] J. E. Bjarnason, T. L. J. Chan, A. W. M. Lee, E. R. Brown, D. C. Driscoll, M. Hanson, A. C. Gossard, and R. E. Muller, "ErAs : GaAs photomixer with two-decade tunability and 12 mu W peak output power," *Applied Physics Letters,* vol. 85, pp. 3983-3985, Nov 1 2004.

[27] J. Mangeney, A. Merigault, N. Zerounian, P. Crozat, K. Blary, and J. F. Lampin, "Continuous wave terahertz generation up to 2 THz by photomixing on ion-irradiated In0.53Ga0.47As at 1.55 mu m wavelengths," *Applied Physics Letters,* vol. 91, pp. -, Dec 10 2007.

[28] P. Kordos, M. Marso, and M. Mikulics, "Performance optimization of GaAs-based photomixers as sources of THz radiation," *Applied Physics a-Materials Science & Processing,* vol. 87, pp. 563-567, Jun 2007.

[29] K. A. McIntosh, E. R. Brown, K. B. Nichols, O. B. McMahon, W. F. DiNatale, and T. M. Lyszczarz, "Terahertz photomixing with diode lasers in low-temperature-grown GaAs," *Applied Physics Letters,* vol. 67, pp. 3844-3846, Dec 25 1995.

[30] E. R. Brown, "A photoconductive model for superior GaAs THz photomixers," *Applied Physics Letters,* vol. 75, pp. 769-771, Aug 9 1999.

[31] E. R. Brown, F. W. Smith, and K. A. Mcintosh, "Coherent Millimeter-Wave Generation by Heterodyne Conversion in Low-Temperature-Grown Gaas Photoconductors," *Journal of Applied Physics,* vol. 73, pp. 1480-1484, Feb 1 1993.

[32] M. Y. Frankel, J. F. Whitaker, G. A. Mourou, F. W. Smith, and A. R. Calawa, "High-Voltage

Picosecond Photoconductor Switch Based on Low-Temperature-Grown Gaas," *Ieee Transactions on Electron Devices,* vol. 37, pp. 2493-2498, Dec 1990.

[33] T. A. Liu, M. Tani, and C. L. Pan, "THz radiation emission properties of multienergy arsenic-ion-implanted GaAs and semi-insulating GaAs based photoconductive antennas," *Journal of Applied Physics,* vol. 93, pp. 2996-3001, Mar 1 2003.

[34] G. R. Lin and C. L. Pan, "Ultrafast response of multi-energy proton-bombarded GaAs photoconductors," *Optical and Quantum Electronics,* vol. 32, pp. 553-571, May 2000.

[35] B. Salem, D. Morris, V. Aimez, J. Beauvais, and D. Houde, "Improved characteristics of a terahertz set-up built with an emitter and a detector made on proton-bombarded GaAs photoconductive materials," *Semiconductor Science and Technology,* vol. 21, pp. 283-286, Mar 2006.

[36] M. Mikulics, E. A. Michael, M. Marso, M. Lepsa, A. van der Hart, H. Luth, A. Dewald, S. Stancek, M. Mozolik, and P. Kordos, "Traveling-wave photomixers fabricated on high energy nitrogen-ion-implanted GaAs," *Applied Physics Letters,* vol. 89, pp. -, Aug 14 2006.

[37] B. Salem, D. Morris, Y. Salissou, V. Aimez, S. Charlebois, M. Chicoine, and F. Schiettekatte, "Terahertz emission properties of arsenic and oxygen ion-implanted GaAs based photoconductive pulsed sources," *Journal of Vacuum Science & Technology A,* vol. 24, pp. 774-777, May-Jun 2006.

[38] I. C. Mayorga, E. A. Michael, A. Schmitz, P. van der Wal, R. Gusten, K. Maier, and A. Dewald, "Terahertz photomixing in high energy oxygen- and nitrogen-ion-implanted GaAs," *Applied Physics Letters,* vol. 91, pp. -, Jul 16 2007.

[39] B. Salem, D. Morris, V. Aimez, J. Beerens, J. Beauvais, and D. Houde, "Pulsed photoconductive antenna terahertz sources made on ion-implanted GaAs substrates," *Journal of Physics-Condensed Matter,* vol. 17, pp. 7327-7333, Nov 23 2005.

[40] Chen Kejian, Li Yutai, Cheung Wingyiu, Wang Weiwen, Pan Ciling, and Chan Kamtai, "THz WAVES GENERATED BY OXYGEN IMPLANTED GaAs," in *2007 International Symposium on Antennas and Propagation* Niigata Convention Center, Niigata, Japan, 2007.

[41] K. Chen, Y. Li, W. Cheung, W. Wang, C. Pan, and K. Chan, "CW Sub-Terahertz wave generation by GaAs:O Materials," in *Lasers and Electro-Optics - Pacific Rim, 2007. CLEO/Pacific Rim 2007*, 2007.

[42] S. M. Sze, *Semiconductor devices, physics and technology*. New York: Wiley, 1985.

[43] J. F. Ziegler, "SRIM:The Stopping and Range of Ions in Matter."

[44] P. D. Townsend, J. C. Kelly, and N. E. W. Hartley, *Ion implantation, sputtering and their applications*. London ; New York: Academic Press, 1976.

[45] S. Mahajan and K. S. SreeHarsha, *Principles of growth and processing of semiconductors*. Boston: WCB/McGraw-Hill, 1999.

[46] G. S. May and S. M. Sze, *Fundamentals of semiconductor fabrication*: John Wiley &Sons,Inc, 2004.

[47] J. Lindhard, M. Scharff, and H. E. Shiøtt, "Range concepts and heavy ion ranges. ," *Mat. Fys. Medd. Dan. Vid. Selsk,* vol. 33(14), pp. 1-42, 1963.

[48] S. D. Benjamin, H. S. Loka, A. Othonos, and P. W. E. Smith, "Ultrafast dynamics of nonlinear absorption in low-temperature-grown GaAs," *Applied Physics Letters,* vol. 68, pp. 2544-2546, Apr 29 1996.

[49] S. D. Benjamin, A. Othonos, and P. W. E. Smith, "Large Ultrafast Optical Nonlinearities in as-Rich Gaas," *Electronics Letters,* vol. 30, pp. 1704-1706, Sep 29 1994.

[50] D. K. Schroder, *Semiconductor material and device characterization.* New York: Wiley, 1990.

[51] M. Tani, S. Matsuura, K. Sakai, and S. Nakashima, "Emission characteristics of photoconductive antennas based on low-temperature-grown GaAs and semi-insulating GaAs," *Applied Optics,* vol. 36, pp. 7853-7859, Oct 20 1997.

[52] B. R. Bennett, R. A. Soref, and J. A. Delalamo, "Carrier-Induced Change in Refractive-Index of Inp, Gaas, and Ingaasp," *Ieee Journal of Quantum Electronics,* vol. 26, pp. 113-122, Jan 1990.

[53] R. A. Soref and B. R. Bennett, "Electrooptical Effects in Silicon," *Ieee Journal of Quantum Electronics,* vol. 23, pp. 123-129, Jan 1987.

[54] F. Stern, "Dispersion of the Index of Refraction Near the Absorption Edge of Semiconductors," *Physics Review A,* vol. 133, 1964.

[55] L. P. Zverev, S. A. Negashev, V. V. Kruzhaev, and G. M. Minkov, "Mechanism of Band-Gap Variation in Heavily Doped Gallium-Arsenide," *Soviet Physics Semiconductors-Ussr,* vol. 11, pp. 603-605, 1977.

[56] C. H. Henry, R. A. Logan, and K. A. Bertness, "Spectral Dependence of the Change in Refractive-Index Due to Carrier Injection in Gaas-Lasers," *Journal of Applied Physics,* vol. 52, pp. 4457-4461, 1981.

[57] I. S. Gregory, C. M. Tey, A. G. Cullis, M. J. Evans, H. E. Beere, and I. Farrer, "Two-trap model for carrier lifetime and resistivity behavior in partially annealed GaAs grown at low temperature," *Physical Review B,* vol. 73, pp. -, May 2006.

[58] S. Gupta, J. F. Whitaker, and G. A. Mourou, "Ultrafast Carrier Dynamics in Iii-V-Semiconductors Grown by Molecular-Beam Epitaxy at Very Low Substrate Temperatures," *Ieee Journal of Quantum Electronics,* vol. 28, pp. 2464-2472, Oct 1992.

[59] P. R. Smith, D. H. Auston, and M. C. Nuss, "Subpicosecond Photoconducting Dipole Antennas," *Ieee Journal of Quantum Electronics,* vol. 24, pp. 255-260, Feb 1988.

[60] D. R. Dykaar, B. I. Greene, J. F. Federici, A. F. J. Levi, L. N. Pfeiffer, and R. F. Kopf, "Log-Periodic Antennas for Pulsed Terahertz Radiation," *Applied Physics Letters,* vol. 59, pp. 262-264, Jul 15 1991.

[61] M. Tonouchi, M. Tani, Z. Wang, K. Sakai, M. Hangyo, N. Wada, and Y. Murakami, "Enhanced THz radiation from YBCO thin film bow-tie antennas with hyper-hemispherical MgO lens," *Ieee Transactions on Applied Superconductivity,* vol. 7, pp. 2913-2916, Jun 1997.

[62] C. S. Wong, J. M. Dai, and H. K. Tsang, "Photoconductive detection of millimeter waves using proton implanted GaAs," *Applied Physics Letters,* vol. 75, pp. 745-747, Aug 9 1999.

[63] I. Strzalkowski, S. Joshi, and C. R. Crowell, "Dielectric-Constant and Its Temperature-Dependence for Gaas, Cdte, and Znse," *Applied Physics Letters,* vol. 28, pp. 350-352, 1976.

[64] L. F. Thompson, C. G. Willson, M. J. Bowden, American Chemical Society. Division of Organic Coatings and Plastics Chemistry., and American Chemical Society. Meeting, *Introduction to microlithography : theory, materials,and processing.* Washington, D.C.: The

Society, 1983.

[65] D. H. Auston, K. P. Cheung, J. A. Valdmanis, and D. A. Kleinman, "Cherenkov Radiation from Femtosecond Optical Pulses in Electro-Optic Media," *Physical Review Letters,* vol. 53, pp. 1555-1558, 1984.

[66] Z. S. Piao, M. Tani, and K. Sakai, "Carrier dynamics and terahertz radiation in photoconductive antennas," *Japanese Journal of Applied Physics Part 1-Regular Papers Short Notes & Review Papers,* vol. 39, pp. 96-100, Jan 2000.

[67] P. U. Jepsen, R. H. Jacobsen, and S. R. Keiding, "Generation and detection of terahertz pulses from biased semiconductor antennas," *Journal of the Optical Society of America B-Optical Physics,* vol. 13, pp. 2424-2436, Nov 1996.

[68] M. Tonouchi, N. Kawasaki, T. Yoshimura, H. Wald, and P. Seidel, "Pump and probe terahertz generation study of ultrafast carrier dynamics in low-temperature grown-GaAs," *Japanese Journal of Applied Physics Part 2-Letters,* vol. 41, pp. L706-L709, Jun 15 2002.

[69] A. Othonos, "Probing ultrafast carrier and phonon dynamics in semiconductors," *Journal of Applied Physics,* vol. 83, pp. 1789-1830, Feb 15 1998.

[70] S. D. Brorson, J. C. Zhang, and S. R. Keiding, "Ultrafast Carrier Trapping and Slow Recombination in Ion-Bombarded Silicon-on-Sapphire Measured Via Thz Spectroscopy," *Applied Physics Letters,* vol. 64, pp. 2385-2387, May 2 1994.

[71] J. T. Darrow, X. C. Zhang, and J. D. Morse, "Saturation Properties of Large-Aperture Photoconducting Antennas," *Ieee Journal of Quantum Electronics,* vol. 28, pp. 1607-1618, Jun 1992.

[72] J. T. Darrow, X. C. Zhang, and D. H. Auston, "Power Scaling of Large-Aperture Photoconducting Antennas," *Applied Physics Letters,* vol. 58, pp. 25-27, Jan 7 1991.

[73] P. K. Benicewicz, J. P. Roberts, and A. J. Taylor, "Scaling of Terahertz Radiation from Large-Aperture Biased Photoconductors," *Journal of the Optical Society of America B-Optical Physics,* vol. 11, pp. 2533-2546, Dec 1994.

[74] M. Tani, M. Herrmann, and K. Sakai, "Generation and detection of terahertz pulsed radiation with photoconductive antennas and its application to imaging," *Measurement Science & Technology,* vol. 13, pp. 1739-1745, Nov 2002.

[75] v. G. C. Loata, "Investigation of low-temperature-grown GaAs photoconductive antennae for continous-wave and pulsed terahertz generation," in *Vorgelegt beim Fachbereich Physik.* vol. Dissertation zur Erlangung des Doktorgrades der Naturwissenschaften Frankfurt: Johann Wolfgang Goethe-Universität, 2007.

[76] B. B. Hu, J. T. Darrow, X. C. Zhang, D. H. Auston, and P. R. Smith, "Optically Steerable Photoconducting Antennas," *Applied Physics Letters,* vol. 56, pp. 886-888, Mar 5 1990.

[77] D. Grischkowsky and N. Katzenellenbogen, "Femtosecond pulses of terahertz radiation: physics and applications," in *Picosecond Electronics and Optoelectronics, Tech. Dig. Ser. Washington, DC: Opt. Soc. Amer. pp. 9-14*, 1991.

[78] J. D. Jackson, *Classical electrodynamics*, 2nd ed. New York: Wiley, 1975.

[79] K. Lee, *Semiconductor device modeling for VLSI.* Englewood Cliffs, N.J.: Prentice Hall, 1993.

[80] J. Zhang, Y. Hong, S. L. Braunstein, and K. A. Shore, "Terahertz pulse generation and detection with LT-GaAs photoconductive antenna," *Iee Proceedings-Optoelectronics,* vol.

151, pp. 98-101, Apr 2004.

[81] X. Q. Jiang, J. Y. Yang, H. Z. Zhan, K. J. Chen, Y. Tang, X. H. Li, and M. H. Wang, "Photon-induced total-internal-reflection all-optical switches," *Ieee Photonics Technology Letters,* vol. 16, pp. 443-445, Feb 2004.

[82] D. H. Auston, K. P. Cheung, and P. R. Smith, "Picosecond Photoconducting Hertzian Dipoles," *Applied Physics Letters,* vol. 45, pp. 284-286, 1984.

[83] S. G. Park, M. R. Melloch, and A. M. Weiner, "Analysis of terahertz waveforms measured by photoconductive and electrooptic sampling," *Ieee Journal of Quantum Electronics,* vol. 35, pp. 810-819, May 1999.

[84] W.-W. Wang, "THz radiation emission properties of oxygen-ion-implanted GaAs photoconductive antennas," *Mphil. Thesis, National Chiao Tung University, Taiwan,* 2007.

[85] S. Verghese, K. A. McIntosh, and E. R. Brown, "Highly tunable fiber-coupled photomixers with coherent terahertz output power," *Ieee Transactions on Microwave Theory and Techniques,* vol. 45, pp. 1301-1309, Aug 1997.

[86] D. H. Martin and E. Puplett, "Polarised Interferometric Spectrometry for Millimetre and Submillimetre Spectrum," *Infrared Physics,* vol. 10, pp. 105-&, 1970.

[87] J. Shan and T. F. Heinz, "Terahertz radiation from semiconductors," *Ultrafast Dynamical Processes in Semiconductors,* vol. 92, pp. 1-56, 2004.

[88] K. J. Siebert, A. Lisauskas, T. Loffler, and H. G. Roskos, "Field screening in low-temperature-grown GaAs photoconductive antennas," *Japanese Journal of Applied Physics Part 1-Regular Papers Short Notes & Review Papers,* vol. 43, pp. 1038-1043, Mar 2004.

[89] B. I. Greene, J. F. Federici, D. R. Dykaar, A. F. J. Levi, and L. Pfeiffer, "Picosecond Pump and Probe Spectroscopy Utilizing Freely Propagating Terahertz Radiation," *Optics Letters,* vol. 16, pp. 48-49, Jan 1 1991.

[90] G. Rodriguez and A. J. Taylor, "Screening of the bias field in terahertz generation from photoconductors," *Optics Letters,* vol. 21, pp. 1046-1048, Jul 15 1996.

[91] M. Tani, K. Sakai, and H. Mimura, "Ultrafast photoconductive detectors based on semi-insulating GaAs and InP," *Japanese Journal of Applied Physics Part 2-Letters,* vol. 36, pp. L1175-L1178, Sep 15 1997.

[92] R. H. Jacobsen, K. Birkelund, T. Holst, P. U. Jepsen, and S. R. Keiding, "Interpretation of photocurrent correlation measurements used for ultrafast photoconductive switch characterization," *Journal of Applied Physics,* vol. 79, pp. 2649-2657, Mar 1 1996.

[93] A. S. Weling and T. F. Heinz, "Enhancement in the spectral irradiance of photoconducting terahertz emitters by chirped-pulse mixing," *Journal of the Optical Society of America B-Optical Physics,* vol. 16, pp. 1455-1467, Sep 1999.

[94] A. S. Weling, B. B. Hu, N. M. Froberg, and D. H. Auston, "Generation of Tunable Narrow-Band Thz Radiation from Large-Aperture Photoconducting Antennas," *Applied Physics Letters,* vol. 64, pp. 137-139, Jan 10 1994.

[95] Y. Q. Liu, S. G. Park, and A. M. Weiner, "Terahertz waveform synthesis via optical pulse shaping," *Ieee Journal of Selected Topics in Quantum Electronics,* vol. 2, pp. 709-719, Sep 1996.

[96] Y. Q. Liu, S. G. Park, and A. M. Weiner, "Enhancement of narrow-band terahertz radiation

from photoconducting antennas by optical pulse shaping," *Optics Letters,* vol. 21, pp. 1762-1764, Nov 1 1996.

[97] J. Kakalios and H. Fritzsche, "Persistent Photoconductivity in Doping-Modulated Amorphous-Semiconductors," *Physical Review Letters,* vol. 53, pp. 1602-1605, 1984.

[98] J. Betko, P. Kordos, S. Kuklovsky, A. Forster, D. Gregusova, and H. Luth, "Electrical-Properties of Molecular-Beam Epitaxial Gaas-Layers Grown at Low-Temperature," *Materials Science and Engineering B-Solid State Materials for Advanced Technology,* vol. 28, pp. 147-150, Dec 1994.

[99] S. E. Ralph and D. Grischkowsky, "Trap-Enhanced Electric-Fields in Semi-Insulators - the Role of Electrical and Optical Carrier Injection," *Applied Physics Letters,* vol. 59, pp. 1972-1974, Oct 14 1991.

[100] Z. D. Taylor, E. R. Brown, J. E. Bjarnason, M. P. Hanson, and A. C. Gossard, "Resonant-optical-cavity photoconductive switch with 0.5% conversion efficiency and 1.0 W peak power," *Optics Letters,* vol. 31, pp. 1729-1731, Jun 1 2006.

[101] N. L. Allen, M. Boutlendj, and H. A. Lightfoot, "Dielectric-Breakdown in Nonuniform Field Air Gaps - Ranges of Applicability to Dc Voltage Measurement," *Ieee Transactions on Electrical Insulation,* vol. 28, pp. 183-191, Apr 1993.

[102] J. H. Son, T. B. Norris, and J. F. Whitaker, "Terahertz Electromagnetic Pulses as Probes for Transient Velocity Overshoot in Gaas and Si," *Journal of the Optical Society of America B-Optical Physics,* vol. 11, pp. 2519-2527, Dec 1994.

[103] H. Thomas, J. K. Luo, D. V. Morgan, D. Westwood, K. Lipka, E. Splingart, and E. Kohn, "Improvement of the Breakdown Voltage of Gaas-Fets Using Low-Temperature-Grown Gaas Insulator," *Ispsd '94 - Proceedings of the 6th International Symposium on Power Semiconductor Devices & Ics,* pp. 155-160 436, 1994.

[104] P. C. Upadhya, W. H. Fan, A. Burnett, J. Cunningham, A. G. Davies, E. H. Linfield, J. Lloyd-Hughes, E. Castro-Camus, M. B. Johnston, and H. Beere, "Excitation-density-dependent generation of broadband terahertz radiation in an asymmetrically excited photoconductive antenna," *Optics Letters,* vol. 32, pp. 2297-2299, Aug 15 2007.

[105] A. G. Davies and E. H. Linfield, "Molecular and organic interactions," *Terahertz Frequency Detection and Identification of Materials and Objects,* pp. 91-106 364, 2007.

[106] Y. Cai, I. Brener, J. Lopata, J. Wynn, L. Pfeiffer, J. B. Stark, Q. Wu, X. C. Zhang, and J. F. Federici, "Coherent terahertz radiation detection: Direct comparison between free-space electro-optic sampling and antenna detection," *Applied Physics Letters,* vol. 73, pp. 444-446, Jul 27 1998.

[107] J. F. O'Hara, J. M. O. Zide, A. C. Gossard, A. J. Taylor, and R. D. Averitt, "Enhanced terahertz detection via ErAs : GaAs nanoisland superlattices," *Applied Physics Letters,* vol. 88, pp. -, Jun 19 2006.

[108] E. A. Michael, I. C. Mayorga, R. Gusten, A. Dewald, and R. Schieder, "Terahertz continuous-wave large-area traveling-wave photomixers on high-energy low-dose ion-implanted GaAs," *Applied Physics Letters,* vol. 90, pp. -, Apr 23 2007.

[109] G. C. Loata, T. Loffler, and H. G. Roskos, "Evidence for long-living charge carriers in electrically biased low-temperature-grown GaAs photoconductive switches," *Applied*

Physics Letters, vol. 90, pp. -, Jan 29 2007.

[110] P. T. Landsberg, *Recombination in semiconductors*. Cambridge: Cambridge University Press, 1991.

[111] R. M. Rubinger, A. G. de Oliveira, G. M. Ribeiro, J. C. Bezerra, M. V. B. Moreira, and H. Chacham, "Field-enhanced trapping in deep levels by multiple phonon emission in semi-insulating GaAs," *Journal of Applied Physics,* vol. 88, pp. 6541-6544, Dec 1 2000.

[112] R. H. Kingston, *Detection of optical and infrared radiation*: Springer Series in Optical Sciences, Berlin: Springer, 1978, 1978.

[113] A. S. Pine, R. D. Suenram, E. R. Brown, and K. A. McIntosh, "A terahertz photomixing spectrometer: Application to SO2 self broadening," *Journal of Molecular Spectroscopy,* vol. 175, pp. 37-47, Jan 1996.

[114] C. L. Wang, Y. H. Chuang, and C. L. Pan, "2-Wavelength Interferometer Bases on a 2-Color Laser-Diode Array and the 2nd-Order Correlation Technique," *Optics Letters,* vol. 20, pp. 1071-1073, May 1 1995.

[115] M. Naftaly, M. R. Stone, A. Malcoci, R. E. Miles, and I. C. Mayorga, "Generation of CW terahertz radiation using two-colour laser with Fabry-Perot etalon," *Electronics Letters,* vol. 41, pp. 128-129, Feb 3 2005.

[116] S.M.Sze, *Physics of Semiconductor Devices*: John Wiley&Sons,Inc., 1981.

[117] S. S.Li, *Semiconductor Physical Electronics*: Springer Science+Business Media,LLC, 2006.

[118] N. Zamdmer, Q. Hu, K. A. McIntosh, and S. Verghese, "Increase in response time of low-temperature-grown GaAs photoconductive switches at high voltage bias," *Applied Physics Letters,* vol. 75, pp. 2313-2315, Oct 11 1999.

[119] Y. Sasaki, H. Yokoyama, and H. Ito, "Dual-wavelength optical-pulse source based on diode lasers for high-repetition-rate, narrow-bandwidth terahertz-wave generation," *Optics Express,* vol. 12, pp. 3066-3071, Jul 12 2004.

[120] S. Matsuura, P. Chen, G. A. Blake, J. C. Pearson, and H. M. Pickett, "A tunable cavity-locked diode laser source for terahertz photomixing," *Ieee Transactions on Microwave Theory and Techniques,* vol. 48, pp. 380-387, Mar 2000.

[121] S. Matsuura, M. Tani, and K. Sakai, "Generation of coherent terahertz radiation by photomixing in dipole photoconductive antennas," *Applied Physics Letters,* vol. 70, pp. 559-561, Feb 3 1997.

[122] K. G. Gan, J. W. Shi, Y. H. Chen, C. K. Sun, Y. J. Chiu, and J. E. Bowers, "Ultrahigh power-bandwidth-product performance of low-temperature-grown-GaAs based metal-semiconductor-metal traveling-wave photodetectors," *Applied Physics Letters,* vol. 80, pp. 4054-4056, May 27 2002.

[123] E. A. Michael, "Travelling-wave photonic mixers for increased continuous-wave power beyond 1 THz," *Semiconductor Science and Technology,* vol. 20, pp. S164-S177, Jul 2005.

[124] J. B. D. Soole and H. Schumacher, "Transit-Time Limited Frequency-Response of Ingaas Msm Photodetectors," *Ieee Transactions on Electron Devices,* vol. 37, pp. 2285-2291, Nov 1990.

[125] E.R.Brown, "THz Generation by Photomixing in Ultrafast Photoconductors," *Internaltional Journal of High Speed Electronics and Systems,* vol. Vol.13, No.2 pp. 497-545, 2003.

[126] A. W. Jackson, "Low-temperature-grown GaAs photomixers designed for increased

terahertz output power," 1999.

[127] C. Jagadish, H. H. Tan, A. Krotkus, S. Marcinkevicius, K. Korona, J. Jasinski, and M. Kaminska, "Ultrafast carrier trapping and high resistivity of MeV energy ion implanted GaAs," in *Semiconducting and Semi-Insulating Materials Conference,1996.IEEE*, 1996, pp. 41-44.

[128] J. F. Holzman and A. Y. Elezzabi, "Two-photon photoconductive terahertz generation in ZnSe," *Applied Physics Letters,* vol. 83, pp. 2967-2969, Oct 6 2003.

[129] H. Ito, T. Furuta, F. Nakajima, K. Yoshino, and T. Ishibashi, "Photonic generation of continuous THz wave using uni-traveling-carrier photodiode," *Journal of Lightwave Technology,* vol. 23, pp. 4016-4021, Dec 2005.

[130] M. Suzuki and M. Tonouchi, "Fe-implanted InGaAs terahertz emitters for 1.56 mu m wavelength excitation," *Applied Physics Letters,* vol. 86, pp. -, Jan 31 2005.

[131] T. Kleine-Ostmann, K. Pierz, G. Hein, P. Dawson, and M. Koch, "Audio signal transmission over THz communication channel using semiconductor modulator," *Electronics Letters,* vol. 40, pp. 124-126, Jan 22 2004.

[132] K. L. Wang and D. M. Mittleman, "Metal wires for terahertz wave guiding," *Nature,* vol. 432, pp. 376-379, Nov 18 2004.

[133] J. Y. Lu, C. P. Yu, H. C. Chang, H. W. Chen, Y. T. Li, C. L. Pan, and C. K. Sun, "Terahertz air-core microstructure fiber," *Applied Physics Letters,* vol. 92, pp. -, Feb 11 2008.

[134] M. A. Belkin, J. A. Fan, S. Hormoz, F. Capasso, S. P. Khanna, M. Lachab, A. G. Davies, and E. H. Linfield, "Terahertz quantum cascade lasers with copper metal-metal waveguides operating up to 178 K," *Optics Express,* vol. 16, pp. 3242-3248, Mar 3 2008.

Appendix:

Appendix A:

Annealing operation (Steps and parameters):

1. Open water valve (2 in； 2 out).
2. Open N_2 valve. (To allow sample annealed at the inert gas blowing condition.)
3. Switch on electrical power (KG2-ZE)
4. Two valves for N_2, adjust the number to 100. (to control the flux of N_2 gas)
5. Switch on power. (to start microprocessor)
6. Setting parameters for process steps.

Some reading of knob related to the certain temperature:

300℃ (2.9);　350℃ (3.05);　400℃ (3.3)

450℃ (3.65);　500℃ (3.9);　550℃ (4.1)

7. Turn on "Stand by".
8. Try one or two cycles' chamber heating. (The temperature should higher than real needed to get rid of some unwanted contaminants on the surface of the chamber from previous annealing process. Let them escape from the chamber with the blowing N_2)
9. Put Samples onto the sample holder. (If the sample is GaAs or InGaAs, add a **GaAs cap** over the samples to decrease the escape of As ion)
10. Turn on "Start" to anneal samples.
11. After annealing is finished, let the temperature down to lower than 100□ before opening the chamber to bring out samples.
12. Close all the power and gas valves.

Appendix B:

The possible applications of screening effect

From such kind of screening effect discussed in Chapter 4.3.4, one can also think about some possible application based on it. For example, THz wave modulator or

THz switches. The modulation ratio of this kind of devices could be controlled by the power of CW background illumination. By optimizing the fs laser power and DC voltage, one could get enough THz output power and good modulation performance. Could this kind of THz modulator (or THz switch) be a suitable component for the future THz wave communication? For communication devices, the speed is a very important factor. As we know, the screening effect is mainly contributed by the photocarriers, and it will decay by the recombination of photocarriers. So the carrier recombination time is the speed limitation factor for such devices. The band-to-band recombination or Auger recombination is expected to be roughly of the order of sub-nanosecond [68, 69]. So if this kind of THz modulator can be fabricated, it could fulfill the requirement of (at least) 1GHz THz communication network, comparing with the fastest speed currently obtained by electrical modulation method [9, 131].

Another possible application as mentioned before is for the physical study, like carrier recombination time. By modifying that theoretical model and make sure the relationship of carrier recombination time of material and other parameters which can be measured in such kind of experiment. From them, one could find the possible original value of carrier recombination time by fitting the curve and the possible value under different working condition (bias voltage and CW background illumination power). Then this kind of method could also be an approach for recombination time investigation.

Appendix C:

Experiment for THz generation by 1550nm fiber laser pumping.

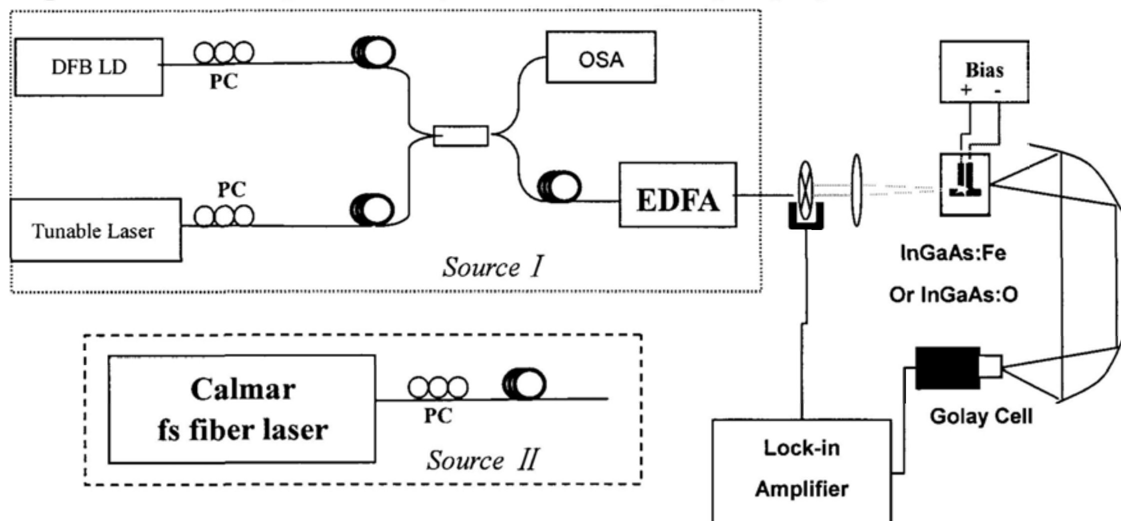

Figure a.1: THz wave generation from the fiber based system. (1550 nm for InGaAs)

Device	Material	Structure	R_{drak} (kΩ)	R_{light} (KΩ)	V_{max} (V)	P_{max} (μV)	P_{err} (μV)
No.134_ R1(+)&R2(-)	InGaAs: 250℃	Dipole	842.3	235.2	70	**35.055**	3.695
No.134_ R1(-)&R2(+)	InGaAs: 250℃	Dipole	886.5	474.4	70	**8.33**	1.61
No.138_ L4&R4	InGaAs: 250℃	spiral	4598	1115	100	31.47	1.09
No.138_ L6(+)&R6(-)	InGaAs: 250℃	spiral	328.6	159.11	120	22.885	0.755
No.137_ L3(+)&R3(-)	InGaAs: 200℃	spiral	672	96.45	100	17.36	2.06
No.137_ L3(-)&R3(+)	InGaAs: 200℃	spiral	672	96.45	100	**93.2**	1.3

Table a.1: Pulsed THz wave generated by LT InGaAs based PC devices under 1550nm fs fiber laser pumping.

Appendix D:

Thinking of THz applications

At end of this thesis, let's think about some possible applications of THz wave, not only limited in the directions related to this work.

At first, let's dream about the space century, when human migrate to the planet outside earth, will come soon. Maybe this century will be, although 8 years already passed. Or it will be the next one.

It listens like a dream, but please remember, "If you think it is only a dream, it is a dream undoubtedly. But if you think it is not only a dream but also a coming future, then it will be the truth as you wished."

Currently ones talking about THz communication, but always think the things

in earth environment. Then some one will question like "THz communication? How can the THz wave transmit in air for long distance? 10-100 m should be the longest distance in free space, (not metal wire[132] or air-cored fiber[133]), then this kind of distance is communication will be useful?" From the point view of on earth, they are right, it is difficult for THz wave transmitting long distance (with huge absorption of vapor in air). If we put the THz technology in the view of space century, what will happen?

In space, one can use THz wave to transmit signal without considering the loss, which may cause by the vapor, because in that environment it is working in vacuum. Then what's the advantage of THz wave comparing with the microwave currently used in space signal exchange? As in space (vacuum environment), all E.M waves have the same transmit speed, the only difference between the THz wave and microwave (or light wave) is their dispersion and signal carry ability. For THz wave, its frequency is higher than microwave, which endows it a larger signal carry ability comparing with microwave. So using THz wave as the carrier wave, one can obtain a high capacity signal transmission network. And THz wave has a smaller dispersion angle comparing with THz wave, and larger one than light wave (see Figure 6.2). This allow one to transmit signal point to point with less possibility of being spied, comparing with microwave, not only the spy in space but also the spy on earth. To microwave, as it has large dispersion angel, one has lots of spaces for him to put a spy satellite. One can also spy just on earth if he has enough technology to magnify the small signal from space into the earth. But for THz wave, there almost no chance to spy on earth, because the most of THz signal have been absorbed by atmosphere already, before reaching to spy base-station. In space, the space for setting spy satellite is also much limited. Maybe someone will question, then light wave has smallest dispersion angle and largest signal transmission capacity, then what is advantage of THz wave? As the speed of satellite moving in space is very fast, if one use light to built this network, it will be more difficult to keep the network be connect without missing the target. For easy handling,

microwave is the best choice, and for less spy possibility light wave will be the best. But if consider them together, THz wave will be the best one.

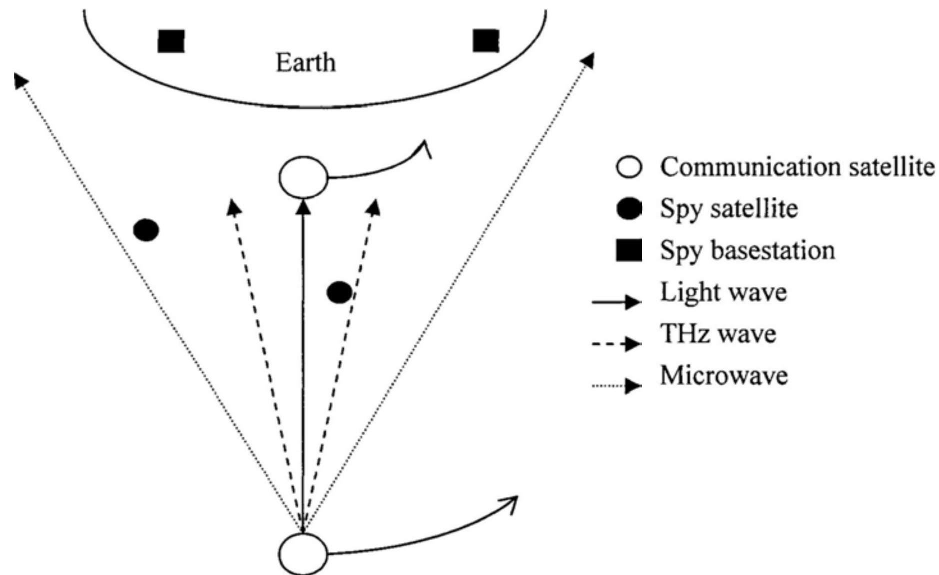

Figure a.2 Signal transmission in space.

When human migrate in planet outside earth, the THz communication network can also be built on that planet for its high capacity signal transmission. And for space usage, the THz wave generation source should be as compact as possible. Fiber laser pumped PC devices should be one of choice. The other like Gunn diode laser, BWO, and QCL are all can be selected. To the opinion of author, the QCL will be the king of the future THz wave generation source, if it can solve the limitation of operation temperature (currently it highest value is 178K [134]). Its advantages like high output power, compact size, and tunable wavelength are all very suitable for the application in space.

Ok, now let's come back to earth. As those application introduced in Chapter 1, here we will discuss some other possible application directions or devices (systems).

1. Detection of antique in the wood wall, which is parts of an archaic building.

2. Character recognizing of archaic book or manuscript, which having new Character over the archaic one. Between these two version characters, there is a calcareousness layer to hide (cover) archaic one.

3. Explosive package detection with a movable robot, which has a compact THz imaging system in his body.

4. Composition analysis for some unknown material, with a THz spectrum analyzer robot. (Especially for the material analyzing in new planet investigation area).

5. Reflection THz spectrum analyzing for liquid material (water, blood, and so on) or some high THz wave absorption materials.

6. An integrate CW and pulsed THz wave generation system for lab or commercial usage.

7. Outer space secret communication (Fiber based pumping sources, PC devices, OCDMA technique)

……..